Testing Models of Sheaths and Instabilities with Particle-in-cell Simulations

by

Lucas P. Beving

A dissertation submitted in partial fulfillment
of the requirements for the degree of
Doctor of Philosophy
(Applied Physics)
in The University of Michigan
2023

Doctoral Committee:

Associate Professor Scott Baalrud, Chair
Professor John Foster
Dr. Matthew Hopkins, Sandia National Laboratory
Professor Mark Kushner
Professor Ryan McBride

Lucas P. Beving

lbeving@umich.edu

ORCID iD: 0000-0001-6498-2822

ACKNOWLEDGEMENTS

I am thankful for always feeling supported (financially, emotionally, and academically) as I traversed my graduate career. I find it difficult to imagine that I would have succeeded with out the support of my mentors, friends, and family.

Foremost, I would like to thank Scott Baalrud, my thesis advisor, who has helped me develop a long list of skill, not limited to reasoning, writing, and public speaking. I appreciate your patience and understanding over the last six years. Your knack for finding interesting problems is something I will strive for in my career.

Matthew Hopkins, my mentor and collaborator, deserves just as much thanks. Our meetings would often take more than the scheduled time, but always made me feel excited by my research and tangent interests. Your help with Aleph was a necessary (but not sufficient!) condition for my success.

My colleagues, who I first met at the University of Iowa, also deserve immense thanks for keeping me afloat when classes, research, and life threw me an unexpected twist: thanks Louis, Brett, Nathaniel, David, Keith, Ryan, Shane, Sanat, and Kwang! I would also like to acknowledge the graduate students, staff, and professors at Iowa who made my time there enriching and enjoyable.

The Applied Physics Program here at Michigan deserves my thanks for being welcoming and helpful with my transfer. The opportunities Michigan offered me, in terms of classes and connections, cannot be understated. I would also like to thank Marco, Jake, Lucas, Moises, Julian, and Julia for the camaraderie during my stay in Cooley. I also appreciate the members of my committee taking the time to help me

develop a better thesis through questions and comments.

Last, but not least, I would like to thank my family for suffering through countless "it's going fine" and "I'll be done *sometime soon*." Mom and dad, thanks for keeping me up-to-date with whats happening at home! I can not imagine getting here without you all, especially Ann and Carol, who did not get the chance to see me graduate.

TABLE OF CONTENTS

LIST OF FIGURES

Figure

LIST OF TABLES

LIST OF APPENDICES

Appendix

ABSTRACT

Sheaths and presheaths represent the response of a plasma to boundaries and are an instance of plasma self-organization. They are commonly utilized in plasma technologies and reduced models of plasmas across a range of gas pressures. This thesis leverages the particle-in-cell method to explain discrepancies between models and measurements of ion temperature at low pressures, test untested models of high pressure sheaths, and explore a novel electron plasma wave instability driven by an ambipolar electric field.

Simulations reveal that ion-acoustic instabilities excited in presheaths can cause significant ion heating. Ion-acoustic instabilities are excited by the ion flow toward a sheath when the neutral pressure is small enough and the electron temperature is large enough. A series of 1D simulations were conducted in which electrons and ions were uniformly sourced with an ion temperature of 0.026 eV and different electron temperatures (0.1 - 50 eV). Ion heating was observed when the electron-to-ion temperature ratio exceeded the minimum value predicted by linear response theory to excite ion-acoustic instabilities at the sheath edge ($T_e/T_i \approx 28$). When this threshold was exceeded, the temperature equilibriation rate between ions and electrons increased near the sheath so that the local temperature ratio did not exceed the threshold for instability. This resulted in significant ion heating near the sheath edge, which also extended back into the bulk plasma because of wave reflection from the sheath. The instability heating was found to decrease for higher pressures, where ion-neutral col-

lisions damp the waves and ion heating is instead dominated by inelastic collisions in the presheath.

Simulations using the direct simulation Monte Carlo method were used to study how neutral pressure influences plasma properties at the sheath edge. The high rate of ion-neutral collisions at pressures above several mTorr were found to cause a decrease in the ion velocity at the sheath edge (collisional Bohm criterion), a decrease in the edge-to-center density ratio, and an increase in the sheath width and sheath potential drop. A comparison with existing analytic models generally indicates favorable agreement, but with some distinctions. One is that models for the edge-to-center density ratio need to be made consistent with the collisional Bohm criterion. With this and similar corrections, a comprehensive fluid-based model of the plasma boundary was constructed that compares well with the simulations.

Ambipolar electric fields are commonplace in plasmas and affect transport by driving currents and in some cases instabilities. Simulations demonstrate that an instability, named the electron-field instability, can be driven by an ambipolar strength electric field. The instability excites waves of 30 Debye-lengths and has a growth-rate that is proportional to the electric field strength. Unlike other instabilities, the electron-field instability only requires that the electrons interact with the field and does not result from the relative drift between electron populations (beam instability) or electrons and ions (ion-acoustic instability). In fact, the instability occurs near the electron plasma frequency which is much higher than most drift instabilities. Low-temperature and space-based plasmas are found to be likely systems where the instability may be excited. We find that our simulations and linear theory agree until a non-linear state is reached in the simulations.

These results demonstrate that low pressure sheaths are susceptible to instabilities that can significantly affect plasmas properties, while fluid model accurately capture collisional effects at higher pressures.

CHAPTER I

Introduction

1.1 Background

Plasmas, like neutral gases, naturally expand to fill the space that surrounds them. For this reason terrestrial plasmas are often confined by material boundaries so that they can be readily studied or utilized in applications. However, unlike neutral gasses, the electron and ions that make up the plasma self-organize near the material boundaries to form two regions: the positively charged sheath and the quasineutral presheath. The positive space charge of the sheath confines the often hotter and faster electrons, while the presheath accelerates the much slower and colder ions toward the sheath, supplying it with positive charges.

Some of the earliest experiments and observations of the plasma boundary were performed in low temperature plasmas, where the electrons were generally much hotter than the room temperature ions [1, 2, 3]. Low-temperature plasmas are formed by ionizing neutral gas near room temperature ($\approx$ 300 K or 0.026 eV), leading to relatively low temperature ions compared to other plasmas, like a fusion plasma. Unlike the ions, the electrons may have a temperature of several eV after ionization has taken place, making low-temperature plasmas characteristically non-equilibrium systems. In applications, like etching or ion-bombardment, this is advantageous as electrons can activate chemical reactions, while the ions can be used to bombard

surfaces with a somewhat controllable energy distribution [4].

Much experimental and theoretical work was done over the past century to uncover the structure and function of the sheath and presheath regions. Some of the earliest work focused on understanding the plasma boundary in low pressure vacuum systems which provided a repeatable and steady-state system. Irving Langmuir was one of the first and most notable scientist to study the plasma boundary [1], and was in fact the one who named the sheath. He also discovered high frequency waves in the plasma, that are called electron plasma waves or Langmuir waves. Furthermore, he and others developed the early mathematical infrastructure for describing the sheath and presheath. Namely, the Tonks-Langmuir model [5, 6, 7] of the presheath that included ion kinetic effects predicted two important phenomena: ions accelerate toward the sheath and the ion temperature increases near the sheath. The Tonks-Langmuir model is still a touchstone for modern analytic plasma models for its practicality, while including kinetic effects.

However, the Tonks-Langmuir model, and all subsequent models, do not account for the presence of instabilities. Kinetic instabilities result from interactions between particles and fluctuations in the electric (and/or magnetic) field, where particle kinetic energy is converted into fluctuation (wave) energy [8]. Such instabilities can be understood through the lens of plasma kinetic theory, and were developed later than the ideas of sheath and presheath [9]. More recently, instabilities have been understood to affect the dynamics of the plasma where they occur as described by quasi-linear and non-linear effects [10]. This includes instability enhanced collisions [11], where the growing waves of the instability effectively increase the Coulomb collision rate between particles. Such collisions are expected to result in larger than normal friction between species or larger energy relaxation rates. Enhanced friction has been observed to affect ion properties in multi species plasma boundaries [12, 13, 14]. Specifically, when two ion species are present the ion-ion two stream

instabilities enhance the friction between the two species. Ultimately this was found to determine the relevant form of Bohm's criterion for multi component plasmas. For single species plasmas the effects of instabilities are still largely unknown and untested. This leads to the questions: what instabilities are present in the plasma boundary and what are the associated effects? These are two of the questions treated by this thesis.

As plasmas became more and more prevalent in engineering applications more motivation was placed on understanding the plasma boundary at higher pressures, where collisions are moderately or very important. For example, the etching of semiconductors, implantation and coating of machine parts, or treatment of wounds. Such applications span a broad range of neutral gas pressures (1 mTorr to 760 Torr) and motivate an understanding of the dynamics of the plasma boundary at different pressures.

Furthermore the standard picture of the sheath and presheath developed by Langmuir and others was extended to include collisional effects at intermediate and higher pressures. Notably, these have included predictions for a collisional Bohm criterion, where ions accelerate less through the presheath due to collisions [15, 16, 17, 18]. This represents a fairly significant deviation from the models of collisionless presheath. However, this and other related predictions have yet to be tested experimentally. Experimental tests of theories of collisional plasmas are naturally difficult as the staple plasma diagnostics were generally designed to work at relatively low pressures. Thus, testing models of the collisional sheath (and presheath) is another aim of this thesis.

Instead of using experimental techniques, this thesis will leverage particle-in-cell (PIC) simulation techniques to study the effects of instabilities (at low pressure) and collisions (at higher pressures) on the plasma boundary region. Specifically, this thesis will use the PIC code Aleph developed at Sandia National Laboratory. PIC simulations can complement experiments since they can simulate plasmas at different

pressures, while including linear and non-linear affects that would be present in an experiment (effectively all the effects captured by the Vlasov equation). However, simulations often suffer from being computationally expensive when including all of the relevant physics. Chapter I introduces the Tonks-Langmuir model, Bohm criterion, collisional models, instability-enhanced collisions, and the PIC method in more detail. Chapter II details how ion-acoustic instabilities cause excess ion heating beyond the Tonks-Langmuir model near the sheath. Chapter III describes a collisional model of the sheath and tests it with simulations, showing that there is a collisional Bohm criterion. Finally, chapter IV illustrates how ambipolar electric fields can drive instabilities near the electron plasma frequency at conditions relevant to the presheath.

1.2 Model of the weakly collisional plasma boundary

In the following sections the standard picture of the plasma boundary is illustrated through Bohm's criterion (sheath) and the Tonks-Langmuir model (presheath). Together these two models describe the basic features of the weakly collisional plasma boundary: ion acceleration via a potential drop, ion heating, and a reduction in the density across the presheath. Here weakly collisional means that the mean free path of collisions is much larger than the length of the plasma boundary, making ionization the dominant collisional effect.

An important location for both Bohm's criterion and the Tonks-Langmuir model is the sheath edge. Practically, the sheath edge is thought of as the point between the quasineutral presheath and the positively charged sheath, even though there is technically a thin intermediate region that separates the two [19]. The importance of the sheath edge has lead to many discussions of what is the best sheath edge definition. The two most common definitions are "where quasineutrality breaks down" and"where the ions reach the sound speed."

The first is the more practical, but also relies on the user choosing what constitutes a *significant* breakdown in quasineutrality. Often the deviation from quasineutrality is measured by the charge density $(q_i n_i - e n_e)$. Then the sheath edge is where the charge density exceeds a chosen fraction of the electron charge density, maybe $(n_i - n_e)/n_e > P_\rho \sim 1 - 10\%$ for singly charged ions. In many cases this is sufficient, specifically if the quantities of interest are not observed to change significantly as P_ρ is varied.

The second is less practical since it requires measuring ion velocities. It is based on the work of David Bohm who showed that the ions must reach the sound speed by the sheath edge for a stable sheath to form [20]. This is called Bohm's criterion and is often expressed as $V_i \geq c_s = \sqrt{T_e/m_i}$, where T_e is the electron temperature in units of energy, m_i is the ion mass, and c_s is the sound speed. The sheath edge is often defined as the location where Bohm's criterion is first satisfied, i.e. where $V_i = c_s$.

Ultimately, either definition of the sheath edge will provide essentially the same location at low pressures. However, at higher pressures the ions experience friction with neutrals and it becomes unclear whether Bohm's criterion is the appropriate location of the sheath edge. For this reason we adopt the first definition of the sheath edge throughout this thesis. Collisional models of Bohm's criterion exist [15, 16, 17, 18] and are the subject of chapter III. The following is a standard derivation of Bohm's criterion for a collisionless plasma sheath and provides a starting point for understanding the sheath at higher pressures and when instabilities are present.

1.2.1 Bohm's criterion and collisionless sheaths

Ultimately, derivations of Bohm's criterion solve Poisson's equation near the sheath edge, which requires information on the electron and ion densities. The electron and ion densities can be related to the potential ϕ by using several approximations. Flux

conservation through the sheath relates the ion density to the ion velocity:

$$V_{se} n_{se} = V(x) n(x). \tag{1.1}$$

Flux conservation is appropriate in the sheath, since the sheath is very thin and so very few ionization events can occur. The ion velocity can be related to the potential when energy is conserved. For cold ($T_i = 0$) and collisionless ions entering the sheath with a velocity of V_{se} conservation of ion energy can be written as

$$\frac{1}{2} m_i V_{se}^2 + e\phi_{se} = \frac{1}{2} m_i V(x)^2 + e\phi(x), \tag{1.2}$$

where ϕ_{se} is the potential at the sheath edge.

Together Eq. (1.2) and (1.1) provide an expression for the ion density in the sheath in terms of the potential:

$$n(x) = n_0 \left(1 + \frac{2e(\phi_{se} - \phi(x))}{V_{se}^2 m_i} \right)^{-1/2}. \tag{1.3}$$

An expression for the electron density in term of potential is provided by the Boltzmann density relation $n_e = n_{se} \exp[e\phi(x)/T_e]$. This relation is appropriate when electrons have a small average velocity and are effectively isothermal. Then Poisson's equation can be written, in dimensionless variables $\eta = e\phi/T_e$ and $X = x/\lambda_{De}$, as

$$\frac{\mathrm{d}^2 \eta}{\mathrm{d}x^2} = \left(e^{\eta - \eta_{se}} - \left(1 + \frac{2T_e(\eta_{se} - \eta)}{m_i V_{se}^2} \right)^{-1/2} \right). \tag{1.4}$$

Multiplying Eq. (1.4) by $\mathrm{d}\eta/\mathrm{d}X$ and integrating leaves the expression

$$\frac{1}{2} \left(\frac{\mathrm{d}\eta}{\mathrm{d}X} \right)^2 = e^{\eta} - 1 + \frac{m_i V_{se}^2}{T_e} \left(-1 + \sqrt{1 - \frac{2T_e \eta}{m_i V_{se}^2}} \right), \tag{1.5}$$

where $\eta_{se} = 0$ is used to eliminate the constant of integration. In addition $(\mathrm{d}\eta/\mathrm{d}X)_{se} =$

0 was used as a boundary condition and is a good approximation since the electric field at the presheath-sheath boundary is expected to be very small compared to that inside the sheath. Clearly, the left hand side is always positive and will lead to the criterion on V_{se},

$$0 \leq e^{\eta} - 1 + \frac{m_i V_{se}^2}{T_e}\left(-1 + \sqrt{1 - \frac{2T_e\eta}{m_i V_{se}^2}}\right). \tag{1.6}$$

A criterion on the sheath edge parameters can be found by expanding Eq. (1.6) about $\eta_{se} = 0$ to second order:

$$0 \leq 1 + \eta + \frac{\eta^2}{2} - 1 + \frac{V_{se}^2}{c_s^2}\left(-1 + 1 - \eta\frac{c_s^2}{V_{se}^2} - \eta^2\frac{c_s^4}{2V_{se}^4}\right). \tag{1.7}$$

Canceling terms gives the collisionless Bohm criterion:

$$V_{se} \geq c_s. \tag{1.8}$$

This criterion on the ion velocity into the sheath is quite powerful as it indicates that the primary means for tuning the ion energy directed out of the plasma is the electron temperature. It can be used as a boundary condition in fluid simulation or in global models for entire devices. It is no surprise that extensions of Eq. (1.8) to collisional systems are of significant interest, since plasmas are made across a wide range of pressures.

1.2.2 Tonks-Langmuir model of the presheath

The Tonks-Langmuir model [5] is a steady-state model of the presheath that includes ion kinetic effects. It captures the effects of cold ions being born at different positions in a monotonic potential and so forming a complex velocity distribution. The model is quite simple, but incorporates important kinetic effects while still remaining tractable. However, the model is only applicable at low pressures since the

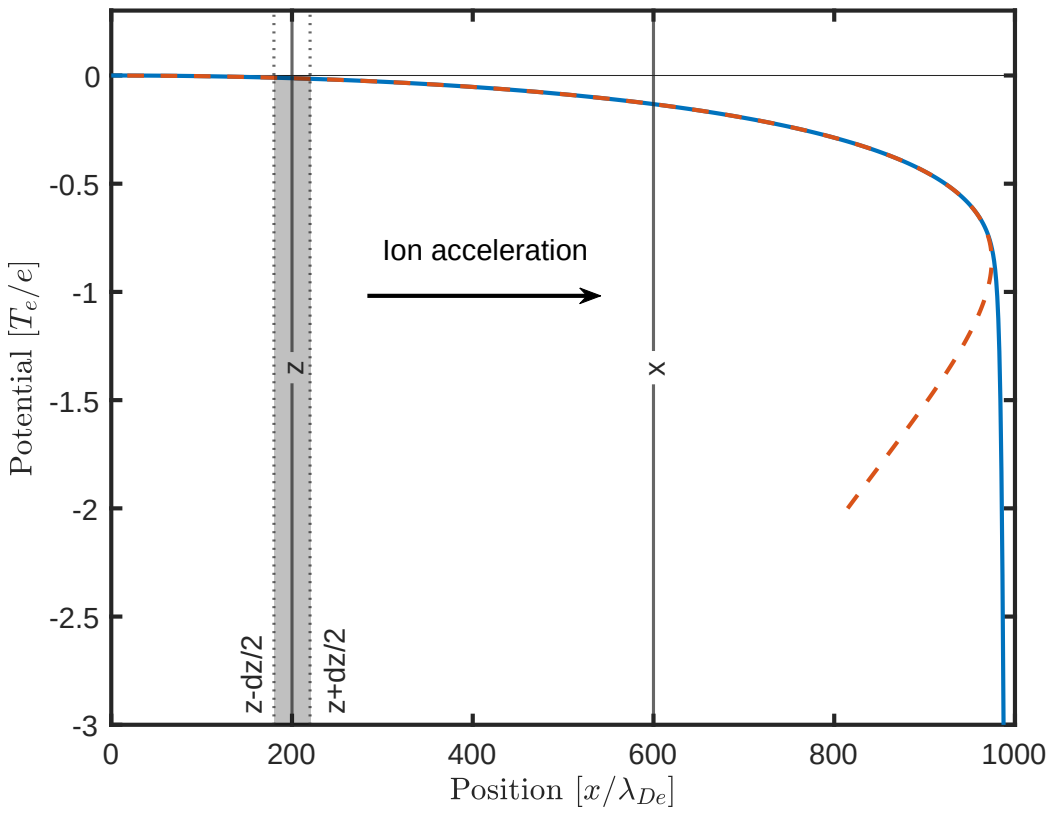

Figure 1.1: Analytic (red dashed) and numerical (blue solid) potential profiles from the Tonks-Langmuir model. The presheath was taken to be 1000 λ_{De} for the solutions. Positive ions at position z contribute to the density at x as ions accelerate to the right.

ions are assumed collisionless (besides ionization). In addition, the model assumes the ions are born at rest and so restricts its applicability to situations where ions are sourced at temperature far below that of electrons. Here we review the derivation and features, which was first solved by series expansion in [5]. We will present the analytic solutions that were later found by Harrison and Thompson [6].

Figure 1.1 shows the potential calculated from the model (red dashed) alongside a full numerical solution for the potential in the presheath and sheath (blue solid). The numerical solution effectively solves Poisson's equation through relaxation as described in [21] and can capture the sheath potential as well. This illustrates that the Tonks-Langmuir model can only capture the presheath before breaking down (i.e

it becomes multivalued at a point). However, the model still captures important physics without relying on numerical techniques, making it an attractive starting point for understanding the plasma boundary.

Furthermore, Fig. 1.1 illustrates the monotonic potential profile characteristic of the presheath and can be used to construct the model. Here the ions are born at rest, so the only ions that can reach the position x must be born at or to the left of x. Then the contribution to the density at x from a region of width $\mathrm{d}z$ of plasma centered at z can be written as:

$$\mathrm{d}n_i = f_i(v_i)\mathrm{d}v_i = \frac{g_{iz}(z)}{v_i(x,z)}\mathrm{d}z, \tag{1.9}$$

where $\mathrm{d}n_i$ is the ion density in $\mathrm{d}z$, f_i is the ion VDF, g_{iz} is the ionization rate per volume, and $v_i(x,z)$ is the speed an ion born at z has when it arrives at x.

To proceed, we assume that the energy of each ion is conserved as it transits the presheath potential drop. This means that no collisions should occur for the model to be applicable and limits it to systems where the mean free path of ions is larger than the presheath (i.e. low pressure). Then $v_i(x,z) = \sqrt{(2e/m_i)(\phi(x)-\phi(z))}$ where ϕ is the potential. Integrating Eq. (1.9) from the beginning of the presheath ($x = 0$) to x gives the ion density profile:

$$n_i(x) = \sqrt{\frac{m_i}{2e}}\int_0^x \frac{g_{iz}}{\sqrt{\phi(x)-\phi(z)}}\mathrm{d}z. \tag{1.10}$$

This equation can be converted into an integral equation for ϕ by specifying n_i and g_{iz} in terms of ϕ. To do this we both enforce quasineutrality ($n_i \approx n_e$) throughout the presheath and that the electrons are isothermal. Isothermal electrons follow the Boltzmann density relation $n_e(x) = n_0 \exp[e\phi(x)/T_e]$, where n_0 is density at $x = 0$ and represent the bulk plasma density. Replacing the ion densities with the Boltzmann density gives a single equation for the potential

$$\exp[e\phi(x)/T_e] = \sqrt{\frac{m_i}{2e}} \int_0^x \frac{g_{iz}}{\sqrt{\phi(x) - \phi(z)}} \mathrm{d}z, \tag{1.11}$$

which can be solved assuming we know the spatial form of g_{iz}. Throughout this work we will focus on ionization profiles that are uniform, meaning g_{iz} does not depend on the spatial coordinate. This is an appropriate assumption when modeling many low temperature devices where a small population of high energy electrons is responsible for ionizing the neutral gas. Such electrons often have large mean free paths compared to the plasma and so make several passes through the volume before ionizing a neutral atom, resulting in a uniform ionization profile.

However, the Tonks-Langmuir model can accommodate more complicated ionization profiles. This is shown in [6] where the form $g_{iz} \propto g_0 \exp(\gamma\phi)$ is used, where γ and g_0 are constants. For example $\gamma = 0$ represents a uniform ionization profile, while $\gamma = 1$ represents one proportional to the electron density. Larger values can be used and represent multi-step ionization processes.

When a uniform ionization profile is assumed Eq. (1.11) can be transformed using $-e\phi(x)/T_e = y^2$ and $-e\phi(z)/T_e = y^2 \sin\theta$ to a form which can be solved by a Schlömich transformation to give:

$$\pi g_{iz} \frac{\mathrm{d}x}{\mathrm{d}\eta} \sqrt{\eta \frac{m_i}{2T_e}} = n_0 \big[1 - 2\sqrt{\eta} e^{-\eta} D(\sqrt{\eta})\big], \tag{1.12}$$

where $\eta = e\phi/T_e$, and $D(x) = \int_0^x \exp(t^2)\mathrm{d}t$ is the Dawson function. Note that the modern definition of the Dawson function (or integral) can vary. Equation (1.12) can be integrated to give an implicit equation for the potential profiles:

$$\begin{aligned} x &= \frac{\sqrt{2T_e/m_i}}{g_{iz}/n_0} e^{-\eta} D(\sqrt{\eta}), \\ \frac{x}{\lambda_{De}} &= \frac{4\sqrt{2}}{\pi} \frac{L}{\lambda_{De}} e^{-\eta} D(\sqrt{\eta}), \end{aligned} \tag{1.13}$$

which is plotted in Fig. 1.1 as the red dashed line. To get the final equation we used the fact that the flux of particles out of and into the domain should be the same (i.e $g_0 = n_0 c_s/(2L)$). Notably this solution has a clear point where it fails as it becomes multivalued on the right. This corresponds to the position where the factor of $\mathrm{d}x/\mathrm{d}\eta = 0$ in equation 1.12, at $x/L \approx 0.973$ or at $x/\lambda_{De} \approx 973$ in Fig. 1.1. Clearly, this point represents a significant breakdown in the quasineutrality. The potential takes a value of $e\phi = 0.854T_e$ at this point, while the electron and ion densities are $n = 0.426n_0$. Other ion properties can now be calculated using the implicit equation for the potential (Eq. (1.13)).

Namely, the ion properties are all related to the ion velocity distribution function (IVDF), which can be rewritten from Eq. (1.9) in terms of the potential as [22]:

$$f_i[v_i/c_s, \eta(x)]\mathrm{d}v_i/c_s = \frac{\sqrt{2}}{\pi}\left[\sqrt{-\eta} - 2e^{\eta}D(\sqrt{-\eta})\right], \quad v_i/c_s \in (0, -\eta(x)). \tag{1.14}$$

The IVDF is shown in Fig. 1.2 at different positions in the presheath. The model predicts there is a maximum velocity for the ions at each position and the IVDFs are cutoff past this velocity. Also, the model predicts no particles with negative velocities since the ions are born at rest and can only move with positive velocities toward the sheath edge following the potential profile. An important feature of the IVDFs is the low velocity tail that is present, skewing the IVDFs to lower velocities. Ultimately, this leads to an increase in the ion temperature (width of the IVDF) near the sheath edge. Here the IVDFs have been normalized by the maximum value at each position for clarity.

Furthermore, average properties can be deduced from moments of the IVDFs. Taking the first velocity moment gives the mean ion velocity

$$V_i/c_s = \frac{2\sqrt{2}}{\pi}D(\sqrt{\eta}), \tag{1.15}$$

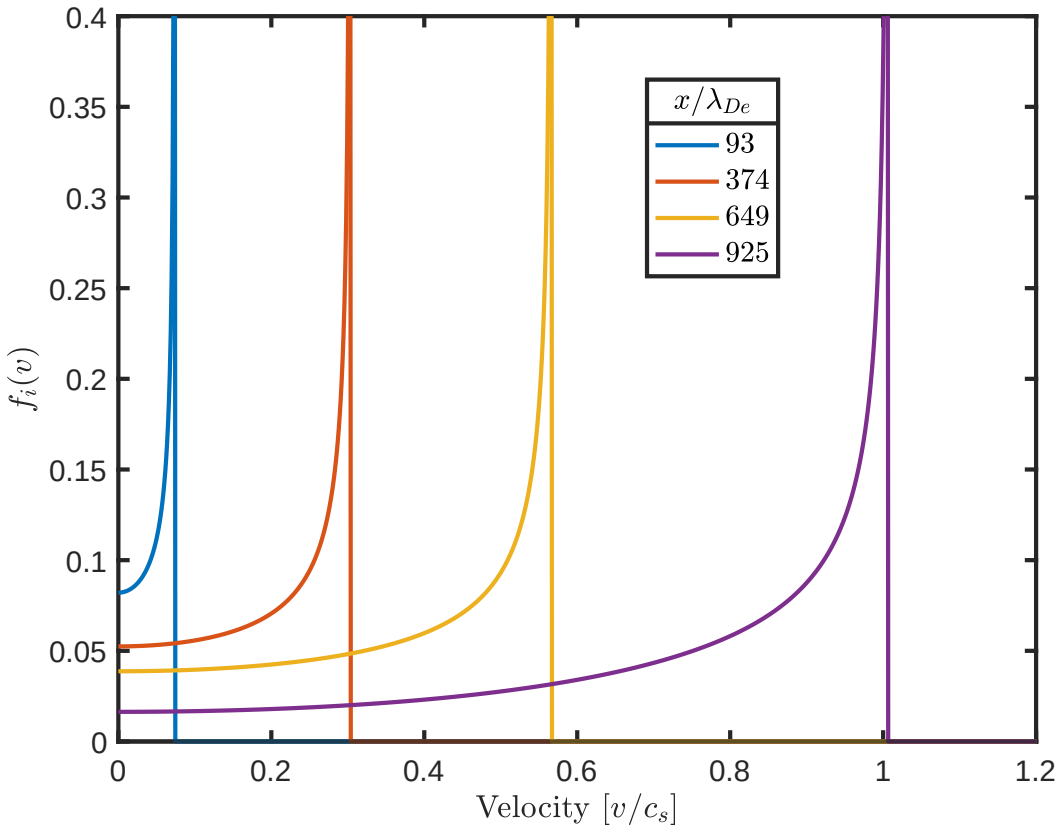

Figure 1.2: Ion velocity distributions predicted by the Tonks-Langmuir model at several different positions in a 1000 λ_{De} length presheath.

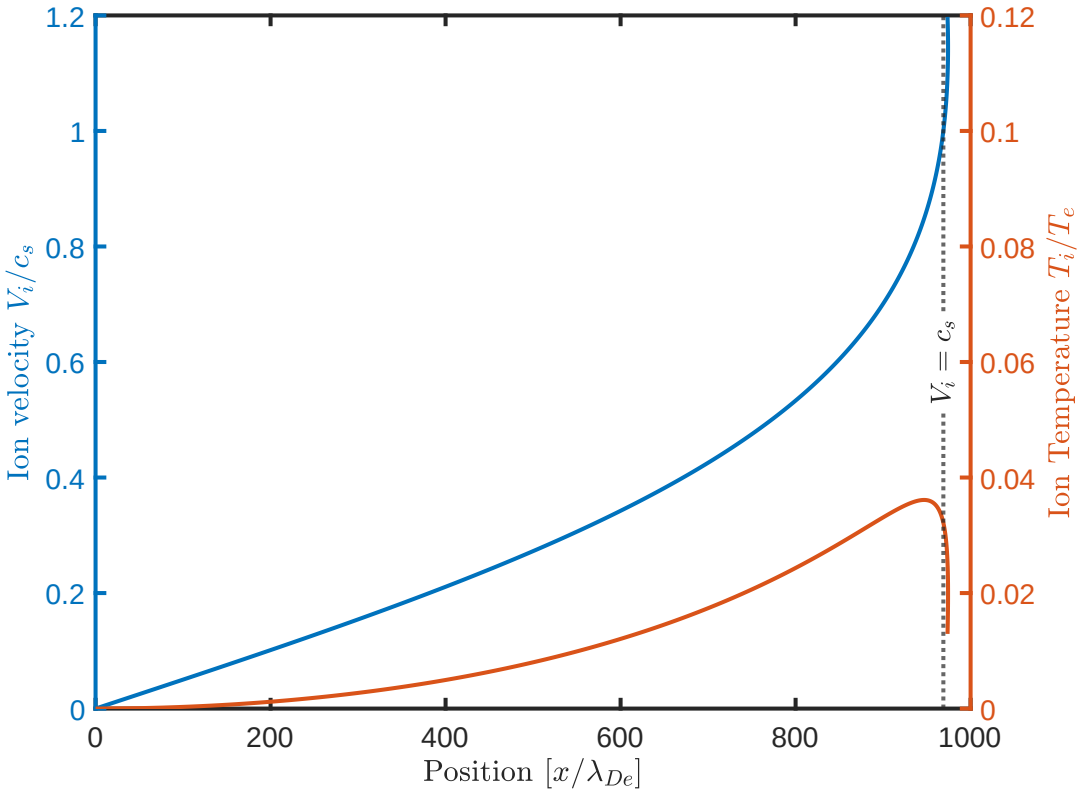

Figure 1.3: Predictions of average ion velocity and ion temperature from the Tonks-Langmuir model (Eq. (1.15) and (1.16)). Here the presheath has a length of 1000 λ_{De}. The vertical dashed line represents the sheath edge, here defined as the point where $V_i = c_s$.

and ion temperature

$$\frac{T_i}{T_e} = \frac{1}{2}(e^{\eta} - 1 - \frac{8}{\pi}D(\sqrt{\eta})). \tag{1.16}$$

The average ion velocity and temperature are plotted in Fig. 1.3. As expected the average ion velocity increases since each ion is being accelerated from rest in the same direction, irrelevant of starting position. The ion temperature is more interesting, since it increases and then begins to decrease near end of the solution. Both of these features can be seen in Fig. (1.2) as well as the peak of the IVDF moves to high velocities and the width of the IVDF increases as the sheath edge is approached. Here the ion temperature is a measure of the width or spread of the IVDFs.

The ion temperature increases since ions from anywhere upstream contribute to

the IVDF downstream leading to a wider range of ion velocities toward the sheath. Consider the IVDF at a position close to $x = 0$, effectively all the particles that contribute to this point were born nearby and so have accelerated very little, making the spread in velocities small (blue curve in Fig. (1.2)). Conversely, the IVDF at a position far to the right is made up of particles born nearby with effectively 0 velocity *and* particles born far upstream that have much higher velocities, leading to a larger spread in velocities. This effect is more pronounced as you move to the right and so the ion temperature increases to the right (purple curve in Fig. (1.2)). Furthermore, the model begins to capture another kinetic affect that that is known as *collisionless thermalization* [23] where a relatively strong electric field, usually associated with the sheath, reduces the spread in velocities between particles and so effectively lowers their temperature. The decrease in temperature is largest near point where the solution breaks down, though this may be an over prediction since the field becomes infinite at the break down point. The fact that this relatively simple model captures such kinetic effects is part of what makes it so important, when compared to fluid models, which cannot capture these effects. Ultimately, this work aims to compare this model to kinetic simulations that should capture these and other effects. With this in mind we will now compute specific values from the model that we can compare with our simulations.

Equations (1.15) and (1.16) can be evaluated at the sheath edge where $V_i = c_s$. There are two reasons for choosing this location as the sheath edge: (1) theoretical works of the collisionless plasma boundary often define the sheath edge as the point where the ions reach the sound speed making for straightforward comparisons and (2) the error at the point where $V_i = c_s$ will be less than at the point where the model has broken down completely making the model more accurate. We find that the potential associated with this definition of the sheath edge is $e\phi = 0.725T_e$. Then

we find from Eq. (1.16) that the sheath edge ion temperature is

$$T_i^{TL}(se) = 0.0161 T_e, \tag{1.17}$$

and from the Boltzmann density relation that the sheath edge density is

$$n_i^{TL}(se) = 0.4841 n_0. \tag{1.18}$$

Equation (1.17) expresses the electron-to-ion temperature ratio we would expect at the sheath edge in kinetic simulations when the ions are sourced at a much lower temperature than the electrons. However, there is an important difference between the Tonks-Langmuir model and kinetic simulations: the model does not capture time-dependent phenomenon or warm ion sources, while simulations can. For example, instabilities may be possible in the presheath and may affect the ion properties there. The theory of how instabilities couple to a plasma is discussed in section 1.3.2, while simulations including instabilities relevant to the presheath are explored in chapters II and IV. Furthermore, Eq. (1.18) expresses the edge-to-center density ratio, which should also be observable in our simulations. However, when collisions are present in the presheath the edge-to-center density ratio can change dramatically. Collisional sheath models are described in section 1.3.1.

Finally, it is important to note how experiments compare with the predictions of the low pressure, low temperature Tonks-Langmuir theory. A common experimental setup that can capture the DC presheath and sheath physics described above is a multi-dipole chamber, where plasma is generated via hot filaments and confined by a weak magnetic field at the boundaries of the chamber. The magnetic field is supplied by permanent magnets that line the chamber walls and effectively confine the hot, but diffuse, ionizing electrons. A probe that is much larger than the electron Debye length ($\sim$ 1 cm diameter) can be inserted into the plasma to represent an unmagnetized

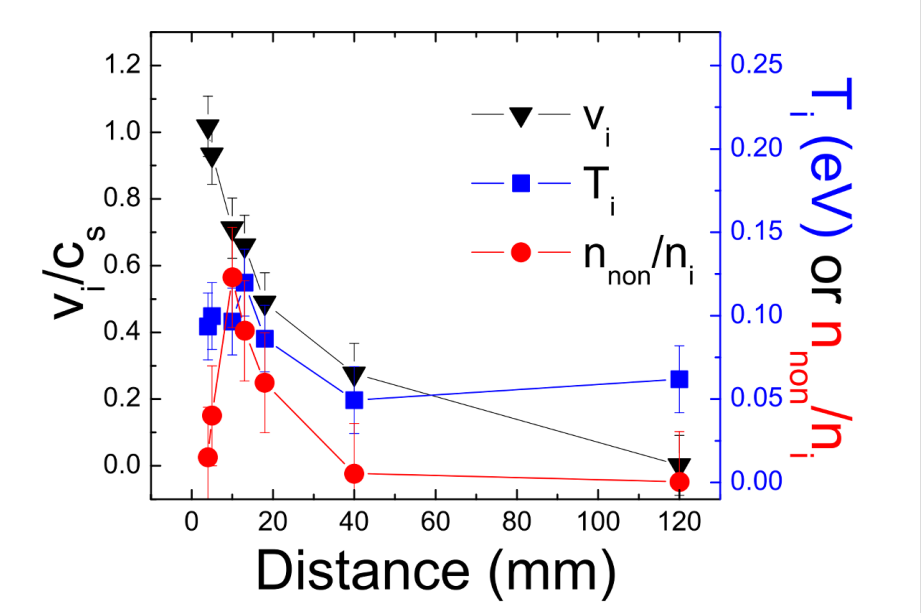

Figure 1.4: The ion temperature (blue squares), average ion velocity (black triangles), and non-thermal fraction of ions (red circles) near the sheath edge (0 mm) from LIF. The pressure is 0.08 mTorr with an electron temperature of 2.4 eV. Reprinted from [24] with permission from IOP publishing.

boundary on which a sheath and presheath can form. Then diagnostics like Langmuir probes, emissive probes, or lasers can be used to make measurements. Often the electron temperature reaches a few eV and densities of 10^{15} m^{-3} are characteristic of the bulk plasma [13, 24, 25, 26].

Laser-induced-fluorescence (LIF) is a common diagnostic technique in such systems, where a pump laser excites a certain atomic transition of a selected ion species and an emission signal is collected that can be related to the number of particles near a certain velocity via Doppler shift [25]. This effectively allows for the measurement of the ion VDF within a relatively small volume. The shortcomings of the method are related to what transitions are accessible and the signal-to-noise ratio, but are beyond the scope of this work. The most important limitation is that a good signal is hard to get in a dense, collisional systems as collisions can quench the desired emission signal.

Experiments have confirmed the validity of Bohm's criterion in single ion species plasmas, and have even been used to describe the correct criterion in multiple species

plasmas [13]. More important to this thesis are measurements of the ion temperature near the sheath edge. A measurement of the ion (Xe^+) temperature near the sheath edge was completed in [24] and has been reproduced below.

Figure 1.4 illustrates two important predictions of the models described above. Namely, that Bohm's criterion is satisfied and that the ion temperature increases near the sheath edge. The black triangles reach 1 (on the left axis) before the sheath edge, fulfilling Bohm's criterion. In addition, the blue squares show the ion temperature measured from the width of the LIF ion VDFs. In the experiments $T_e \approx 2.4$eV which, using the Tonks-Langmuir model, predicts a *maximum* ion temperature of 0.039 eV. Comparing this to Fig. 1.4, the max measured ion temperature is approximately 0.12 eV which is about 3 times higher than predicted. Even when a warm ion source is included in the theory, the theoretical prediction does not change significantly [22]. This leaves the question: what causes the excess ion heating? This question is answered in chapter II.

1.3 Extensions to the Tonks-Langmuir model

The models described in the previous section exclude the effects of collisions and instabilities. Here a collisional extension to Bohm' criterion is described along with the basic theory of instability enhanced collisions.

1.3.1 Charged-neutral collisions

Collisional models of the presheath and sheath are often based on moment (or fluid) models of the plasma. Moments of the plasma kinetic equation are taken to get a system of coupled differential equations for quantities like the density, velocity, and temperature of a specific species. These can include collisional effects in a straightforward manner. In this section, a collisional plasma model is derived, and from it a collisional Bohm criterion.

The model start from the plasma kinetic equation:

$$\{\partial_t + \mathbf{v}\cdot\partial_{\mathbf{x}} + \frac{q_s}{m_s}\mathbf{E}\cdot\partial_{\mathbf{v}}\}f_s = C(f_s) + \mathcal{S}, \tag{1.19}$$

where sources and sinks of particles besides collisions are included in $\mathcal{S}$ and collisions are included through the collision operator C. Velocity moments of Eq. (1.19) provide evolution equations for the moments of the VDF f_s.

The moments of the VDF are the density

$$n_s \equiv \int_{-\infty}^{\infty} f_s \mathrm{d}^3 v, \tag{1.20}$$

the average velocity

$$\mathbf{V}_s \equiv \frac{1}{n_s}\int_{-\infty}^{\infty} \mathbf{v} f_s \mathrm{d}^3 v, \tag{1.21}$$

the temperature (related to the pressure p_s)

$$T_s \equiv \frac{1}{n_s}\int_{-\infty}^{\infty} \frac{m_s}{3}(\mathbf{v}-\mathbf{V}_s)^2 f_s \mathrm{d}^3 v = \frac{p_s}{n_s}, \tag{1.22}$$

the stress tensor

$$\pi_s \equiv m_s \int_{-\infty}^{\infty} ((\mathbf{v}-\mathbf{V}_s)(\mathbf{v}-\mathbf{V}_s) - \frac{1}{3}(\mathbf{v}-\mathbf{V}_s)^2\mathcal{I}) f_s \mathrm{d}^3 v, \tag{1.23}$$

and the friction force density

$$\mathbf{R}_s \equiv m_s \int_{-\infty}^{\infty} \mathbf{v} C(f_s) \mathrm{d}^3 v, \tag{1.24}$$

where $C(f_s)$ is the collision operator which can include Coulomb and other types of collisions. The first two moments ($\mathbf{v}^0$ and $\mathbf{v}^1$) of Eq. (1.19) are used to extend Bohm's

criterion and include the continuity equation

$$\partial_t n_s + \partial_{\mathbf{x}} \cdot (n_s \mathbf{V}_s) = S, \tag{1.25}$$

where $S = \int_{-\infty}^{\infty} \mathcal{S} \mathrm{d}^3 v$, and momentum equation

$$m_s n_s \{\partial_t \mathbf{V}_s + \mathbf{V}_s \cdot \partial_{\mathbf{x}} \mathbf{V}_s\} = n_s q_s \mathbf{E} - \partial_{\mathbf{x}} p_s - \partial_{\mathbf{x}} \cdot \Pi_s + \mathbf{R}_s. \tag{1.26}$$

The final ingredient necessary for the derivation is a criterion on the gradient of the charge density $\rho = \sum_s q_s n_s$ at the sheath edge. This has been derived in [19] and takes the form

$$\frac{\mathrm{d}\rho}{\mathrm{d}\phi}|_{\phi=0} = \sum_s q_s \frac{\mathrm{d}n_s}{\mathrm{d}x} \leq 0. \tag{1.27}$$

This definition is derived by expanding Poisson's equation about the sheath edge where $\phi = 0$ and assumes qusineutrality implying $\rho(\phi = 0) = 0$. Thus, the first non-vanishing term in the expansion is $\frac{\mathrm{d}\rho}{\mathrm{d}\phi}$, which can be converted to a spatial gradient using the chain rule. Furthermore, any spatial variation is assumed to be along the x direction. Eq. (1.27) is a more rigorous way of defining the sheath edge as the point where quasineutrality breaks down. Now, Eq. (1.25) and Eq. (1.26) can be solved simultaneously for n_s and $\mathbf{V}_s$ and substituted into Eq. (1.27) to give

$$\sum_s q_s \frac{q_s n_s E - n_s \mathrm{d}T_s/\mathrm{d}x - \mathrm{d}\pi_s^{xx}/\mathrm{d}x - m_s V_s S + R_s}{E(m_s V_s^2 - T_s)} \geq 0, \tag{1.28}$$

where π_{xx} is the xx-component of Eq. (1.23). Equation (1.28) is a generalized Bohm criterion that includes kinetic effects as well as collisional effects (R_s). It is often the case, for a range of neutral gas pressures, that the most important terms in Eq. (1.28) are E, T_e, and R_i, which is checked with simulations in chapter III. Eliminating the other terms leaves

$$V_{i,se}/c_{\mathrm{s}} \leq \sqrt{1 - \frac{R_{in,se}}{eE_{se}n_{se}}}, \tag{1.29}$$

where $n_i \approx n_e = n_{se}$ and only electrons and a single, singly charged ion were included. Here $V_{i,se}$ is the average ion velocity at the sheath edge. In addition, only ion-neutral collisions were included and are represented by R_{in}.

An analytic form of R_{in} can be derived for certain types of collisions (e.g. elastic) when the cross section is fairly simple. A derivation of R_{in} for elastic ion-neutral collisions is included in appendix B.3. In such a case, the friction force is a function of the ion velocity at the sheath edge $V_{i,se}$

$$R_{in,se} = -m_i n V_{i,se} \frac{c_{\mathrm{s}}}{\lambda_{in}(c_{\mathrm{s}})}. \tag{1.30}$$

Upon substituting Eq. (1.30) into Eq. (1.29) one arrives at a modified Bohm criterion, which is tested against simulations in chapter III. Modification to Bohm's criterion are often used to predict the sheath width and sheath potential drop [27]. These quantities are also investigated in chapter III.

Furthermore, collisional fluid models are also an important part of models to examine the presheath region. They generally consist of a continuity equation like Eq. (1.25) and a momentum equation like Eq. (1.26). Some may include an energy equation, but this is rare for analytic models. Often the momentum equation is simplified by omitting some of the smaller terms like the stress tensor. Variations in the models arise when different forms of S and $\mathbf{R}_s$ are chosen. For example S may be a constant or proportional to the electron density, while $\mathbf{R}_s$ can be modeled by assuming a constant mean free path, constant collision frequency, or something more complicated [28]. Ultimately, to model the presheath quasineutrality is assumed ($n_i \approx n_e$) and Eqs. (1.25) and (1.26) are solved for the density or potential profile (similar to the method of the Tonks-Langmuir model). For example, assuming a

constant and uniform source rate and a constant collision frequency model for the friction force we arrive at (see section B.1)

$$n(V) = \frac{-s(1+V^2) + \sqrt{s^2(1+V^4) + 2s(s+\frac{\lambda_{\mathrm{De}}}{\lambda_{in}})V^2}}{(\lambda_{\mathrm{De}}/\lambda_{in})V^2}, \tag{1.31}$$

where $s = S\lambda_{De}/(c_s n_0)$, $V = V_i/c_s$ is the average ion velocity, and λ_{in} is the ion-neutral mean free path. The edge-to-center density ratio and presheath potential drop can be modeled from Eq. (1.31).

1.3.2 Instability-enhanced collisions

Kinetic instabilities characteristically take particle kinetic energy and convert it into field energy. Instabilities are of significant interest in plasmas where Coulomb collisions are rare since wave-particle scattering can effectively enhance Coulomb collision rates between particle species. Wave-particle scattering by instabilities had been studied in linear and non-linear settings, but often results in a theory that depends on an external input. For example, the interaction of the instability with the background plasma is the subject of quasi-linear theory, and predicts how the initially unstable VDF is altered by the instability to evolve toward a more stable configuration [8, 10]. The particle VDF is split into a gradually varying component f_0 representing the background plasma and a more quickly varying component f_1 that represents the velocity space effects of the instability. Quasi-linear theory predicts that f_0 evolves according to a diffusion equation:

$$\begin{aligned} \partial_t f_0 &= \partial_{\mathbf{v}}(\mathcal{D}(\mathbf{v},t)\partial_{\mathbf{v}} f_0) \\ \mathcal{D} &= \frac{2}{\epsilon_0}\left(\frac{q}{m}\right)^2 \int_{-\infty}^{\infty} \frac{i\mathcal{E}(\mathbf{k},t)}{\omega - \mathbf{v}\cdot\mathbf{k}} \mathrm{d}k^3, \end{aligned} \tag{1.32}$$

where $\mathcal{E}$ is the spectral density of the electric field, which measures the energy stored in waves with wavenumber k. Notably, $\mathcal{E}$ depends on time and must be provided from some other calculation or model. This restricts the utility of quasi-linear theory to cases where $\mathcal{E}$ can be estimated. The sources of wave energy can be external (like an antenna) or internal from the motion of the electron and ions in the plasma. The latter is an important source of wave energy since the plasma particles are in constant motion.

Recently, a kinetic equation was constructed for unstable plasmas, where the wave energy generated from the motion of single particles is included self consistently in the model [11, 29]. Their calculations show how the plasma kinetic equation is modified by the presence of instabilities and that the Coulomb collision rates between particles can be enhanced beyond the nominal values because of instabilities, leading to the name instability-enhanced collisions. Enhanced collision rates lead to larger than expected friction and energy exchange between species [12, 30], that alter the steady-state of the plasma in important ways. Furthermore, the modifications to the kinetic equations are consistent with the quasi-linear theory described by Eq. (1.32), but where the spectral energy is calculated self consistently from the discrete particle motion.

It is important to note that the theory of [11, 29] was designed to be applicable in a linear regime before non-linear wave effects become important. For example, their linear theory is well positioned to analyze convective instabilities since the growing wave can pass through the plasma before reaching a non-linear state. Convective instabilities are of interest to this thesis since they can be generated in the presheath by the large ion drift (ion-acoustic instabilities in chapter II) or the ambipolar electric field (chapter IV). Specifically, ion-acoustic instabilities can enhance the electron-ion collision rate in low pressure presheaths, leading to larger electron-to-ion energy transfer rates.

The instability-enhanced energy exchange rate enters into the ion (and electron) energy equations, which can be derived from the $m_s(\mathbf{v}-\mathbf{V}_s)^2/2$ moment of the kinetic equation [11, 29]. The kinetic equation derived in Refs [11, 29] can be written in the same form as Eq. (1.19), but where C has a new component representing instability enhance collisions. Ultimately, we can write the temperature evolution equation for species s (in 1D) as

$$\frac{3}{2}n_s V_s \frac{\mathrm{d}T_s}{\mathrm{d}x} + n_s T_s \frac{\mathrm{d}V_s}{\mathrm{d}x} + \frac{\mathrm{d}q_s}{\mathrm{d}x} + \pi_s^{xx}\frac{\mathrm{d}V_s}{\mathrm{d}x} = Q_c + Q_n + Q_{IE} + \mathcal{S}_2, \tag{1.33}$$

where $\mathcal{S}_2$ is the $m_s(\mathbf{v}-\mathbf{V}_s)^2/2$ moment of $\mathcal{S}$ in Eq. (1.19), Q_c is the energy exchange rate from Coulomb collisions, Q_n is the energy exchange rate from neutral collisions, and Q_{IE} is the instability-enhanced energy exchange rate. Q_{IE} includes components from like (s) and unlike species. In low temperature plasmas, Q_c is generally negligible when compared to $\mathcal{S}_2$ or Q_n, and Q_n can be negligible at low enough neutral pressures. This leaves instabilities, Q_{IE}, as a possibly non-negligible contribution. Such a case is described in chapter II.

1.4 Particle-in-cell simulations

1.4.1 Background

Even though much theoretical work was done to reduce the complexity of first principles descriptions of plasmas (e.g. the Klimintovich equation [8]) to something more manageable that still captures kinetic effects, like the plasma kinetic equation (Eq. (1.19)), solving such an equation can still present immense difficulties. For example, including physically relevant boundary conditions, like an emitting boundary, or specific atomic reactions is cumbersome. However, many of the applications of plasmas include such features, which often makes fully analytic methods intractable. Kinetic simulation techniques were developed with this in mind and have grown to

be ubiquitous tools. Simulation techniques include molecular dynamics, Vlasov and related solvers, and particle-in-cell simulations. Each has different advantages. Although Vlasov solvers have been used to study the sheath before [31, 32, 33], we utilize the PIC technique as it can simulate large scale plasmas (1,000s λ_{De}), unlike molecular dynamics, and can be easily modified to include a host of charge-neutral collisions, unlike Vlasov solvers. The following is a review of the basic numerical methods used in 1D, uniform mesh, PIC simulations. Furthermore, the method used to include charge-neutral collisions and the ability of PIC to capture instabilities is described.

A PIC simulation of a plasma calculates the trajectory of macro-particles in response to self-consistent, and applied, electric and magnetic fields. In this work we consider only electrostatic simulations, though the general principles are unchanged with a magnetic field. A macro-particle represents many (usually billions) of real particles, allowing PIC simulations to be used to model macroscopic systems containing many Debye spheres worth of particles. The fields are solved for on a fixed grid instead of pair-wise between the particles, reducing the computational expense, but introducing some nuance to the method. The grid considered here is uniform, defined by a cell size dx between grid points, and does not change during the simulation. The general algorithm follows [34]:

1. Initialize particle positions, velocities, electric field, and the grid.

2. Calculate the charge density ρ on all grid points by interpolating each macro-particle's charge to neighboring, or more distant, grid points.

3. Solve Poisson's equation on the grid for the electric field.

4. Interpolate the electric field from the grid to each particle's location and push the particle according to $F = ma = qE$.

5. Repeat steps 2-4 for N_t time steps of size dt.

The specific algorithms chosen in steps 1-4 all affect the efficiency of the simulation program and the physics that is observed.

In step 1, the initial positions and velocities are chosen for the macro-particles. In general this can be accomplished by inverse cumulative density sampling which takes uniformly distributed random number $R_i \in (0, 1)$ and converts it to a random number distributed by the chosen spatial or velocity distribution. The is the technique described in [34], and is a very general mathematical technique not specific to particle simulations. Often the spatial distribution is chosen to be uniform, but is sometimes chosen to be a monochromatic wave ($\sim \sin kx + \phi$) when studying Landau damping or instabilities. The most common initial velocity distribution is the Maxwellian, though multiple peaked VDFs can be used to study instabilities, and kappa distributions can be used in simulations of space plasmas.

In step 2, the program takes the charge of each particle, q_i, at position x_i and partitions it among a chosen set of neighboring nodes. The most common interpolation schemes in 1D are nearest grid point and linear. The former takes all of the macro-particle charge q_i and assigns it to the nearest grid point, while the latter divides q_i among the two closest grid points. Specifically, linear interpolation gives a grid point with position X_j a charge $q_i|X_j - x_i|/dx$, provided $X_j - x_i < dx$ otherwise the assigned charge is 0. In general, any interpolation scheme can be viewed as a way of smearing out the charge of a point macro-particle, making it look like the macro-particle has some shape. In fact, the charge density is transformed from a discrete distribution ρ_p of point charges to a continuous density ρ_c by

$$\rho_c(x, t) = \int \mathsf{S}(x - x')\rho_p(x', t)\mathrm{d}x', \tag{1.34}$$

where S is called the shape function and represents the interpolation scheme. For example, the particle shape for nearest grid point is a top-hat function, while the linear scheme is a triangle. Higher order interpolation schemes include grid points that

are farther from the macro-particle and lead to more complicated shape functions. In fact, high resolution simulations often implement higher order interpolation to reduce noise in the electric field [35].

Step 3 requires that the Poisson's equation be solved on the grid points using the charge density ρ_c. In a 1D simulation using a uniform mesh, the implementation is straightforward and can utilize a direct matrix solve. This is in contrast to other solution techniques that require multiple iterations to solve the linear system of equations that follows from descritizing Poisson's equation. After this is completed the electric field is known at the grid points.

Step 4 is ultimately the reverse of step 2, where the field E at the grid points is interpolated back to the particle positions. In the framework of the shape function this is

$$F_i(x,t) = \int q_i \mathsf{S}(x-x')E(x',t)\mathrm{d}x', \tag{1.35}$$

where F_i is the force on macro-particle i. Here we have assumed that the same interpolation scheme was used as in step 2. In practice, this is always the case since using different interpolation schemes for the charge and fields would result in macro-particles experiencing a self-force. Once the forces are known, the particles are moved according to $F = ma$. A common method is known as the Verlet algorithm in which the position and velocity of each particle is advanced using

$$\begin{aligned} x(t+dt) &= x(t) + v(t)dt + \frac{F[x(t)]}{m}\frac{dt^2}{2}, \\ v(t+dt) &= v(t) + \frac{dt}{2m}(F[x(t+dt)] + F[x(t)]). \end{aligned} \tag{1.36}$$

Other algorithms include the leapfrog method, which is less accurate, or a linear multistep method like Adams-Bashforth, which is more accurate but far less computationally efficient.

Step 5 is the straightforward repetition of the first steps using a times step dt for

N_t total steps. The latter is chosen so that the simulation will resolve any long time scale physics of interest. In simulations of physical devices, N_t must often be large enough that the simulation reaches a steady-state, where the average densities and energies begin to oscillate about an average value. Thus, N_t is only restricted by the physics one needs to resolve. Conversely, restrictions on the size of dt are usually based on the accuracy of the underlying numerical techniques and resolving critical physics.

As with all numerical integration techniques, the smaller dt is the smaller the error. When the method of Eq. (1.36) is used to solve for the motion of a single harmonic oscillator with frequency ω, there is no amplitude error for $dt\omega < 2$. This same criterion is applicable to PIC simulations, where electrons often oscillate with a frequency ω_{pe} in response to a potential. Thus, a standard criterion in PIC simulations is that $dt\omega_{pe} < 2$. However, a further restriction on the size of dt is set by the need to resolve the particle trajectories. Specifically, a particle should not skip over a grid cell in one time step (i.e. the trajectory should be resolved by the grid), similar to the CFL condition when solving fluid equations [36]. If the average macro-particle is expected to have a speed v_{ave} then the time step should be smaller than dx/v_{ave}. For a grid cell of size $dx \approx \lambda_{De}/M$, and average electron thermal velocity of $v_{ave} \approx Nv_{Te}$ this gives $dt\omega_{pe} < 1/(MN)$. Often M and N are at least 2 which gives us the CFL-like criterion $dt\omega_{pe} < 0.25$ which is more restrictive than that of Eq. (1.36), making it the more practical criterion to use.

Restrictions on the size of a grid cell (dx) also exist, and are the result of mitigating errors in the collective plasma motion, rather than errors in single particle trajectories [37]. First, a numerical instability associated with the finite points of the grid (called the finite grid instability) can cause significant heating of the macro-particles [34]. Effectively, the grid modifies the normal linear dielectric to include numerical modes that have positive growth rate. When the grid is small enough to resolve the Debye

length the nonphysical instability is Landau damped away, significantly reducing the heating. Ultimately, after accounting for thermal particle VDFs, this leads to a requirement that the grid spacing must resolve the electron Debye length $dx < \lambda_{De}$. A second component of numerical heating is statistical in nature. Namely, since there are only 10s-1000s of particles in each simulation cell, the motion of a single particle out of (or into) the cell causes significant fluctuations in the electric field at the neighboring grid points. The fluctuations are nonphysically large in a typical PIC simulation since there are far fewer macro-particles than physical particles. The enhanced fields couple back to the other particles in the simulation, ultimately leading to an energy gain of the particles. This form of numerical heating scales inversely with the number of macro-particles per cell and is a slower process than the numerical instability heating [38]. This form of heating can be reduced significantly, by resolving the electron Debye length and having at least $\sim 10s$ of particles per cell [38].

The following sections describe how PIC simulations can be modified to include collisions and how they can be run to resolve instabilities.

1.4.2 Direct simulation Monte-Carlo method

Collisions between charged and neutral particles are generally incorporated into PIC simulations via a Monte-Carlo method, which relies on pseudo random numbers to determine if and how the particles collide. An extremely efficient and simple method can be employed if one is not interested in the motion of the neutral particles or if the neutral gas density is not expected to change much. In such a case the Monte-Carlo collision method (MCC) can be used [39]. Conversely, if the motion of the neutral gas is of interest, it can be simulated using macro-particles just like the electrons and ions in the PIC simulation. In this case, collisions between the charged and neutral particles are included using the direct simulation Monte-Carlo method (DSMC) [40]. The DSMC method was previously integrated into the simulation code

used in this thesis, called Aleph, and is how collisions were implemented in all the simulations in this work. The DSMC algorithm was initially designed for solving the Boltzmann equation for neutral gasses in [40].

Consider elastic collisions between electrons and neutral helium atoms. The basic DSMC algorithm cycles through every pair of electrons and helium macro-particles in a given cell and uses an acceptance-rejection method to determine which pairs will collide. However, the DSMC method limits the number of pairs that can collide so that the collision rate, as determined by the Boltzmann collision operator, is not exceeded [41]. This is done by summing the time for each accepted collision, calculated as

$$\tau = \frac{2}{N n_g v_r \sigma(v_r)}, \tag{1.37}$$

where N is the number of pairs in a cell, n_g is the neutral gas density, v_r is the relative velocity between the collision pair, and σ is the cross section. Once the sum of collision times exceeds the time step (dt), no more collisions are counted, which enforces that the mean collision rate from theory is not exceeded. This is repeated across each grid cell and at each time step.

This is the basic DSMC method. However, sampling pairs one-at-a-time is computationally inefficient scaling, like N^2. A more efficient algorithm is used in Aleph, called the no-time-counter method, where the number of collision pairs is determined at the beginning of each time step from an estimate of the maximum collision frequency (calculated from the maximum v_r). Once a collision pair is accepted, the final velocities for the colliding particles are determined from the cross section data. Ideally, the differential cross section data is used to randomly sample the final velocities, while maintaining conservation of energy if applicable. However, this is rarely implemented because often only the total energy dependent cross section is available. This is also the case for the simulations in this work. In such cases, it is convenient to assume isotropic velocity scattering for the particles, in which case the final energy

of the pair is chosen from the total cross section, while the scattering angle is chosen form a uniform distribution between 0 and π radians.

The DSMC method is quite general and can be used for any type of binary collision where the Boltzmann equation would apply. In fact, the method can be used to include complicated gas and plasma chemistry into PIC simulations.

1.4.3 Resolving instability-enhanced collisions

Kinetic instabilities are commonly studied in PIC simulations since simulations provide a first-principles and detailed look how instabilities can affect plasma dynamic. In addition, simulations allow one to easily diagnose details of the instabilities since the electric field can be output with fine spatial and temporal resolution. Furthermore, simulations can capture the effects instabilities have on the plasma through both non-linear and linear phenomena. Specific to this thesis are wave-particle interactions that occur primarily during the linear growth stage of an instability, called instability-enhanced collisions. Effectively, the fluctuations of the instability can enhance the effective Coulomb collision rate of particles in the plasma.

However, PIC simulations can only self consistently capture Coulomb collisions at scales larger than the cell size [34]. This means there are effectively no Coulomb collisions in the simulations since such long range collisions are rare in low temperature plasmas. This may lead one to question whether instability enhanced collisions will be present in a PIC simulation. The answer to this question was supplied recently [42], where it was shown that instability enhanced collisions are properly represented in PIC simulations as long as waves are spatially resolved.

One can calculate a Lenard-Balescu-like collision operator that includes Coulomb and instability-enhanced collisions, for PIC simulations:

$$C_{\mathrm{PIC}} = \partial_{\mathbf{v}} \cdot \int_{-\infty}^{\infty} (\mathcal{Q}_{\mathrm{C}} + \mathcal{Q}_{\mathrm{IE}}) \left(\frac{1}{m_{s'}} \partial_{\mathbf{v}'} - \frac{1}{m_s} \partial_{\mathbf{v}} \right) f_s(\mathbf{v}) f_{s'}(\mathbf{v}') \mathrm{d}^3 v', \tag{1.38}$$

where m_s and $m_{s'}$ represent the mass of the two colliding species,

$$\mathcal{Q}_{\mathrm{C}} = \frac{2q_s^2 q_{s'}^2}{m_s} \int \frac{\mathbf{kk}}{k^4} \delta[\mathbf{k} \cdot (\mathbf{v} - \mathbf{v}')] \frac{\left|\hat{\mathsf{S}}(\mathbf{k})\right|^4}{\left|\epsilon_{\mathrm{PIC}}(\mathbf{k}, \mathbf{k} \cdot \mathbf{v})\right|^2} \mathrm{d}^3 k \tag{1.39}$$

is the Lenard Balescu collision kernel for standard Coulomb collisions in PIC and

$$\mathcal{Q}_{\mathrm{IE}} = \frac{2q_s^2 q_{s'}^2}{\pi m_s} \int \frac{\mathbf{kk}}{k^4} \sum_j \frac{\gamma_j e^{2\gamma_j t}}{\left[(\omega_j - \mathbf{k} \cdot \mathbf{v})^2 + \gamma_j^2\right]^2} \frac{\left|\hat{\mathsf{S}}(\mathbf{k})\right|^4}{\left|\partial_\omega \epsilon_{\mathrm{PIC}}\right|^2_{\omega_j}} \mathrm{d}^3 k \tag{1.40}$$

is the instability-enhanced collision kernel relevant to PIC. In Eq. (1.40) ω_j and γ_j represent the frequency and growth rate of the j-th unstable mode. Furthermore, the linear dielectric relevant to PIC is

$$\epsilon_{\mathrm{PIC}} = 1 + \sum_s \frac{q_s^2}{\epsilon_0 m_s k^2} \left|\hat{\mathsf{S}}(\mathbf{k})\right| \int \frac{\mathbf{k} \cdot \partial_{\mathbf{v}} f_s}{\omega - \mathbf{k} \cdot \mathbf{v}} \mathrm{d}^3 v, \tag{1.41}$$

where $\hat{\mathsf{S}}$ is the Fourier transform of the interpolation scheme S. Ultimately, it is the dependence of Eq. (1.41) on $\hat{\mathsf{S}}$ that leads to PIC capturing instability enhanced collisions. This form of the linear dielectric is analyzed in detail in [34].

The mathematical difference between the kernels for Coulomb collisions and instability-enhanced collisions is that the former depends on $\epsilon_{\mathrm{PIC}} \sim 1 + \hat{\mathsf{S}}^2$, while the latter depends on $\partial_\omega \epsilon_{\mathrm{PIC}} \sim \hat{\mathsf{S}}^2$. Both numerators of Eq. (1.39) and (1.40) depend strongly on $\hat{\mathsf{S}}$, which for nearest grid point and linear weighting schemes is $\sim \sin k\lambda_{De}/(k\lambda_{De})$. Notably, $\sin k\lambda_{De}/(k\lambda_{De}) \ll 1$ for $k\lambda_{De} \geq 1$, meaning that the effect of small scale phenomena are potentially reduced in either kernel. From Eq. (1.39) this translates to a reduction of the Coulomb collision rate in PIC since such collisions happen below the Debye length. However, there is no such effect for instability-enhanced collisions as $\partial_\omega \epsilon_{\mathrm{PIC}} \propto \hat{\mathsf{S}}^2$ cancels the effect of $\hat{\mathsf{S}}$ from Eq. (1.40). Thus, if the cell size is on the order of λ_{De} Coulomb collisions are not resolved, but wave-particle collisions can be resolved if the wavelength is resolved by the grid.

This shows that interpolation has a significant effect on the phenomena that can be observed in PIC simulations. Furthermore, the mathematical conclusions in [42] might fit one's expectation that the phenomena observed in PIC are those that are spatially (or temporally) resolved. Instabilities often occur at scales of several λ_{De} while particle trajectories are also resolved on this scale. Thus, it is not entirely surprising that wave-particle effects should be resolved by PIC. Conversely, Coulomb collisions occur at far smaller scales, which are often not resolved in PIC simulations.

Finally, the fact that PIC should capture instability-enhanced effects supports the findings of chapter II, where ion-acoustic instabilities are observed to heat the ions in a low temperature, low pressure plasma. In addition, it provides an avenue for understanding what effects the electron plasma wave instability can have on a plasma in chapter IV.

1.4.4 Aleph

The PIC code used throughout this thesis is Aleph [43]. Aleph is an electrostatic code that can handle unstructured meshes in 1D-3V, 2D-3V, and 3D-3V geometries. The unstructured mesh allows it to handle very high variations in spatial resolution (Debye length) for large density variations, in addition to complex geometries (bondaries). Most notably, Aleph can utilize 10,000s of individual cores on high performance computing (HPC) resources. This thesis relied on the HPC abilities of Aleph, even though the simulations used simple, uniform 1D meshes. Specifically, the simulations described in chapter II and III used on average, 144 cores running for several days. However, several high resolution simulations using more particles per cell took nearly 1,000 cores for more than a week. Conversely, the simulations described in chapter IV utilized single cores since the periodic boundary conditions have only been implemented in a serial verion of the code.

In each simulation presented here the particles moved along a single spatial di-

mension, while the velocities were tracked in three velocity dimensions for use in the DSMC method. Although there was on one spatial dimension, quantities like density were reported in m^{-3} by taking the two missing spatial dimensions to be 1 m in length when necessary. When reporting VDFs, the y and z directions were integrated over leaving $f(x, v_x)$.

Two types of boundary conditions were utilized during this thesis: absorbing (chapters II and III) and periodic (chapter IV). Absorbing boundary condition allowed presheaths and sheaths to form in the simulations, while periodic boundary conditions removed the effects of spatial variations from the simulations.

In all simulations, the requirements discussed in section 1.4.1 were met by choosing small enough time steps and grid cells so that numerical heating was negligible. Furthermore, simulations were repeated with 2-10 times more particles, smaller times steps, or smaller cells, to check that our observations did not change. This often pushed simulations to take weeks, and was possible because of the HPC capabilities of Aleph.

1.5 Publications

Much of the work presented in this thesis has recently been published in two journals; specifically, chapter II covers the research published in Physics of Plasmas [44] and chapter III covers the research published in Plasma Sources Science and Technology [45]. The work described in chapter IV is in the manuscript stage and will be submitted for review shortly.

CHAPTER II

Ion Heating Due to Ion-acoustic Instabilities

2.1 Introduction

A property of low temperature plasmas is that the ion temperature is close to room temperature, the temperature of the neutral gas ($T_n, T_i \sim 0.026$ eV), while the electron temperature can be much higher ($T_e \sim 0.1 - 100$ eV). This disparity results from a lack of thermal relaxation between the electrons and ions since the ion-electron mean free path is typically much longer than the device. However, we find that this is not always the case and that the ions can heat significantly without an external heating mechanism.

Here, particle-in-cell (PIC) simulations show that ion heating can result from the natural excitation of ion-acoustic instabilities near plasma boundaries. Specifically, ion flow through the presheath can excite ion-acoustic instabilities. Scattering from the resulting collective fluctuations acts to rapidly increase the rate of Coulomb collisions [11], and as a consequence, the electron-ion thermal relaxation rate. This results in significant ion heating so that the ion temperature takes a value between the neutral and electron temperatures ($T_n \ll T_i \ll T_e$). Its value at the sheath edge is observed to be set by the threshold (afterword "th" superscript) electron-to-ion temperature ratio required for instability $T_e/T_i \approx (T_e/T_i)^{\text{th}}$. Although the heating is mostly localized to the presheath, ion-acoustic waves reflect from the sheath and can

lead to heating in the bulk plasma as well.

This finding is particularly influential in the context of applications that use a plasma and sheath to create a high emittance ion source, such as in plasma etching of semiconductors or ion beam generation [4, 46, 47, 48]. It may also be applicable to some electric propulsion systems, where ions are accelerated to higher velocities to generate thrust, usually in the presence of hot electrons [49, 50], and to energy transport controlled by ion-acoustic instabilities in other contexts. [51, 52, 53, 54, 55, 56, 57]

The common expectation is that the ion temperature at the sheath edge is near room temperature at low neutral gas pressures, but can increase at higher pressures due to inelastic collisions (such as ionization and charge exchange) in the presheath [58, 59]. Inelastic collisions cause ions to be sourced at different locations of the presheath potential drop, causing the ion velocity distribution function (IVDF) to broaden, i.e., heat, as the sheath edge is approached. As in the previous work of Meige *et al.* [59], in our simulations we observe this to be the dominant ion heating mechanism at sufficiently high neutral pressures. However, we also find that a fundamentally different instability-enhanced heating mechanism dominates at sufficiently low neutral pressures. Ion acoustic instabilities are driven by inverse electron Landau damping [10], and therefore require a kinetic description of electrons to capture. This is presumably why the previous simulations [59], which used a Boltzmann density relation to model electrons, did not see the effect, even at low pressure.

Experiments using laser-induced fluorescence (LIF) may be able to test the proposed heating mechanism by measuring the IVDF in the presheath. Although a number of such measurements have been made [24, 58, 60], they mostly focus on plasma conditions where it is difficult to make a definitive test. For example, the measurements of Claire *et al.* [58] were made in an argon plasma with an electron temperature high enough to be expected to excite instability ($T_e = 2.5$ eV), but at a

high enough neutral gas pressure ($p_n = 0.36$ mTorr) that the associated instability-enhanced ion heating (a factor of 2-3 at this T_e) is comparable to what is expected from inelastic collisions with neutrals. Similar measurements were made by Lee *et al.* [60] in a xenon plasma, but with a low enough electron temperature ($T_e = 0.61$ eV) that the instability may not have been excited. The most pertinent measurements are those by Yip *et al.* [24] made at a low neutral pressure ($p_n = 0.08$ mTorr) and high enough electron temperature ($T_e = 2.4$ eV). Indeed, these seem to show evidence of ion heating in the presheath. As will be shown in Sec. 2.3, the measured ion temperature profile throughout the presheath agrees well with our simulations; including a factor of approximately 4 heating of ions near the sheath edge (compared to room temperature). Although the existing experiments are consistent with the simulations, they were not designed to test the proposed instability-enhanced ion heating. An ideal test would vary the electron temperature across its threshold value in a system where the neutral pressure remained sufficiently small ($p_n \lesssim 0.1$ mTorr). Such a test would demonstrate whether the instabilities and associated ion heating transition at the predicted threshold of the unstable regime. This motivates future experiments to explore lower neutral pressures and higher electron temperatures.

The existence of ion-acoustic instabilities in the presheath has been discussed in a number of recent works. One of the first theories suggested that these instabilities can rapidly thermalize electrons and may contribute to resolving Langmuir's paradox [61]. Shortly afterward, it was suggested that they also rapidly thermalize ions near the sheath edge as inelastic collisions cause the IVDF to become distorted away from Maxwellian in the presheath [29]. This latter prediction was tested experimentally by Yip *et al.* [24] using LIF measurements. These measurements showed good agreement between the degree of thermalization and the predicted instability boundary as neutral pressure was varied. However, they did not directly probe the instability. The first direct measurements of ion-acoustic instabilities in the presheath were provided by

recent LIF measurements that leveraged advancements in single photon counting and large collection optics [25]. These confirmed that ion-acoustic instabilities are present in the presheath and also suggested that the excited waves reflect from the sheath, but did not investigate ion heating.

Here, we show results from tests of the predicted instability heating using particle-in-cell, direct simulation Monte Carlo (PIC-DSMC) simulations. Our 1D-3V simulations applied absorbing boundary conditions on both the left and right boundary causing sheaths to form. Ions and electrons were sourced uniformly and at equal rates throughout the domain, with the ions sourced at room temperature ($T_i^s = 0.026$ eV) and the electrons sourced at temperatures ranging from $T_e^s = 0.1 - 100$ eV. To better assess simulation results (especially noise levels), simulations of uniform plasmas in a specular (reflecting) box with similar plasma parameters were also conducted for comparison. The ion temperature was computed from time-averaged IVDFs and the presence of instabilities was examined by comparing the fraction of energy stored in fluctuations that were ion-acoustic in a nominally stable sheath configuration, an unstable sheath configuration, and a uniform configuration. The energy stored in fluctuations was computed from fluctuations in the charge density.

Results show that instabilities are excited in the presheath, but not in the uniform plasma. The spectral energy density indicates that a significant fraction of the wave power is reflected from the presheath, in agreement with the suggestion made by Hood *et al.* [25] based on experimental measurements. Ion heating was also observed to be associated with ion-acoustic instabilities. No heating was observed at conditions where instabilities were expected to be absent based on linear theory, but heating near the sheath edge was so significant in the presence of instabilities that the temperature ratio could not significantly exceed the threshold condition for instability $T_e/T_i \approx (T_e/T_i)^{\text{th}}$. This led to a "stiff" boundary condition where the electron-to-ion temperature ratio was locked to the threshold value at the sheath edge. For large

electron temperatures ($T_e \gtrsim 10$ eV), this led to ion temperatures more than an order of magnitude above room temperature near the sheath edge. This rapid ion heating was found to be associated with a significant increase in the electron-ion energy relaxation rate associated with instability-enhanced collisions. This was confirmed by computing the residual of the steady-state ion energy balance equation, which corresponds to the energy moment of the collision operator. Spatial profiles of this term show that the heating is greatest near the sheath edge, but also extends into the bulk plasma. At sufficiently high neutral pressure and low electron temperature, the instability was not present and ion heating was instead found to be controlled by inelastic (ionization) collisions in the presheath.

We also find that the instability-enhanced heating results in a drastically different distribution of ion energy parallel or perpendicular to the single spatial dimension of the simulations. Since the waves are confined to a single spatial dimension, the associated instability-enhanced relaxation appears to be as well. This leads to highly anisotropic IVDFs with a much larger parallel temperature than perpendicular temperature.

2.2 Simulation setup

Simulations were conducted using the electrostatic PIC-DSMC code Aleph [43]. They used a 1D domain in space, 3D domain in velocity phase-space, and a uniform mesh. A presheath was simulated by applying absorbing boundary conditions at each domain boundary and continuously sourcing electrons and ions uniformly throughout the domain from Maxwellian distributions with respective temperatures T_e^s and T_i^s. Although, this introduces particles into the sheath, such events are expected to be rare and nearly all ions loaded directly into the sheath will not enter the presheath. A uniform source approximates plasma generation in multidipole devices [24, 25, 58, 60], where the primary electrons responsible for ionization are expected to have a close to

uniform density.

Reference to the electron source temperature (T_e^s) will be made often in this work as the independent variable we change to study situations where the ion-acoustic instabilities are or are not present. However, as a result of losses to the wall the measured electron temperature in a given simulation is slightly lower (at most 20% lower) than the source temperature; see Tbl. 2.1. Although they are not simulated, two dimensions perpendicular to the simulated domain are taken to have length 1m when reporting quantities like densities and rate-densities. This is reflected in Table 2.1 and throughout the remainder of this work.

In each simulation, data were analyzed after the plasma had evolved sufficiently long to reach a steady-state (approximately 600 μs which represents the time needed for a thermal ion to transit the domain), where the number of ions lost to the walls balanced those sourced in the domain. The primary quantity analyzed in steady-state was the ion temperature. Here, "ion temperature" refers to the temperature moment calculated from the full 3V velocity distribution function,

$$T_i = \frac{m_i}{3n_i} \int (\mathbf{v} - \mathbf{V}_i)^2 f_i(\mathbf{v}) \, \mathrm{d}^3 v \,, \tag{2.1}$$

where m_i is the ion mass, n_i is the ion number density, $f_i(\mathbf{v})$ is the IVDF, and $\mathbf{V}_i = \frac{1}{n_i} \int \mathbf{v} f_i(\mathbf{v}) \, \mathrm{d}^3 v$ is the ion flow velocity. We will later also utilize 1V temperatures from the reduced velocity distribution functions (e.g., $f_i^x(v_x) = \int f_i(\mathbf{v}) \mathrm{d}v_y \mathrm{d}v_z$),

$$T_i^x = \frac{m_i}{n_i} \int (v_x - V_i^x)^2 f_i^x(v_x) \, \mathrm{d}v_x \,, \tag{2.2}$$

where $V_i^x = \frac{1}{n_i} \int v_x f_i^x(v_x) \, \mathrm{d}v_x$. We define $T_i^{\parallel} = T_i^x$ to be the parallel temperature and $T_i^{\perp} = T_i^y$ to be the perpendicular temperature. All simulated quantities were effectively equal in the y and z directions since there was no spatial variation in either direction. The 3V temperature can be computed from the 1V temperatures

$T_e^s(eV)$	$T_e(eV)$	$n_0(\#/m^3)$	$R^s(\#/m^3/s)$
0.1	0.08	1×10^{13}	3.1×10^{16}
0.2	0.16	2×10^{13}	8.76×10^{16}
0.5	0.41	5×10^{13}	3.47×10^{17}
0.8	0.65	8×10^{13}	7.01×10^{17}
1.5	1.25	1.5×10^{14}	1.8×10^{18}
3	2.58	3×10^{14}	5.09×10^{18}
6	5.40	6×10^{14}	1.44×10^{19}
12	11.50	1.2×10^{15}	4.08×10^{19}
24	25.10	2.4×10^{15}	1.15×10^{20}
48	42.80	4.8×10^{15}	3.26×10^{20}

Table 2.1: Simulation parameters. Here T_e is the simulated electron temperature in the middle of the domain. The simulation density was chosen to keep $dx/\lambda_{De} = 0.42$ constant while the electron source temperature was increased. R^s is the rate-density at which electrons and ions were sourced in the simulation. In section III B, simulations A and B refer to the rows where $T_e^s = 6$ eV and $T_e^s = 0.1$ eV respectively.

$T_i = (T_i^x + T_i^y + T_i^z)/3 = (T_i^{\parallel}/3 + 2T_i^{\perp}/3)$.

Of specific importance is the ion temperature measured at the sheath edge. Here, we define the sheath edge as the position where the charge density first exceeds 5% of the average ion density. This value was chosen since it was the smallest value we could resolve with the data from each simulation. The sheath edge position is nearly the same in each of the simulations in Table 2.1 at 0.496 m.

The 1D spatial grid was composed of 1600 cells of length $dx = 3.125 \times 10^{-4}$ m, resulting in a total domain length of $L = 0.5$ m, which ensured that the Debye length was resolved. The steady-state density was changed (via the source rate) along with T_e^s to maintain the same electron Debye length ($\lambda_{De} = 7.43 \times 10^{-4}$ m). This was done so that the same spatial grid could be used in each simulation. In an experimental test of the instability heating mechanism such control of the plasma density would

not be necessary. The steady-state densities of each simulation are summarized in Table 2.1 The average number of computational particles per cell in the center of each simulation was 30 for each species and decreased to 15 near the sheath edge for computational electrons and ions. Fewer computational electrons and ions were found in the sheath; however, this is not expected to affect our measurements in the presheath since ions in the sheath quickly exit the simulations. For simulations with $T_e^s < 24$ eV, a time step of 1.1×10^{-10} s was chosen to meet a CFL-like condition, so that an electron with velocity lower than $2v_{Te} = \sqrt{8k_B T_e/m_e}$ does not cross an entire spatial cell in one time step [36]. For $T_e^s > 24$ eV, a time step of 2.5×10^{-11} s was chosen.

The plasma was assumed to be generated from pure helium, and to be singly ionized. Plasma parameters were chosen to match those in the low-temperature plasma experiments commonly used to study sheaths: $T_i^s = 0.026$ eV, $n \approx 5 \times 10^{15}$ m^{-3} [24, 25, 58]. The neutral pressure was varied in order to study different regimes of ion-acoustic wave damping. Ion-neutral and electron-neutral elastic collisions were modeled by way of the DSMC method [40]. Cross sections for both interactions were from the Phelps database provided by LXCat [62, 63, 64, 65]. No explicit method, like DSMC, was used to model Coulomb collisions in the simulations. However, Coulomb collisions occurring over large enough distances to be resolved by the grid are expected to be included implicitly in the simulations.

2.3 Results at low pressure

2.3.1 Ion heating

Figure 2.1 illustrates the most notable result, which is the observation of ion heating near the sheath edge (vertical line) at low pressure ($p_n = 0.01$ mTorr) when the source electron temperature was sufficiently high. The heating is mostly localized to

near the sheath edge, but the ion temperature in the bulk plasma is also well above room temperature. Ion heating is surprising because the only energy input is the kinetic energy at which the electrons and ions are sourced. Ion heating to above room temperature requires a mechanism for energy transfer from electrons to ions. However, the collisional electron-ion energy relaxation rate based on Coulomb collisions is expected to be negligible. Using an estimate based on the standard Coulomb collision frequency [66], the mean free path for electron-ion energy equilibration is thousands of meters at these conditions. Furthermore, since the simulations do not include an explicit Coulomb collision model only long-range interactions resolved by the grid will be included. Since there are only about 2 grid points per Debye length, Coulomb collisions that are implicitly simulated are expected to be extremely rare (in the absence of instability).

Some ion heating near the sheath edge is expected due to the interaction between the flowing ion distribution and the stationary background neutrals [59]. However, this effect is negligible at the low pressure of these simulations since the estimated ion-neutral collision mean free path is approximately 10 m. It also does not contribute to heating in the bulk plasma. Alternatively, the time averaged IVDF could broaden (i.e. heat) if the IVDF were to oscillate in velocity space on a shorter time scale than the average. We find that this is not a significant source of heating in our simulations when we compare snapshots of the IVDF that resolve the ion plasma period.

The simulation data appear to indicate that the source of ion heating is enhanced electron-ion energy exchange resulting from ion-acoustic instabilities near the sheath edge, which extends into the plasma due to wave reflection from the sheath. A number of observations provide evidence for this.

First, the parameters at which heating is observed seem to correspond well with the conditions at which the linear dispersion relation for ion-acoustic instabilities predicts instability in the presheath. The threshold for exciting the instability can be

estimated from the ion-acoustic dispersion relation, which has real frequency

$$\omega_r = kV_i^x - \frac{kc_s}{\sqrt{1+k^2\lambda_{De}^2}} \tag{2.3}$$

and growth rate [10]

$$\gamma = \frac{-kc_s\sqrt{\pi/8}}{(1+k^2\lambda_{De}^2)^2}\left[\left(\frac{T_e}{T_i}\right)^{3/2}\exp\left\{-\frac{T_e/T_i}{2(1+k^2\lambda_{De}^2)}\right\} + \sqrt{\frac{m_e}{m_i}}\left(1-\frac{V_i^x}{c_s}\sqrt{1+k^2\lambda_{De}^2}\right)\right]. \tag{2.4}$$

Here, k is the wavenumber, $c_s = \sqrt{k_B T_e/m_i}$ is the ion sound speed, and $\lambda_{De} = \sqrt{\epsilon_o k_B T_e/e^2 n_e}$ is the electron Debye length. The change in density between simulations with different electron source temperatures does not affect this prediction since the density only appears in the Debye length, which is held constant. The threshold temperature ratio decreases with increasing flow velocity and reaches a value of $(T_e/T_i)^{\text{th}} \approx 28$ when the flow speed reaches its maximum value in the presheath, which is approximately the sound speed. This estimation corresponds to $T_e^{\text{th}} = 0.7$ eV if the ions have the source temperature, $T_i = 0.026$ eV. In a plasma with heavier ions the threshold temperature ratio increases slightly: 30 for argon, 30.3 for xenon, and 30.8 for krypton.

Of the four conditions shown in Fig. 2.1, the two cases with source electron temperatures above the predicted threshold ($T_e^s = 3$ eV and $T_e^s = 12$ eV) both clearly exhibit significant heating. No heating is observed in the case with source electron temperature well below the threshold ($T_e^s = 0.1$ eV), though some cooling is observed as a result of losses to the walls. The remaining simulation has a source temperature close to the threshold ($T_e^s = 0.5$ eV) and exhibits minor heating near the sheath edge. The heating may be the result of instabilities since the source temperature is close to the estimated threshold value.

Second, if the source temperature ratio is high enough to expect instability in the

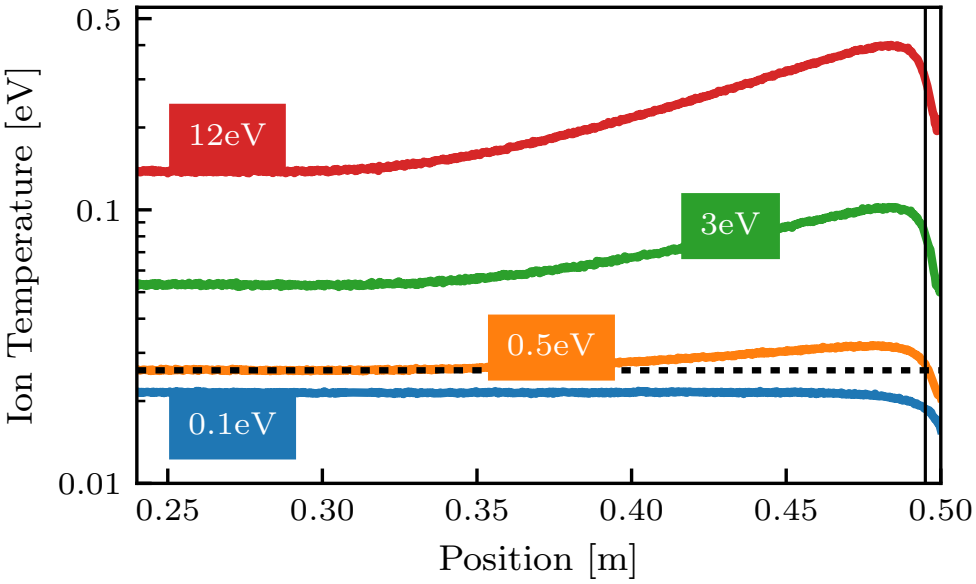

Figure 2.1: Spatial distribution of ion temperature from simulations with a neutral pressure $p = 0.01$ mTorr and four values of the electron source temperature (T_e^s) indicated in the boxes. The solid vertical line represents the sheath edge, while the horizontal dashed line represents the ion source temperature $T_i^s = 0.026$ eV.

presheath, the observed temperature ratio at the sheath edge (subscript "se") takes a value approximately equal to the instability threshold: $(T_e/T_i)_{\rm se} \approx (T_e/T_i)^{\rm th}$; as depicted by the horizontal dashed line in Fig. 2.2. Here, the orange line represents the source temperature ratio T_e^s/T_i^s, which would also be the expected temperature ratio at the sheath edge in the absence of any ion heating (or cooling). In addition, some ion heating is expected in the presheath due to the fact that ions are sourced at different values of the plasma potential throughout the presheath; as in the classical Tonks-Langmuir model [5] and in detail in chapter I. The green line represents the sheath edge temperature ratio predicted by the Tonks-Langmuir (TL) model, where $(T_e/T_i)_{\rm se}^{TL} = 3(1/25 + 2T_i^s/T_e)^{-1} \approx 75$ was used to convert the 1V TL prediction to the 3V of our simulations. Since the ion source is cold in the TL model, its prediction only applies to simulations where $T_e^s/T_i^s >> 1$. It is important to note that the TL model, even with a warm ion source, does not predict heating in the center of the

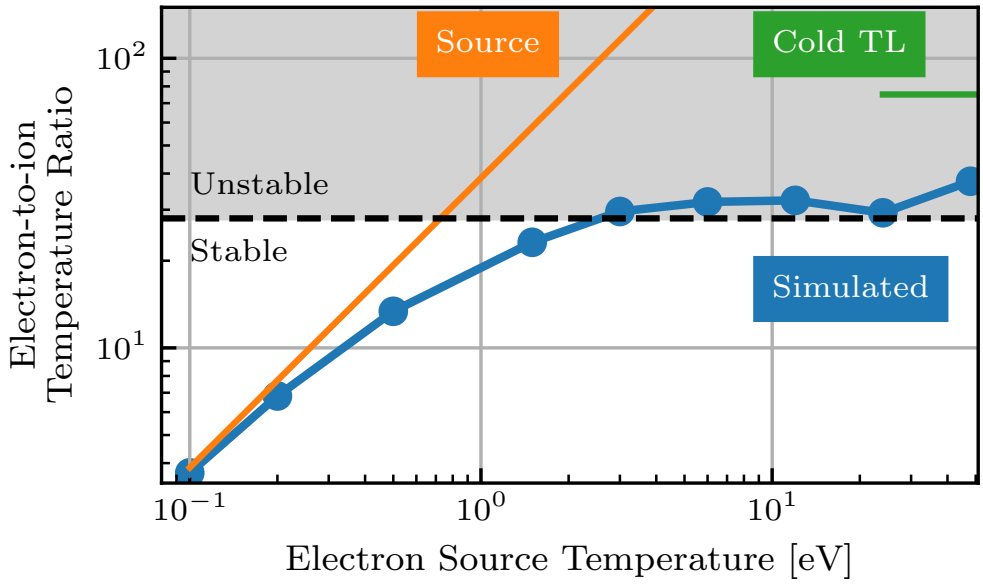

Figure 2.2: Observed electron-to-ion temperature ratio at the sheath edge (blue circles) as the electron source temperature (T_e^s) is varied. The dashed line represents the predicted threshold for instability from Eq. (2.4), and the orange line represents the source temperature ratio (T_e^s/T_i^s). The green line represents the temperature ratio at the sheath edge predicted by the Tonks-Langmuir model.

domain [22] and does not explain the observed kinetic energy balance of ions through the domain; as will be explained in Sec. 2.3.3.

Instead of following the orange line, or locking to the green line, the observed temperature ratio at the sheath edge (blue dots) locks to the threshold value, $(T_e/T_i)^{\text{th}} \approx 28$, when the source electron temperature (T_e^s) exceeds the instability threshold ($T_e^{\text{th}} \approx 0.7$ eV). This implies that the plasma cannot significantly enter an unstable parameter regime.

Third, when instability is predicted, the observed ion heating extends far enough into the presheath that the plasma does not significantly enter the unstable parameter regime. Fig. 2.3 shows the ion flow velocity and temperature ratio as a function of position in each of the four simulations from Fig. 2.1. In each simulation the ions flow toward the sheath edge with increasing velocity until they satisfy the Bohm criterion with $V_i^x/c_s = 1$. The lines are expected to be purely vertical in the absence of ion (or

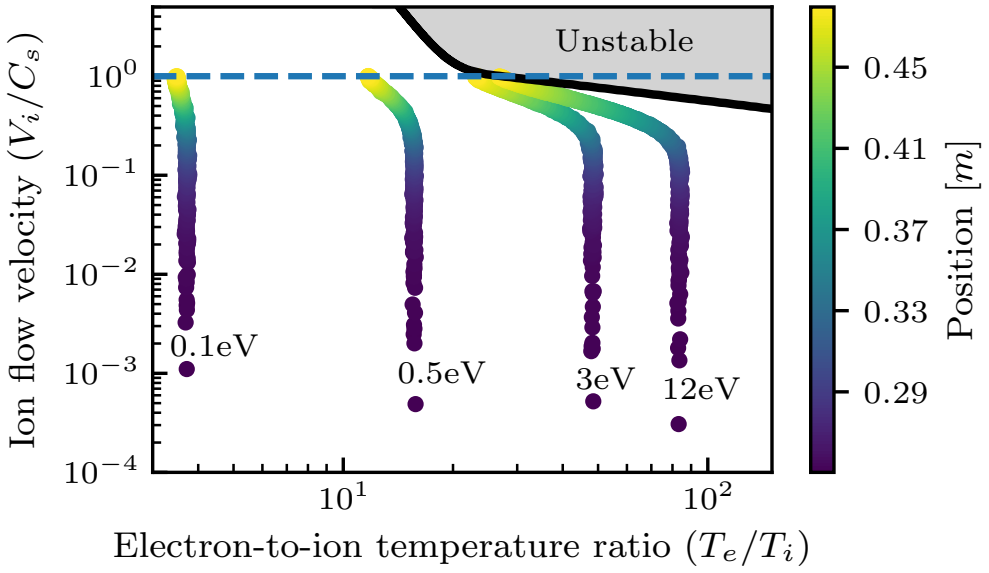

Figure 2.3: Ion flow speed (V_i^x/c_s) and electron-to-ion temperature ratio (T_e/T_i) through the presheath from simulations with varying electron source temperatures (T_e^s) indicated by the numbers in the figure. The dashed line indicates the sheath edge, where the Bohm criterion is met, $V_i^x/c_s = 1$, and the shaded region indicates parameters predicted to be ion-acoustic unstable according to Eq. (2.4).

electron) heating. As expected, a nearly vertical line is observed when the electron source temperature is in the stable region ($T_e^s = 0.1$ eV). However, when the electron source temperature is high enough that isothermal ions would lead to instability near the sheath edge ($T_e^s = 3$ eV and $T_e^s = 12$ eV), the ions are observed to heat in the presheath well before reaching the instability boundary. Ions reach the instability boundary at the sheath edge, where the temperature ratio takes the universal value associated with the intersection of the Bohm criterion ($V_i^x = c_s$) and the instability threshold. The fact that the ions heat further into the presheath than the location at which instability is predicted suggests that the excited ion-acoustic waves may reflect from the sheath and propagate back through the presheath and into the bulk plasma. Further evidence for this will be shown in Sec. 2.3.2.

The observed ion heating leads to a significant temperature anisotropy in the presheath. In particular, Figs. 2.4 and 2.5 show that the ion heating is entirely

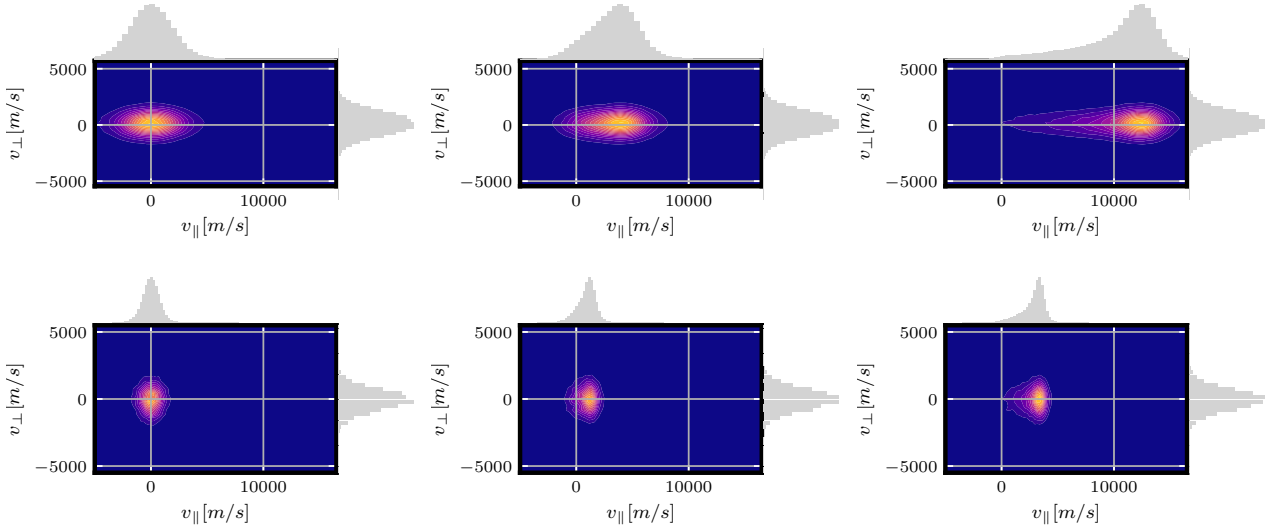

Figure 2.4: IVDFs in the $v_\perp$-$v_\parallel$ (v_y-v_x) plane from simulations with a high electron source temperature ($T_e^s = 6$ eV, top row) and a low electron source temperature ($T_e^s = 0.5$ eV, bottom row). Each is plotted at three different locations from left to right: middle of the domain (0.25 m), presheath (0.37 m), and sheath edge (0.49 m).

constrained to the single dimension of the spatial domain. The IVDFs shown in Fig. 2.4 illustrate that the ion temperature remains isotropic (or nearly so) throughout the presheath in the case where instability is predicted to be absent (see the $T_e^s = 0.5$ eV case). In contrast, the IVDF spreads significantly in the parallel dimension when instability is predicted ($T_e^s = 6$ eV). It is noteworthy that the ion-acoustic group velocity lies below the peak of the IVDF, on the low-velocity tail, and is the region of velocity phase-space at which wave-particle scattering is expected to be most frequent. In each of the 6 panels of Fig. 2.4, the reduced perpendicular IVDFs are nearly the same, demonstrating that the perpendicular IVDF is not affected. Additionally, the perpendicular IVDF does not evolve significantly throughout the presheath. These observations are consistent with wave-particle scattering, which would be expected to be confined to the single dimension in which the wave exists in these 1D simulations. The fact that the simulations are 1D-3V may preclude any affects to the perpendicular IVDF by the waves, which would be expected to spread in 3 dimensions in reality.

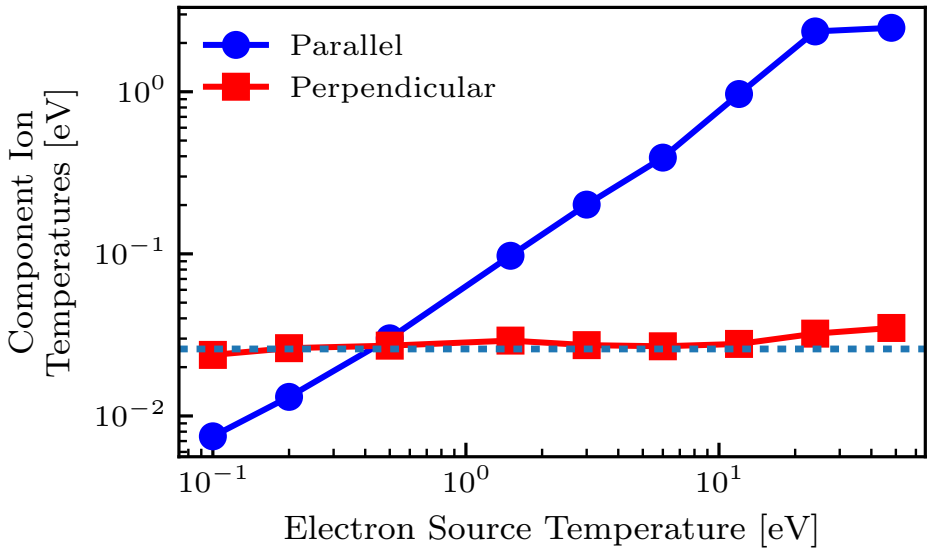

Figure 2.5: Parallel and perpendicular components of the ion temperature as a function of the electron source temperature (T_e^s). The dashed line indicates the ion source temperature ($T_i^s = 0.026$ eV).

Studying this will require simulations in 2D or 3D. Preliminary 2D simulations (two absorbing boundaries and two reflecting) are shown in Appendix A and indicates that the instability heating still occurs in 2D. Interestingly, the heating still occurs in the parallel direction with the sheaths, while significant heating also occurs along the perpendicular direction.

Aggregate data showing the parallel and perpendicular ion temperatures at the sheath edge are shown in Fig. 2.5. This shows a consistent story with the IVDFs, demonstrating that the ion heating is constrained to the parallel direction. The reason the parallel temperature dips below the source temperature for low T_e^s is because the boundaries provide an energy sink for ions that does not exist in the perpendicular directions. In the absence of the ion-ion Coulomb collisions required to thermalize the distribution, an anisotopy forms with a higher perpendicular temperature. This effect is not noticeable at higher T_e^s where the instability heating becomes significant and dominates the cooling effect.

Finally, we add that these simulation results compare well with the LIF measure-

ments of Yip *et al.* [24], which are plotted in Fig. 1.4 in chapter I. Even though the experiments used a xenon plasma, the threshold electron-to-ion temperature increases only slightly to 30.3 compared to 28 for helium. This means that for a given electron temperature (e.g., 3 eV) we should expect the ion temperature at the sheath edge to decrease from 0.107 eV in a helium plasma to 0.099 eV in xenon. In particular, compare the simulation using $T_e^s = 3$ eV from Fig. 2.1 with the measured ion temperature profile in Fig. 5 from Ref. [24], which was obtained in a plasma with an electron temperature of $T_e \approx 2.4$ eV and a neutral pressure of 0.08 mTorr. The electron temperature in this comparison is close enough that we expect similar results for the ion temperature profile, and the neutral pressure in the experiment is low enough that we expect the instability to not be affected by neutral damping. The ion temperature profile in the simulation is consistent with that measured in the experiment. In both, the ion temperature near the sheath edge is 0.1 eV, which is significantly higher than the room temperature ion source. Similarly, in the experiment the ion temperature reported farthest from the sheath was ≈ 0.05 eV, which is close to the value of 0.053 eV observed at the center of the domain in our simulation.

2.3.2 Ion-acoustic instabilities

The presence of instabilities are expected to enhance the electrostatic fluctuation level above the thermal level. To investigate this, we compare the fraction of fluctuations that are ion-acoustic (those with k and ω near that of Eq. (2.3)) from a simulation where the ion acoustic instabilities are expected (simulation A: $T_e^s = 6$ eV) to one where they are not (simulation B: $T_e^s = 0.1$ eV); see Fig. 2.6. The results show a higher fraction of ion-acoustic fluctuations in case A, which matches the expectation that ion-acoustic instabilities enhance coherent ion-acoustic fluctuations. Furthermore, the sheath simulations are compared with a simulation of a uniform plasma (simulation C), which exhibits only thermal fluctuations.

Ion-acoustic fluctuations are expected even in simulations where no instabilities or presheaths are present. We designed the uniform simulation to check that the simulated fluctuation level matches the theoretical level for a uniform plasma. The simulation utilized reflecting boundary conditions for all particles at the walls and fixed the potential to 0 V there as well. The same average number of particles per cell was used in the uniform simulation as in the presheath simulations, so that the statistical noise would be the same. The density and electron temperature were chosen to be 6×10^{14} m^{-3} and 6 eV. However, numerical heating is noticeable in the simulation since it is a closed system. The time averaged electron temperature is higher (12 eV) than the initial temperature (6 eV) since the duration of simulation C extends over at least several microseconds (thousands of ω_{pe}^{-1}) to acquire enough data for the analysis. The acquisition time for the uniform simulation is shorter than the presheath simulations, which results in a more granular image in Fig. 2.6 (g).

Fluctuations in each simulation were analyzed using 2D (space and time) Fourier transforms of the ion density (density spectrum) between a point in the presheath (0.447 m) and the presheath-sheath boundary (0.496 m). Fig. 2.6 shows the logarithm of the ion density spectrum near the right boundary in simulation A (a), B (d), and C (g). The color axis in each plot was set to range from the maximum spectral value down to 100 times less than the maximum since the maximum varies between simulations. We identified ion-acoustic modes in each simulation by comparing the density spectrum to the theoretical dispersion of ion-acoustic modes from Eq. (2.3). The white lines denote the real frequency calculated from the average densities, temperatures, and velocities at 0.447m (dashed) and 0.496m (solid). We see that in each simulation some of the fluctuations are ion-acoustic since they fall within the predicted dispersion relation curves, while part of the signal does not and is representative of *thermal noise*, defined as in Dieckmann *et. al.* [67]

Ion-acoustic instabilities are expected to increase the ion-acoustic fluctuation level

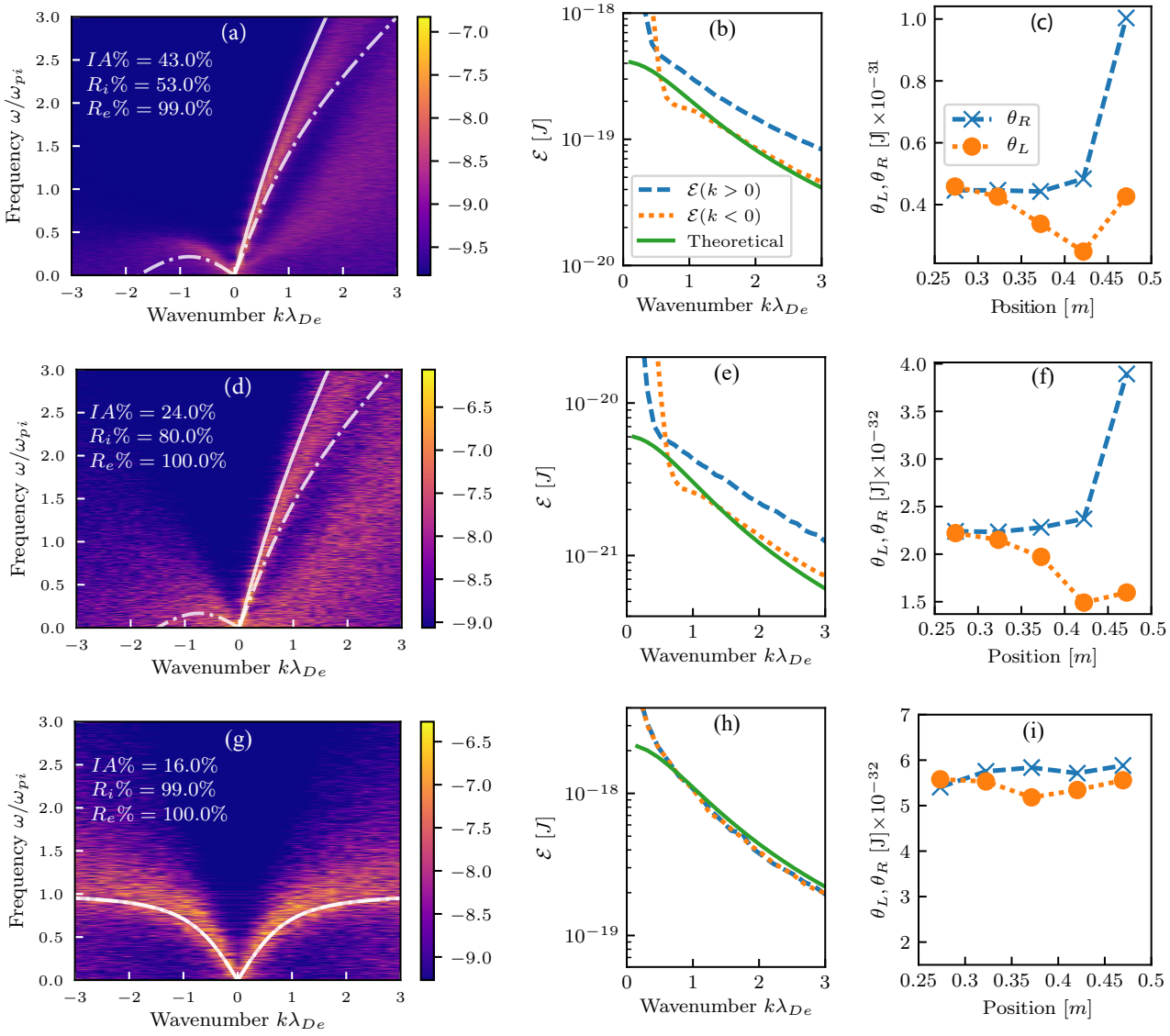

Figure 2.6: Fourier transform of ion density fluctuations ($\log_{10}((\delta n_i/n_i)(k,\omega))$) in simulations A [$T_e^s = 6$ eV: (a)], B [$T_e^s = 0.1$ eV: (d)], and C [uniform: (g)]. White dashed and solid lines indicate the real part of the ion-acoustic dispersion relation (Eq. (2.3)) calculated using data at 0.447 m and 0.496 m, respectively. $IA\%$ denotes the percent of the signal that is ion-acoustic, $R_i\%$ is the reflection coefficient of wave energy carried by ions from the sheath, and $R_e\%$ is that for electrons. Panels (b), (e), and (h) show the spectral energy between 0.447 m and 0.496 m calculated using Eq. (2.6) for $k > 0$ (dashed) and $k < 0$ (dotted) in simulations A,B, and C. The solid line represents the theoretical prediction from Eq. (2.7). (c,f,i) show profiles of the energy per particle carried by right- (crosses) and left- (circles) moving ion-acoustic modes in simulations A, B, and C

above the thermal noise level represented by the uniform simulation. However, the thermal noise level depends on the electron temperature [68] and numerical heating makes it difficult to match the electron temperature of simulation C to that of either A or B. For this reason, we compare the fraction of the total energy stored in the ion-acoustic fluctuations rather than the absolute fluctuation levels. The fraction of energy that is ion-acoustic was calculated as

$$IA\% = \frac{\int_{IA} \hat{\rho}^2/(2\epsilon_0 k^2)\,\mathrm{d}k\,\mathrm{d}\omega}{\int \hat{\rho}^2/(2\epsilon_0 k^2)\,\mathrm{d}k\,\mathrm{d}\omega}, \tag{2.5}$$

where $\hat{\rho}$ is the charge density spectrum, ϵ_0 is the permitivity of free space, and the integral in the numerator is carried out only over ion-acoustic modes. Referencing Fig. 2.6 (a,d,g), the range of the "IA" integral includes values up to $0.3\omega_{pi}$ greater and less than the frequency range predicted by the linear dispersion relation (solid and dashed white lines). This was done to exclude the part of the signal that clearly does not fall within the ion-acoustic lines (e.g. signal in the bottom right of (a) and (d)). It includes only positive values of the frequency and does not include any part of the signal with $|k\lambda_{De}| < 0.1$ as this represents the smallest wavenumber that could be resolved. The fraction of the total energy that is ion-acoustic is reported in each of the spectrum plots and is noticeably higher in simulation A ($IA\% = 43\%$) compared to B (24%) or C (16%). The higher ion-acoustic wave energy fraction in simulation A compared to B is consistent with the prediction of Eq. (2.4) that ion-acoustic instabilities are excited in A but not B.

Fluctuations in the uniform simulation (C), as well as the left moving modes ($k < 0$) in both A and B, are consistent with thermal noise. This can be confirmed by calculating the spectral energy as

$$\mathcal{E}(k) = V \int \frac{\hat{\rho}^2}{2\epsilon_0 k^2}\,\mathrm{d}\omega\,, \tag{2.6}$$

where V is the volume of the Fourier transformed region near the right boundary ($V = 0.049$ m^3). We compare this to the theoretical value of the spectral energy for a uniform and stable plasma [69]

$$\mathcal{E}(k)_{\text{theory}} = \frac{T_e^c}{2} \frac{1}{1 + k^2 \lambda_{De}^2}. \tag{2.7}$$

Here $T_e^c = wT_e$ is the temperature of the computational electrons, where w is the number of real electrons represented by a computational electron. Although the effects of ion thermal motion can be included in this prediction, the effects are small [69]. In the uniform plasma (simulation C), both left ($k < 0$) and right ($k > 0$) moving modes agree well with the theoretical predication for thermal fluctuations; see panel (h), as expected. In contrast, panels (b) and (e) show that the energy in the right moving modes is higher than the thermal level in both simulations A and B. Although the enhanced level of fluctuations beyond the predicted thermal level might be considered evidence of instability, there are other reasons this may occur: The estimate from Eq. (2.7) is for a uniform plasma and does not account for gradients in plasma parameters such as density or ion flow, which are both characteristic features of the presheath. Thus, the comparison between the observed and thermal spectra does not provide a conclusive test for instability.

Observation of the instabilities may also be obscured by the fact that the thermal noise level is enhanced in PIC simulations by the particle weight [67, 68], as seen in Eq. (2.7). For example, if the instabilities saturate because of ion trapping, we can estimate the saturation energy density as $\theta_{sat} \approx T_e n_e/36$ [70]. This does not change with the particle weight since the computational particle density is proportional to w^{-1} and the computational particle temperature is proportional to w. When evaluated for the plasma parameters of simulation A we find $\theta_{sat} \approx 1 \times 10^{-3}$ J/m^3. Furthermore, integrating Eq. (2.7) over all k gives an estimate for the PIC thermal

energy density of $\theta_{thermal} \approx T_e^c/(\lambda_{De} \times 1m^2) \approx 10\ J/m^3$, which is 10^4 times higher than the predicted level for saturation. This demonstrates that in such a situation, the instabilities may be difficult to detect by simply comparing observed and thermal spectra.

Profiles of the energy per particle stored in ion-acoustic modes provide further evidence that the ion-acoustic instabilities are excited in simulation A. The energies per particle are calculate as

$$\theta_L = \frac{1}{n_i} \int_{IA,k<0} \mathcal{E}(k)\, \mathrm{d}k\,, \tag{2.8a}$$

$$\theta_R = \frac{1}{n_i} \int_{IA,k>0} \mathcal{E}(k)\, \mathrm{d}k\,, \tag{2.8b}$$

where n_i is the local average ion density. Here $\mathcal{E}$ was calculated as in Eq. (2.6), but using the charge density spectra in adjacent regions of volume V from the center to the sheath edge. The energy in the right moving modes (crosses) increases, especially near the sheath edge, in both simulations A and B; see panels (c) and (f). However, the energy stored in right moving ion-acoustic modes increases more across the presheath in simulation A than B (a percent increase of 122% vs 71%). This is consistent with the presence of instabilities in A and not B. In simulation C the energy stored in both modes is equal and does not vary, as seen in panel (i). In simulations A and B the left moving energies decrease along the direction of ion flow in the presheath except near the sheath edge. The decrease may be because, as one moves toward the sheath, there is less plasma to the right that can emit left moving fluctuations. If this is the case, then it is surprising that the energy in the left moving modes does not reach 0 near the sheath. In fact it increases near the sheath edge in both cases. Reflection of the right moving modes by the sheath or presheath density gradient may explain this.

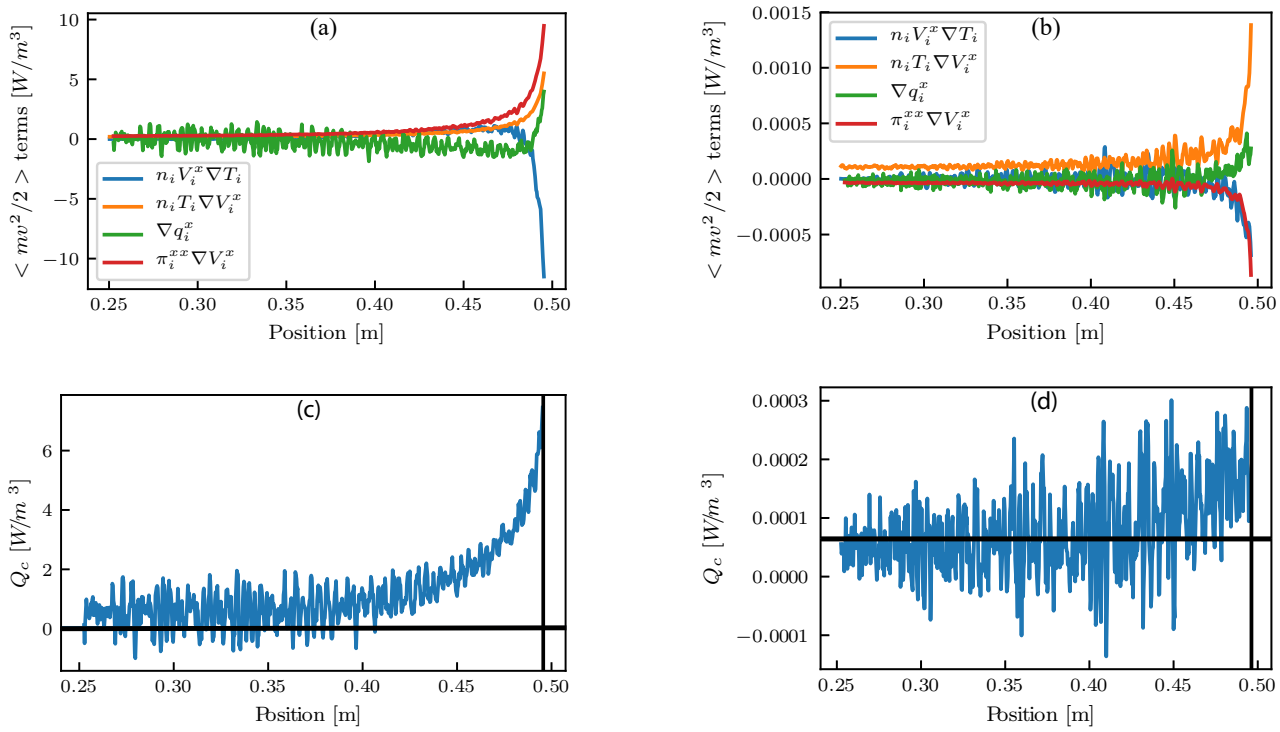

Figure 2.7: Terms on the left side of the ion energy balance from Eq. (2.11) evaluated from the IVDF in: (a) simulation A (T_e = 6 eV), and (b) simulation B (T_e = 0.1 eV). The instability-enhanced collision term (Q_c: blue line) and the source term ($\frac{3}{2}\nu_i^s n_i T_i^s$: horizontal black line) are shown in panel (c) for simulation A and panel (d) for simulation B. The vertical line represents the sheath edge position.

We hypothesize that right moving ion-acoustic modes reflect from the sheath and propagate into the bulk plasma. Consider an ion-acoustic wave excited in the presheath that is moving rightward toward the sheath at the sound speed c_s. Such a wave is carried by electrostatic fluctuations (compression and rarefaction) in both the ions and electrons. When the wave reaches the sheath edge, all of the ions are transferred though the sheath to the boundary, carrying the ion fluctuation energy with them. However, essentially all of the electrons are reflected. The reflected electrons continue to oscillate at the ion-acoustic wave frequency as they propagate back into the bulk plasma. Near the sheath, ions are drifting at nearly the ion-acoustic speed to the right, so there are very few ions resonating with the phase speed of the reflected wave propagating to the left. Thus, the transfer of wave energy from electrons to ions for negative-k modes is minimal near the sheath. However, nearer to the bulk plasma, more ions populate this region of phase space so more fluctuation energy can be transferred from electrons to ions. In the bulk plasma, the ion wave energy is observed in both the electrons and ions. This picture is consistent with left and right moving wave energy profiles shown in Figs. 2.6(c) and (f). It is also consistent with the observation of ion heating in the bulk plasma though instabilities are only predicted near the sheath edge.

To test if the electron fluctuations are reflected from the sheath we calculate the ratio of energy stored in left and right moving electron fluctuations between 0.447 m and 0.496 m (approximating the presheath region):

$$R_{e,i}\% = \frac{\int_{IA,k<0} e^2 \hat{n}_{e,i}^2/(2\epsilon_0 k^2)\,\mathrm{d}k\,\mathrm{d}\omega}{\int_{IA,k>0} e^2 \hat{n}_{e,i}^2/(2\epsilon_0 k^2)\,\mathrm{d}k\,\mathrm{d}\omega}. \tag{2.9}$$

Here, $\hat{n}_{e,i}$ is the electron or ion density spectrum. The values of R_e are shown in Fig. 2.6 (a,d,g), where each is effectively 100%. Such high percentages imply that all the electron fluctuations moving into the sheath are reflected, as we expect. We test

our assumption that ion fluctuations are absorbed at the sheath by computing the same ratio, but using the ion density spectrum in Eq. (2.9); providing R_i. In both presheath simulations the ion fluctuations are partially absorbed since the amount of energy reflected is less than 100% (A: 53.0%, B: 80.0%). Data from both simulations A and B seem consistent with the reflection hypothesis, though we observe less absorption of the ion fluctuations than expected. One reason may be that this definition of reflection coefficient does not account for the continuous thermal excitation. As shown in Fig. 2.6, the left moving modes in the ion fluctuations are consistent with thermal noise near the sheath edge, whereas the right moving modes have a higher level of fluctuations. In contrast, the electron wave power is nearly identical in both the left and right moving modes. In the uniform simulation we observed that both ion and electron fluctuations are fully reflected. This is the expected behavior since all particles reflect from the walls in simulation C.

In summary, the observations presented in Fig. 2.6 are consistent with the hypothesis that instabilities are present when the electron temperature exceeds the predicted threshold for ion-acoustic instability excitation in the presheath, and that some fraction of ion-acoustic fluctuations that impinge on the sheath are reflected back into the plasma, most likely by the electrons. Other works also suggest that ion-acoustic waves reflect from sheaths [71, 72, 73, 74]. Recently, Hood *et al.* [25] measured fluctuations in an ion presheath at conditions where ion-acoustic instabilities were expected to be excited near the sheath edge. The measurements showed evidence of ion-acoustic fluctuations near the sheath edge, but also further into the plasma in the region predicted by linear theory to be stable [25]. Furthermore, when the biased probe on which the sheath formed was removed, and the measurement repeated, no fluctuations were measured to within the diagnostic resolution. This shows that ion-acoustic fluctuations are due to the presence of the sheath, and suggests that they were reflected from the sheath back into the bulk plasma. Our simulations are consistent with this

picture, but the high noise level in PIC simulations makes it difficult to conclusively associate enhanced fluctuations with an instability based on the spectrum alone.

2.3.3 Enhanced electron-ion energy exchange rate

As mentioned earlier, ion heating in simulations with electron temperatures above 0.7 eV seem to be attributable to an increased electron-ion energy exchange rate caused by ion-acoustic instabilities. To test whether this is the case, we evaluate terms in the ion energy evolution equation and find that the term representing instability-enhanced electron-ion scattering is significant in a simulation with T_e^s above the instability threshold (simulation A from Sec. 2.3.2). Furthermore, in a simulation with an electron temperature below the threshold (simulation B from Sec. 2.3.2) the instability-enhanced term is near zero implying that there is no instability-enhanced heating.

The ion temperature equation is obtained from the second velocity moment of the ion kinetic equation, which in one spatial dimension (x) is

$$\partial_t f_i + v_x \partial_x f_i + \frac{e}{m_i} E \partial_{v_x} f_i = C_c + C_n + R^s. \tag{2.10}$$

Here, C_c and C_n are the Coulomb and neutral collision operators and $R^s = \nu_i^s f_i^s$ represents the sourcing of ions at a fixed rate ν_i^s from the distribution f_i^s, a stationary Maxwellian with temperature $T_i^s = 0.026$ eV. Each term on the right side of Eq. (2.10) represents a potential mechanism for heating. The source term (representing ionization collisions) can broaden the IVDF in the presheath by introducing new particles at velocities much less than the average ion velocity. The C_n term represents other ion-neutral collisions, like charge exchange, which can lead to ion heating when a fast ion is effectively slowed down. However, at a pressure of 0.01 mTorr this term is negligible since the ion-neutral mean free path is approximately

100 times longer than the simulation length. Equally as rare are Coulomb collisions between electrons and ions, represented by C_c, since the electron-ion mean free path is also much larger (thousands of meters) than the simulation length. However, if ion-acoustic instabilities are present, they can significantly increase the collision rate between electrons and ions [11]. The increased collision rate would allow for more energy exchange between electrons and ions, heating the ions.

To determine the electron-ion energy exchange rate we calculate the $\frac{m_i}{2}v^2$ moment of Eq. (2.10), which can be cast in terms of the ion temperature. In one spatial dimension and three velocity dimensions the ion temperature equation takes the form:

$$\frac{3}{2}n_i V_i^x \frac{\mathrm{d}T_i^x}{\mathrm{d}x} + n_i T_i^x \frac{\mathrm{d}V_i^x}{\mathrm{d}x} + \frac{\mathrm{d}q_i^x}{\mathrm{d}x} + \pi_i^{xx}\frac{\mathrm{d}V_i^x}{\mathrm{d}x} = Q_c + \frac{3}{2}\nu_i^s n_i T_i^s. \tag{2.11}$$

Here, n_i is the average ion density,

$$q_i^x = \frac{m_i}{2}\int (v_x - V_i^x)|\mathbf{v} - \mathbf{V}_i|^2 f_i \,\mathrm{d}^3 v \tag{2.12}$$

is the x-component of the heat flux,

$$\pi_i^{xx} = m_i \int \left((v_x - V_i^x)^2 - \frac{1}{3}|\mathbf{v} - \mathbf{V}_i|^2\right) f_i \,\mathrm{d}^3 v \tag{2.13}$$

is the xx-component of the stress tensor, and

$$Q_c = \frac{m_i}{2}\int |\mathbf{v} - \mathbf{V}_i|^2 C_c \,\mathrm{d}^3 v \tag{2.14}$$

is the energy moment of the Coulomb collision operator. Since C_n is negligible at low pressure its moment is not included here. The second term on the right hand side represents the energy introduced by the ion source.

The contribution of the electron-ion energy relaxation rate to the ion temperature

equation is determined by evaluating each of the terms on the left side of Eq. (2.11) using the simulated IVDFs, and subtracting from this $\frac{3}{2}\nu_i^s n_i T_i^s$ to obtain Q_c; see Fig. 2.7. The individual terms from simulation B have nearly equal magnitude up until the sheath edge where the flow gradient terms dominate. In simulation A we see similar behavior near the center, but the term related to the stress tensor reverses sign and contributes significantly near the sheath edge. Summing the term on the left hand side of Eq. (2.11) and subtracting the source term results in the residual Q_c which represents the energy exchange rate between electrons and ions. In simulation B the energy exchange rate is effectively a flat profile across the entire domain and has a comparable magnitude to the source term (horizontal line). This is what is expected in a simulation where ion heating results only from the sourcing of particles throughout the presheath. However, the picture changes dramatically in simulation A where the residual term significantly exceeds the source term throughout the presheath, but most notably near the sheath edge. This supports the idea that the heating observed in simulation A is the result of instability-enhanced energy exchange between electrons and ions, since the residual is only significant in simulation A.

Although the instability-enhanced energy exchange rate decreases significantly further from the sheath edge, it is still far larger than the source term ($\frac{3}{2}\nu_i^s n_i T_i^s \approx 2 \times 10^{-3} \frac{\mathrm{W}}{\mathrm{m}^3}$) near the center. This indicates that the heating we observed near the center of simulation A is also caused by the instabilities and further supports the reflection mechanism discussed in the Sec. 2.3.2.

2.4 Higher Pressure

Increasing the neutral pressure has two major consequences: increasing the temperature ratio threshold necessary for exciting the instabilities and increasing the heating that results from ion-neutral collisions in the presheath. Figure 2.8 shows an estimate for the threshold temperature ratio as a function of pressure illustrat-

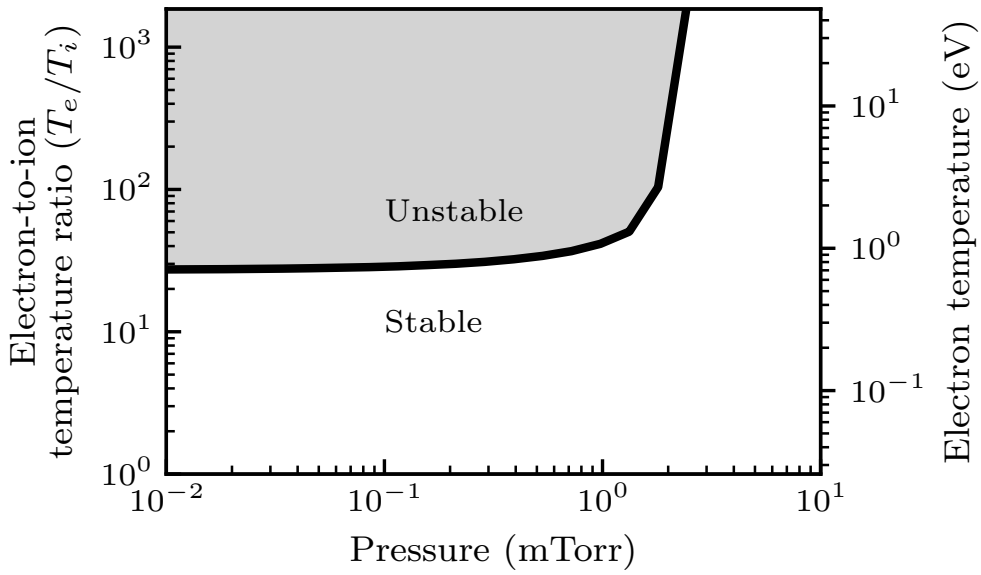

Figure 2.8: The theoretical temperature ratio threshold as a function of pressure calculated using Eq. (2.15).

ing the former point. To study the ion heating due to ion-neutral collisions, with and without the instabilities present, we included simulations at pressures of 0.01 mTorr, 1 mTorr and 10 mTorr with individual simulations taking the same electron temperature values as in Table 2.1. We find that the heating from ion-neutral collisions is isotropic, which distinguishes it from instability-enhanced heating, which is anisotropic (in 1D-3V simulations).

The effects of ion-neutral collisions can be modeled using the Bhatnagar–Gross–Krook [75] (BGK) collision operator. It uses a velocity-independent collision frequency which can be estimated from the Phelps database cross sections of He^+ and He (σ_{i-n}) [62, 63]. Ultimately the BGK model predicts a modification to the growth rate of the form

$$\gamma_{\mathrm{BGK}} = \gamma - \nu_{i-n}/2, \tag{2.15}$$

where γ is the growth rate from Eq. (2.4) and ν_{i-n} is the ion neutral collision frequency estimated as $\nu_{i-n} \approx \sigma_{i-n} c_s n_{He}$. In Fig. 2.8 we see that the collisionless prediction

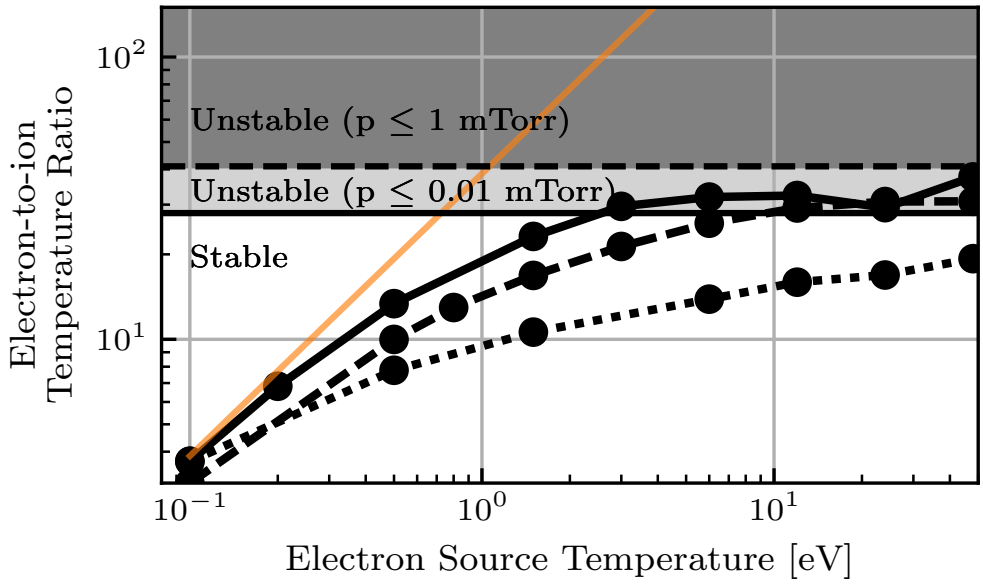

Figure 2.9: Electron-to-ion temperature ratio at the sheath edge vs. T_e^s for pressures of 0.01 mTorr (solid), 1 mTorr (dashed), and 10 mTorr (dotted). The source temperature ratio is shown in solid orange and the solid horizontal line represents the collisionless (0.01 mTorr) prediction for the threshold $(T_e/T_i)^{\text{th}} = 28$ and the dashed line represents the threshold at 1 mTorr $(T_e/T_i)^{\text{th}} = 41$.

of $(T_e/T_i)^{\text{th}} = 28$ is returned at low pressures and at 1 mTorr the temperature ratio threshold is about $(T_e/T_i)^{\text{th}} = 41$, which is a relatively minor change corresponding to an electron temperature threshold of about 1.1 eV. Finally, above approximately 3 mTorr the threshold temperature ratio becomes so large (roughly 1000) that no ion-acoustic instabilities are expected over the entire range of simulated parameters.

Figure 2.9 shows the sheath edge temperature ratio for 3 different pressures. The main observation is that higher neutral pressure lowers the observed electron-to-ion temperature ratio for all source electron temperatures considered. Although the predicted instability threshold is only slightly higher at 1 mTorr than at 0.01 mTorr, 1 mTorr is apparently a high enough pressure to cause some ion heating due to interaction with neutrals. As a consequence, the observed temperature ratio does not reach the predicted threshold value over the range of simulated values. At a pressure of 10 mTorr, heating due to ion-neutral collisions is even more significant. This is

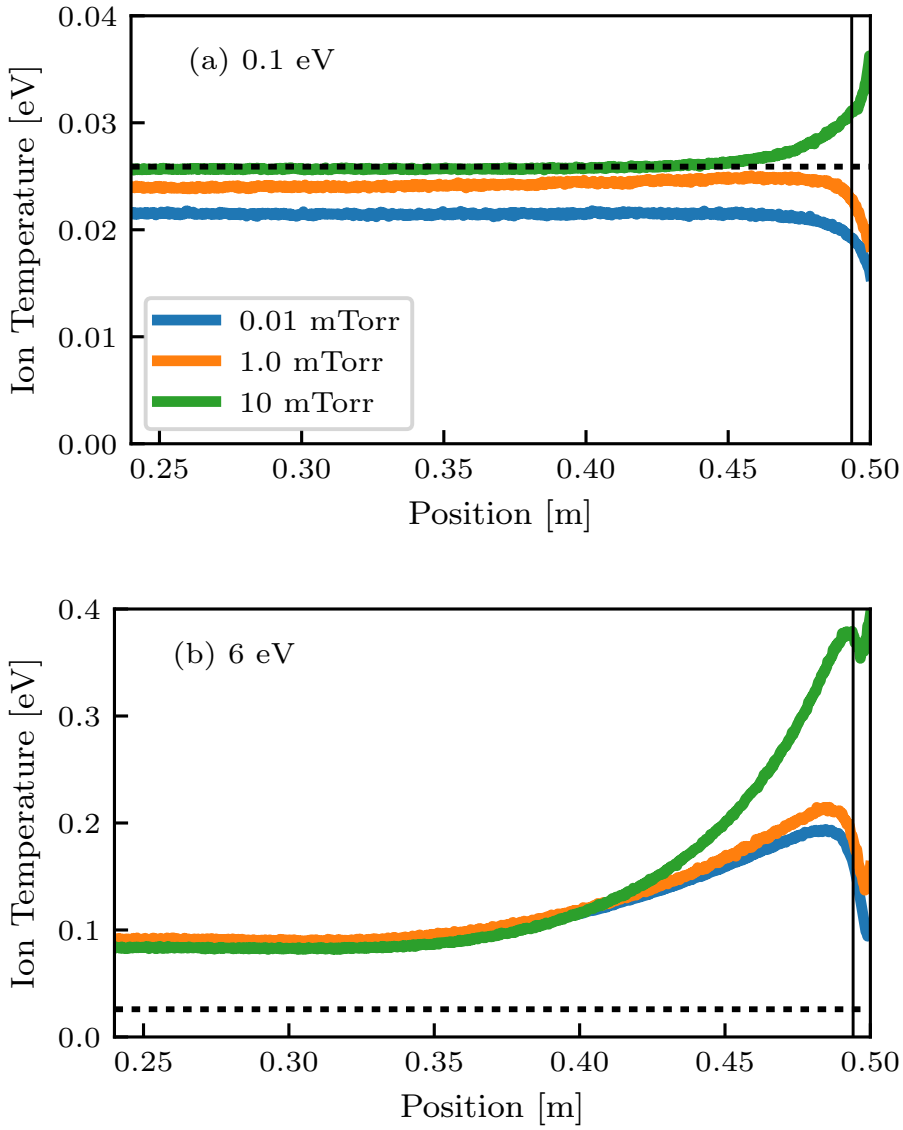

Figure 2.10: Ion temperature profiles for different pressures at electron temperatures of (a) 0.1 eV and (b) 6 eV representing simulations where ion-acoustic instabilities are not present and present only at low enough pressures, respectively. The dashed horizontal line represents the ion source temperature (room temperature).

consistent with the expectation that no ion-acoustic instabilities should be present in the 10 mTorr simulation.

Simulations at low electron source temperatures ($T_e^s = 0.1$ eV) show that ion-neutral collisions result in minor ion heating throughout the presheath, when the pressure is large enough. Specifically, ion temperature profiles from simulations with neutral pressures of 0.01, 1, and 10 mTorr are plotted in Fig. 2.10 (a). For all pressures, the temperature profile is flat through most of the domain. At 0.01 mTorr and 1 mTorr a slight decrease of the ion temperature is observed near the sheath, whereas a slight increase is observed at 10 mTorr. In the simulations with electron temperatures of 6 eV we expect the effects of the ion-acoustic instabilities to be present at low pressure (0.01 mTorr and 1 mTorr), and the effects of ion-neutral collisions to become important at higher pressure (1 mTorr and 10 mTorr). In each of the simulations shown in Fig. 2.10 (b), the temperature in the bulk is approximately the same, and heating is observed near the sheath. The heating is largest at the highest neutral pressure. It is unexpected that the ion heating near the center of the domain persists at higher pressures where the instabilities should be damped.

It is important to point out that the heating from ion-neutral collisions increases with electron temperature as well as neutral pressure. This is seen in Fig. 2.10 where the ion temperature is very close to the source temperature in (a), but much higher in (b). The reason for this is that the sound speed is approximately $\sqrt{60}$ times higher in (b) than (a) since the electron temperature increases by a factor of 60. Plasmas with a higher sound speed experience more ion-neutral heating since the IVDF spans a wider range of velocities ($0 \rightarrow c_s \propto \sqrt{T_e}$) while traversing the presheath. Ion-neutral collisions drag the IVDF out over these lower velocities, resulting in a wider IVDF in plasmas with higher electron temperatures. This makes it difficult to differentiate between instability-enhanced heating and heating from ion-neutral collisions since they increase simultaneously.

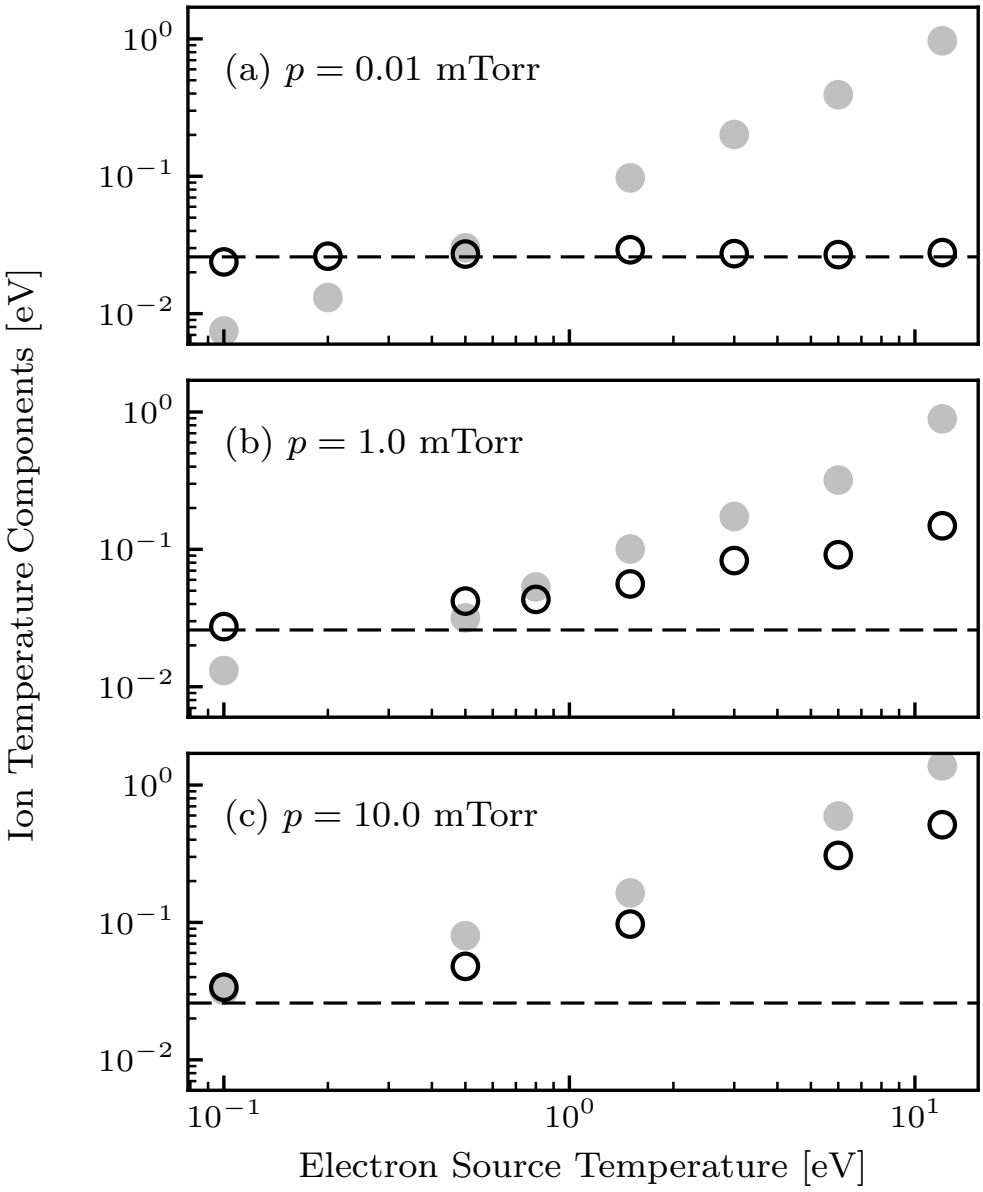

Figure 2.11: Parallel (solid markers) and perpendicular (open markers) ion temperatures at the sheath edge for different electron temperatures at pressures of 0.01 mTorr, 1 mTorr, and 10 mTorr. At higher pressures fewer simulations were run due to increased computation time.

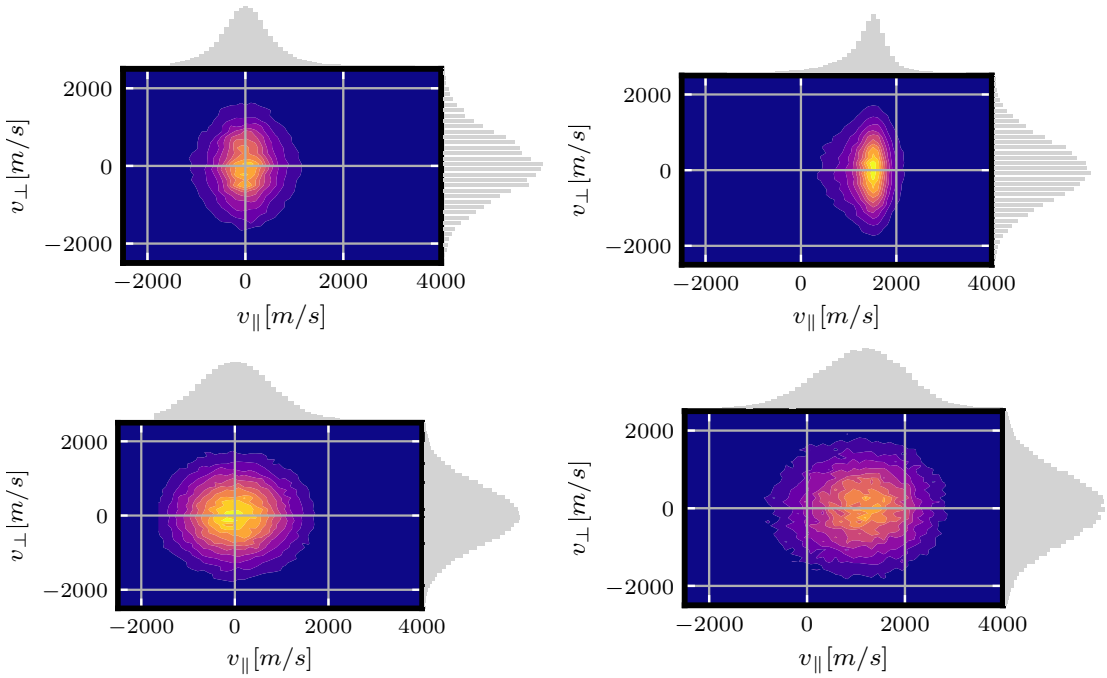

Figure 2.12: IVDFs in the $v_\perp$ vs $v_\parallel$ (v_y vs v_x) plane. The source electron temperature in each simulation was 0.1 eV, which is low enough that no instabilities are expected. Each row shows the IVDF at two different locations from left to right: 0.25 m, 0.49 m. The top row represents a collisionless system with $p_n = 0.01$ mTorr and the bottom row a collisional system with $p_n = 10$ mTorr

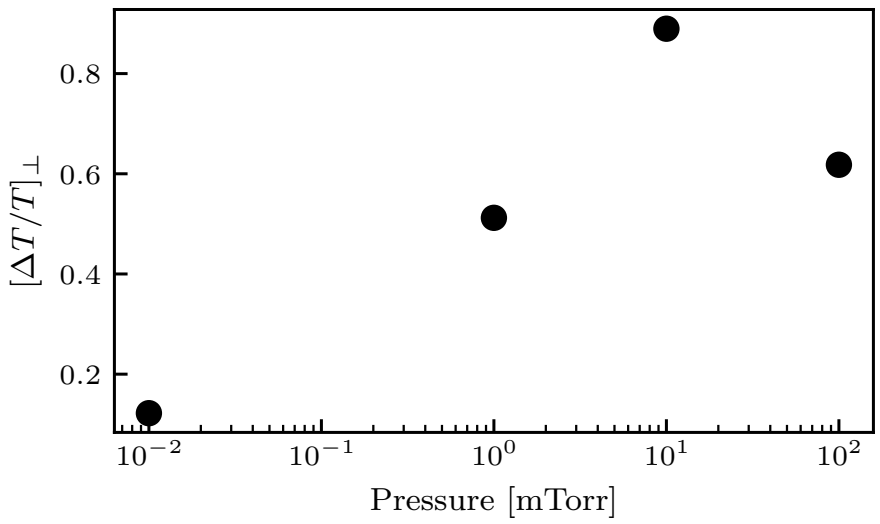

Figure 2.13: Change in perpendicular ion temperatures across the presheath plotted against pressure for an electron temperature of 0.5 eV.

Furthermore, the two mechanisms are not separated by a pressure regime where neither is significant. Instead, when the electron temperature is sufficient for instabilities, the dominant heating mechanism immediately transitions from instability-enhanced to collisional with increasing pressure. This is demonstrated by calculating an estimate of the neutral pressure at which the instability-enhanced energy exchange rate (Q_c) becomes equivalent to the ion-neutral energy exchange rate ($Q_n = \frac{m_i}{2}\int |\mathbf{v}-\mathbf{V}_i|^2 C_n \,\mathrm{d}^3v$). We can estimate Q_c from Fig. 2.7 (c) (which assumes $T_e^s = 6$ eV) and so take $Q_c \approx 1$ W/m^3. Here, Q_n was estimated assuming that the ion-neutral collision operator has the same form as the ion source term, but with a different collision frequency and distribution ($C_n = \nu_{i-n} n_i e^{-(\mathbf{v}-\mathbf{V}_i)^2/v_{Ti}^2}/(\pi^{3/2} v_{Ti}^3)$). This distribution represents the steady-state that the IVDF should relax to in the presence of ion-neutral collisions. In this model, the ion-neutral energy exchange rate is

$$Q_n \ [\mathrm{W/m^3}] \approx \frac{3}{2}\nu_{i-n} n_i T_i \approx \frac{3}{2}\sigma_{i-n} c_s n_{He} n_i T_i, \tag{2.16}$$

where the ion-neutral collision frequency was approximated as $\nu_{i-n} \approx \sigma_{i-n} c_s n_{He}$. The

neutral density can be estimated for a given temperature (here room temperature) and neutral pressure p (measured in mTorr). The estimate for the ion-neutral energy exchange rate is

$$Q_n \text{ [W/m}^3\text{]} \approx 0.3p \text{ [mTorr]}, \tag{2.17}$$

where the electron temperature was taken to be 6 eV and the ion-neutral cross section was estimated as $\sigma_{i-n} \approx 2 \times 10^{-19}\text{m}^2$ from the Phelps database [62, 63]. Equating this to the instability enhanced energy exchange rate results in an estimated transition pressure around 3 mTorr. This implies that at pressures well below this value the instability-enhanced heating is most important, but at intermediate pressures ($\approx$ 1 mTorr) both mechanisms will contribute to ion heating. This estimate appears to be consistent with the observations, and is further corroborated by considering the ion temperature anisotropy.

Specifically, elastic ion-neutral collisions lead to a much more isotropic IVDF than the instability-enhanced heating and the transition from anisotropic to isotropic agrees well with the estimated transition of 3 mTorr. This is depicted in Fig. 2.11, where the perpendicular (open markers) and parallel (solid markers) ion temperature at the sheath edge is plotted as a function of electron temperature for several pressures. Clearly ion-neutral collisions transfer some of the parallel energy the ions gain in the presheath into the perpendicular direction. The simulations also indicate that this transfer in energy is most significant at the highest neutral pressure (10 mTorr), where the heating is nearly isotropic. It is nonexistent at the lowest pressure (0.01 mTorr), and has an intermediate value at 1 mTorr. This seems consistent with the predicted transition from ion-acoustic instability to ion-neutral collisional heating occurring near 1 mTorr neutral pressure.

At electron temperatures where we don't expect ion-acoustic instabilities we find that our observations agree well with previous PIC simulations [59]. In the simulations of Meige *et al.*, the electron density was modeled using the Boltzmann relation instead

of the PIC method and so excluded the excitation of ion acoustic instabilities which require inverse Landau damping to occur [10]. Specifically, we compare their results to our simulations with electron temperatures of 0.1 eV.

Meige *et al.* report a slightly anisotropic IVDF at low pressure (0.1 mTorr) where the ion temperature varies little across the presheath. This is consistent with our simulations, demonstrated in the top row of Fig. 2.12, where the 2D IVDF at 0.01 mTorr has a perpendicular temperature that is nearly twice as large as the parallel temperature. The temperatures in the center ("c") and sheath edge ("se") positions are also nearly equal ($T_c^{\parallel} = 0.014$ eV, $T_{se}^{\parallel} = 0.013$ eV, $T_c^{\perp} = 0.026$ eV, $T_{se}^{\perp} = 0.026$ eV). The lower ion temperature in the parallel direction is associated with ion energy loss to the walls in this dimension. However, at a higher pressures (e.g. 10 mTorr) Meige *et al.* report significant broadening of the parallel IVDF, leading to a more isotropic distribution. Again, we see the same behavior as demonstrated in the bottom row of Fig. 2.12, where the IVDF in the $v_{\perp}$ vs $v_{\parallel}$ plane is nearly circular, with slightly higher temperatures near the sheath edge ($T_c^{\parallel} = 0.024$ eV, $T_{se}^{\parallel} = 0.032$ eV, $T_c^{\perp} = 0.026$ eV, $T_{se}^{\perp} = 0.032$ eV).

In addition to detailing the broadening of the IVDF in the presheath, Meige *et al.* discovered that the ions heat in the perpendicular direction as they transit the presheath and that this effect has a non trivial dependence on the pressure. Specifically, the perpendicular heating due to ion-neutral scattering increases until about 10 mTorr and then decreases at higher pressure. Fig. 2.13 shows the change in perpendicular temperature of the ions across the presheath ($[\Delta T/T]_{\perp} = \big(T_i^{\perp}(\text{se}) - T_i^{\perp}(\text{c})\big)/T_i^{\perp}(\text{c})$). Our simulations show similar behavior to those of Meige *et al.*, though with a slightly higher perpendicular heating at all pressures. Specifically, at 10 mTorr our simulations predict a percent increase of 0.9 while Meige *et al.* predict 0.75. This further supports the fact that our simulations agree well with previous simulations when we chose the electron temperature to be low enough that

the ion-acoustic instabilities are not excited.

2.5 Conclusions

We observe significant ion heating in the presheaths in 1D PIC-DSMC simulations when the electron-to-ion temperature ratio is high enough to excite ion-acoustic instabilities near the sheath edge. We observe enhanced ion-acoustic fluctuation levels alongside ion heating when the instabilities are expected. Further analysis of our simulations support the hypothesis that excited waves greatly increase the rate of electron-ion energy equilibration such that the electron-to-ion temperature ratio at the sheath edge is near the threshold value at which instability onsets. Wave reflection is observed and is a plausible mechanism allowing for the heating to occur away from the sheath. The heating we observe exceeds the heating expected from inelastic collisions that occur in the presheath at low pressure. The amount of heating observed increases with the source electron temperature. At sufficiently high neutral gas pressure, the instability-enhanced heating mechanism is replaced by collisional heating (here at pressures above 1 mTorr). However, ion heating is still observed far from the sheath edge, which is unexpected at high pressures. Currently available experimental data are consistent with what we observe in our simulations, but measurements of the ion temperature over a range of electron temperatures will be needed to provide a definitive test. In addition, the instability-enhanced heating observed is limited to the parallel direction of our 1D-3V simulations; however this may be an artifact of the 1D simulations since the electric field is confined to the one spatial dimension. 2D or 3D simulations will be necessary to confirm if this is the case and what effect it has on the heating. The results presented in this work provide another example of how electrostatic instabilities driven by ion flow influence transport in the presheath [30].

CHAPTER III

Collisional Bohm Criterion and Sheath Properties

3.1 Introduction

Understanding how sheaths work is important because they mediate the interaction of plasmas with the materials that surround them. They also set boundary conditions that determine bulk properties of a plasma. Because of their importance, sheaths have been studied for a long time [21]. This has led to models for key aspects of sheaths, including the density [28, 76, 77] and speed of ions at the sheath edge [15, 16, 17, 18, 78], the sheath width [28, 79, 80], and the electrostatic potential change across the sheath and presheath [80]. Although models have been developed to treat a wide range of conditions, the experimental validation necessary to distinguish which are correct has largely been confined to low neutral gas pressures (less than a few mTorr). It is important to extend this to higher pressures where plasmas operate in many applications, but diagnostics become more challenging at these conditions. Here, we take an intermediate step toward validation by testing models using particle-in-cell simulations. These simulations provide meaningful tests because they solve a more complete model than the approaches that have been applied to analyze sheath properties. The simulations are not limited by diagnostic access and essentially any property can be directly computed. Simulations were performed over pressures ranging from $10^{-2} - 10^{4}$ mTorr. Results show that ion-neutral collisions

substantially alter sheath properties at pressures exceeding a few mTorr. The data is used to quantify the following dimensionless sheath properties: edge-to-center density ratio ($h_l = n_{\mathrm{se}}/n_{\mathrm{c}}$), collisional Bohm criterion ($a_l \equiv V_{i,\mathrm{se}}/c_{\mathrm{s}}$), sheath width ($w_{\mathrm{s}}/\lambda_{\mathrm{De}}$), electric field at the sheath edge ($E_{\mathrm{se}}/(T_e/e\lambda_{\mathrm{De}})$), sheath potential drop ($e\Delta\phi_{\mathrm{s}}/T_e$) and presheath potential drop ($e\Delta\phi_{\mathrm{ps}}/T_e$).

Previous models have predicted that ion-neutral collisions act to decrease the speed of ions at the sheath edge [15, 16, 17, 18, 78], decrease the edge-to-center density ratio [28, 76, 77], and increase the sheath width [28, 79, 80] and potential drop across the sheath and presheath [80]. A variety of models have been proposed based on either fluid or kinetic approaches. Although they tend to give quantitatively different predictions, they also tend to agree on the general trends as neutral gas pressure increases. Some of the models differ particularly in how they treat the ionization source, with the most popular choice being a source rate proportional to the electron density [81]. To focus on the influence of the ion-neutral collision rate, our simulations used a constant and uniform volumetric source and included only elastic ion-neutral collisions.

To compare with the simulations, we develop a model based on fluid conservation equations for ions, the Boltzmann density distribution for electrons, and Poisson's equation to connect the fluid quantities and electric field. The model is solved numerically for the plasma density, ion velocity, and electric field profiles which allow us to calculate the aforementioned plasma properties at the sheath edge. In addition, simple analytic formulae for the sheath properties are developed from approximations of the fluid model and input from the simulations. The fluid model is inspired by, and in some respects the same as, previous work [77, 82]. Some further development was required to incorporate the constant ionization source term, especially in obtaining analytic approximations of the sheath properties. Another aspect of development was to solve for all these properties from a single self-consistent model. This leads to some

distinctions from previous work.

For example, previous models have effectively combined the collisional Bohm criterion (a_l) and edge-to-center density ratio (h_l) into a single factor (h_l^*). This is a feature of the previous models because they have either (1) used the sound speed as a boundary condition in deriving h_l [77], which neglects the collisional Bohm criterion (a_l), or (2) defined h_l as the ratio of the ion flux at the sheath edge compared to $n_c c_{s,c}$ [76]. Here, $c_{s,c}$ is the sound speed at the center of the domain. The latter approach was motivated by global models that require the flux to the boundary as an input parameter [83]. In either case, it is useful to define h_l as the edge-to-center density ratio and modify the analysis to account for distinct h_l and a_l factors. For instance, the distinction is essential to correctly compute the plasma potential.

Finally, we note that a variety of definitions for the sheath edge have been put forth, and that sheath properties can depend sensitively on the definition. The original definition suggested by Langmuir is that the sheath edge separates a quasineutral plasma from a non-neutral sheath [1]. Other definitions have been used, such as taking the location that ions reach the sound speed [77], or the location where a critical value of the electric field is obtained [15]. We emphasize that it is important to adopt Langmuir's original definition, as this is the closest location to the boundary where the electron and ion densities are equal, which allows one to compute the flux of plasma reaching the boundary based on knowledge of the bulk plasma properties and a model for the h_l and a_l factors. We find that Langmuir's definition is consistent with a critical value of the electric field, though one that is much smaller than previously proposed. Other definitions, such as the point where ions reach the sound speed, become increasingly problematic at high pressure as ions can make it all the way to the boundary at a sub-sonic speed, even though there remains a highly non-neutral sheath region near the boundary surface.

Comparison of the simulations, numerical solution of the fluid model, and analytic

expressions for the sheath properties are found to generally agree well. Assumptions made in the fluid model, particularly the Boltzmann density relation for electrons, begin to break down at the highest pressure case that was simulated (10^4 mTorr). But overall the result is a comprehensive model for sheath properties over a broad range of neutral gas pressures, that has at least been tested by a high-fidelity computational model. The work may inspire future experimental tests to complete the validation needed for adoption of the model.

3.2 Model and simulations

3.2.1 PIC simulation setup

PIC simulations of electron-helium plasmas were carried out using the electrostatic simulation code Aleph [43]. Each simulation had one spatial dimension of length $L = 1.0$ cm and 3 velocity dimensions and included electrons, singly charged helium ions, and neutral helium particles. Both electrons and ions were sourced uniformly in space and time from stationary Maxwellian distributions with electron temperature $T_e^s = 1$ eV and ion temperature $T_i^s = 0.026$ eV respectively. The source rate was $S = 1.62 \times 10^{22}$ particles/m^{3}s in all but the highest pressure simulation where it was reduced to $S = 4.05 \times 10^{21}$ particles/m^{3}s. For a given pressure the neutral density was computed as $n_n[\text{m}^{-3}] = 3.250 \times 10^{19} p_n[\text{mTorr}]$. The constant source rate makes it simple to compute the ion flux throughout the domain ($\Gamma_i = Sx$, where S is the source rate and x is the distance measured from the center of the discharge), and in some ways simplifies the fluid model (see appendix B.1). It has been studied using PIC before [84], and also represents a common type of low temperature, low pressure plasma experiment where ionization is generated by a dilute population of high-energy injected electrons; such as the filament discharges with a multi-dipole chamber that are common in sheath studies [85] and in certain hollow cathode devices [86].

The mesh was uniform in each simulation and was composed of 500 cells for simulations with neutral pressures at or below 10^2 mTorr and 5,000 cells for higher pressures. The mesh was refined to resolve the ion-neutral mean free path ($\lambda_{in,c} \propto p_n^{-1}$) by a factor of 2 at the highest pressures. In addition, the ratio of cell size to the Debye length at the center of each simulation was $dx/\lambda_{\mathrm{De}} \approx 0.5$, except in the simulation at 10^3 mTorr where it was set to 0.1.

The time step was chosen to resolve the electron plasma frequency and a CFL-like condition, so that an electron with velocity lower than $0.5\sqrt{eT_e/m_e}$ does not cross an entire spatial cell in one time step [36]. However, since the mesh was refined at higher pressures the time step was decreased from 4×10^{-11} s for simulations with neutral pressures below 10^3 mTorr, to 1×10^{-11} s for those at or above 10^3 mTorr. The time to steady state ranged from 4×10^{-5} s to 4×10^{-4} s as the pressure was increased from 10^{-2} mTorr to 10^4 mTorr.

The computational weight of the electrons and ions was the same, though this value was changed between simulations since the density increased at higher pressure (see table 3.1). This required significantly more particles in the higher pressure simulations. The weight was chosen so that the average number of particles per cell for each species was approximately 30 near the center in each simulation. The number of particles per cell near the wall ranged from about 15 at pressures below 10^3 mTorr to as small as 1 at 10^4 mTorr.

The direct simulation Monte Carlo (DSMC) method was used to simulate ion-neutral and electron-neutral collisions [40], while no method was used to include binary Coulomb collisions. Only two interactions were included: elastic ion-neutral collisions and elastic electron-neutral collisions. For both interactions the scattering angles are distributed isotropically and momentum and energy are conserved. The method for calculating post-collision velocities is described in [40] on page 131.

Cross sections for both interactions were taken from the Phelps database provided

by LXCat [62, 63, 64, 65]. Furthermore, only the total cross section was available for helium ion-neutral collisions, though it was split into isotropic and back-scatter components. We chose to use only the isotropic component of the total cross section for ion-neutral collisions as it is advantageous for developing a simple fluid model. This is due to the fact that the isotropic cross section scales inversely with the relative velocity (u^{-1}). Ultimately, this means that using the same cross section in our fluid model will reduce it to a constant mean free path model.

Throughout this chapter all reported temperatures refer to the 1D temperature. The 1D temperature is computed from the reduced velocity distribution functions (e.g., $f_{s,x}(v_x) = \int f_s(\boldsymbol{v})\mathrm{d}v_y\mathrm{d}v_z$), using

$$T_s = \frac{m_s}{n_s}\int (v_x - V_s)^2 f_{s,x}(v_x)\mathrm{d}v_x, \tag{3.1}$$

where $V_s = \frac{1}{n_s}\int v_x f_{s,x}(v_x)\mathrm{d}v_x$, x represents the one spatial dimension of our simulations, m_s is the mass of a particle of species s, and n_s is the density.

In each PIC simulation the sheath edge is defined as the location where the charge density first exceeds $P_\rho = 0.019$ of the average electron density (i.e., $n_i - n_e = P_\rho n_e$). This value was chosen because it represents the location in the lowest pressure simulation where $V_i = c_{s,\mathrm{c}} = \sqrt{eT_{e,\mathrm{c}}/m_i}$. Here $T_{e,\mathrm{c}}$ is the electron temperature at the center. Physically, it corresponds to a small but non-zero charge density that defines the separation between quasineutral plasma and non-neutral sheath. Results are also provided for a range of values $P_\rho = 0.0077 - 0.048$, illustrating the sensitivity of the results to the particular numerical value that is chosen.

3.2.2 Fluid model

Here we develop a fluid model that captures the basic physics of the PIC simulations and can be analyzed to give expressions for the quantities of interest like a_l

p_n	$\lambda_{\mathrm{De,c}}/\lambda_{in,\mathrm{c}}$	$T_{e,\mathrm{c}}$	$T_{e,\mathrm{se}}$	$V_{i,\mathrm{se}}$	n_{se}	n_{c}	$\sigma_s(T_{e,\mathrm{c}})$
10^{-2}	1.53×10^{-6}	0.895	0.701	4.72×10^{3}	1.60×10^{16}	2.92×10^{16}	1.29×10^{-19}
10^{-1}	1.53×10^{-5}	0.903	0.718	4.61×10^{3}	1.64×10^{16}	2.92×10^{16}	1.27×10^{-19}
10^{0}	1.52×10^{-4}	0.909	0.732	4.65×10^{3}	1.62×10^{16}	2.95×10^{16}	1.26×10^{-19}
10^{1}	1.46×10^{-3}	0.868	0.786	4.49×10^{3}	1.67×10^{16}	3.21×10^{16}	1.21×10^{-19}
10^{2}	1.30×10^{-2}	0.945	0.894	4.30×10^{3}	1.74×10^{16}	4.01×10^{16}	1.14×10^{-19}
10^{3}	6.95×10^{-2}	0.859	0.701	2.64×10^{3}	2.90×10^{16}	1.41×10^{17}	1.29×10^{-19}
10^{4}	2.93×10^{-1}	0.326	0.230	4.07×10^{2}	4.74×10^{16}	7.91×10^{17}	2.25×10^{-19}

Table 3.1: PIC simulation parameters: neutral pressure (p_n [mTorr]), ratio of sheath edge Debye length to ion neutral mean-free-path ($\lambda_{\mathrm{De,c}}/\lambda_{in,\mathrm{c}}$), center electron temperature ($T_{e,\mathrm{c}}$ [eV]), sheath edge electron temperature ($T_{e,\mathrm{se}}$ [eV]), sheath edge ion velocity ($V_{i,\mathrm{se}}$ [m/s]), sheath edge density (n_{se} [#/m^3]), center density (n_{c} [#/m^3]), and ion-neutral elastic cross section evaluated at $c_{\mathrm{s,c}}$ (σ_s [m^2]) Here the sheath edge was defined using $P_\rho = 0.019$.

and h_l. Previous authors have used the same model equations [82]. The fluid model includes the continuity equation with a constant source rate (S [particles/(m^{3}s)]), which matches how the plasma is sourced in the PIC simulations:

$$\frac{\mathrm{d}}{\mathrm{d}x}(n_i V_i) = S \tag{3.2}$$

In addition, we include an ion momentum equation that accounts for only the electrostatic and friction force on the ions:

$$m_i n_i V_i \frac{\mathrm{d}V_i}{\mathrm{d}x} = e n_i E - R_{in} - m_i V_i S. \tag{3.3}$$

The friction force can be written

$$\begin{aligned} R_{in} &= m_i n_i V_i \nu_{in} \\ &= m_i n_i V_i (c_{\mathrm{s,c}}/\lambda_{in,\mathrm{c}}), \end{aligned} \tag{3.4}$$

where we have used a constant collision frequency model: $\nu_{in} = n_n \sigma V_i = c_{\mathrm{s,c}}/\lambda_{in,\mathrm{c}}$. This corresponds to choosing a cross section of the form $\sigma = \sigma_s(c_{\mathrm{s,c}}/V_i)$, as in the Phelps database provided by LXCat used in our PIC simulations [62]. This is the same form as used in previous models [78, 82]. Here, σ_s is the cross section evaluated at the sound speed ($c_{\mathrm{s,c}}$). This form of the friction force can be derived by taking the momentum moment of the Boltzmann collision operator and applying the $\sigma = \sigma_s(c_{\mathrm{s,c}}/V_i)$ form of the cross section; see appendix B.2. The ion-neutral collision mean free path is then $\lambda_{in,\mathrm{c}} = 1/(n_n \sigma_s)$.

Finally, we close the system of equations with Poisson's equation

$$\epsilon_0 \frac{\mathrm{d}^2\phi}{\mathrm{d}x^2} = -e(n_i - n_{\mathrm{c}} e^{-e\phi/T_{e,\mathrm{c}}}), \tag{3.5}$$

where we have used the Boltzmann density relation for the electrons and n_c is the center density.

The Boltzmann density relation assumes that the electrons are isothermal. It is known that electron temperature gradients exist in the presheath and sheath mainly due to the non-local kinetic effect of loss of high energy electrons (those above the sheath potential energy) to the wall [29, 87]. Recent work has explored modified fluid models that attempt to account for this effect [87, 88, 89]. The accuracy of the isothermal assumption is assessed in section 3.3 and section 3.4.6 provides a discussion of how this aspect of the model might be improved.

The model equations can be cast in a dimensionless form where the position is measured in electron Debye lengths ($\lambda_{\mathrm{De,c}} = \sqrt{T_{e,\mathrm{c}}\epsilon_0/n_{\mathrm{c}}e^2}$) at the center of the plasma, the electric field is measured in $(T_{e,\mathrm{c}}/e)/\lambda_{\mathrm{De,c}}$, the density is measured in terms of the

center density (n_c), and the velocity is measured in terms of the sound speed:

$$\frac{d}{dx}(n_i V_i) = s, \tag{3.6}$$

$$n_i V_i \frac{dV_i}{dx} = n_i E - n_i V_i(\lambda_{De,c}/\lambda_{in,c}) - V_i s, \quad \text{and} \tag{3.7}$$

$$\frac{d^2\phi}{dx^2} = (e^{\phi} - n_i). \tag{3.8}$$

Furthermore, the dimensionless form of the model is fully described by only two dimensionless quantities: the source strength ($s = S\lambda_{De,c}/(n_c c_{s,c})$) and the collisionality ($\lambda_{De,c}/\lambda_{in,c}$). The latter is proportional to the pressure

$$\lambda_{De,c}/\lambda_{in,c} = (\lambda_{De,c}\sigma_s)p_n/T_n, \tag{3.9}$$

which is the independent variable of our study. For each pressure, we calculate $\lambda_{De,c}/\lambda_{in,c}$ using $T_{e,c}$ and n_c from the corresponding PIC simulation. Then the fluid model is solved numerically for each value of $\lambda_{De,c}/\lambda_{in,c}$. The values of $\lambda_{De,c}/\lambda_{in,c}$ for each pressure are shown in table 3.1 alongside the values of σ_s used to calculate $\lambda_{in,c}$.

Appendix B.1 discusses the details of the numerical solution of equations (3.6-3.8). In addition, the sheath edge was defined using the same criterion as in the PIC simulations, but where $P_\rho^{\text{fluid}} = 0.057$. This value was chosen so that $V_i = c_{s,c}$ in the lowest pressure numerical fluid solution.

3.3 Results

The main results of the PIC simulations are shown in Fig. 3.1 where profiles of the average ion velocity, relative density, charge density fraction, plasma potential, electron temperature, and ion temperature are plotted. The profiles from simulations with $p_n = 10^{-2}$ and 10^{-1} mTorr have been omitted as they generally overlap with the profiles for $p_n = 10^{0}$ mTorr. The sheath edge is highlighted by the circles on

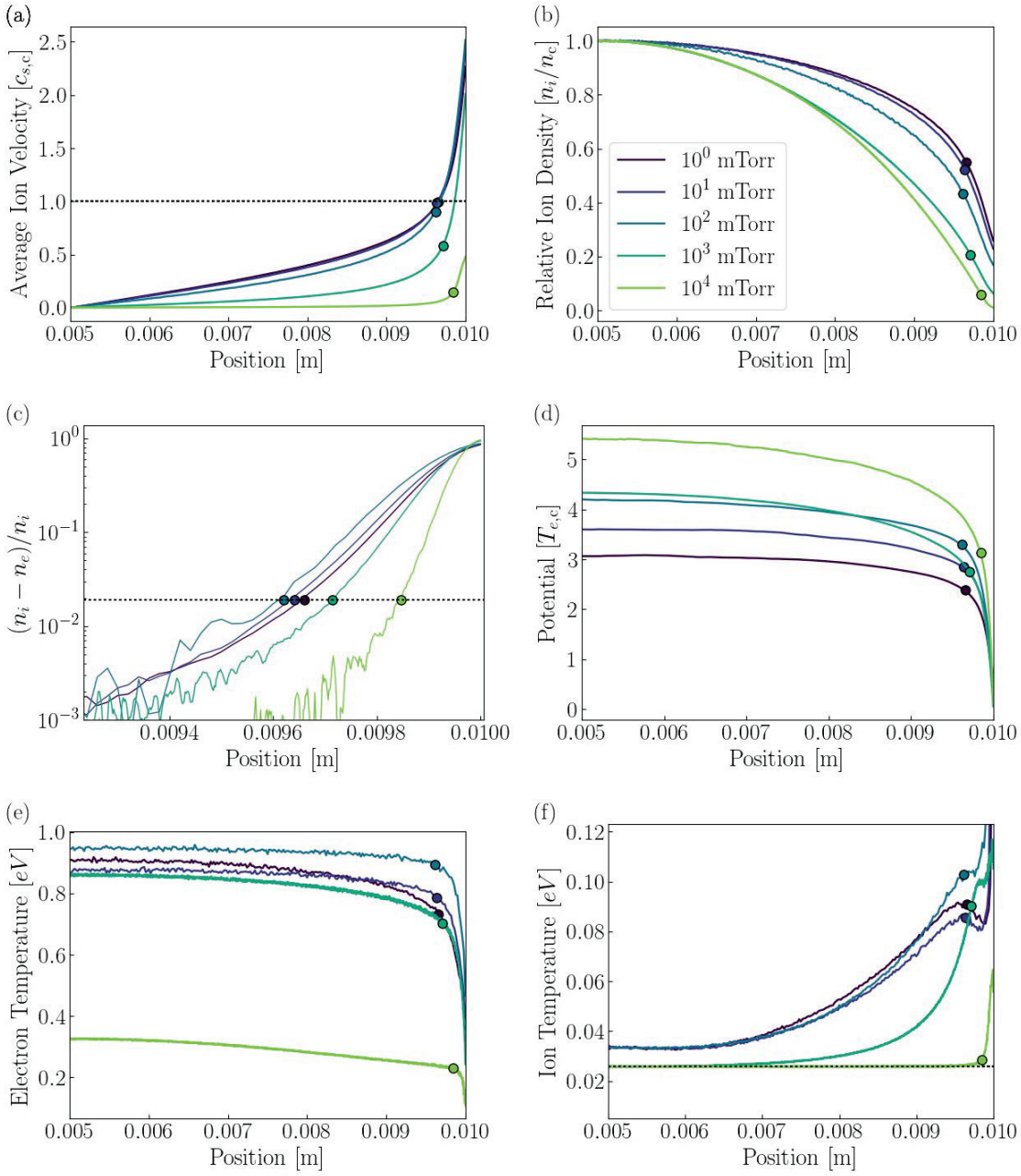

Figure 3.1: Spatial profiles of the (a) ion velocity (V_i), (b) relative ion density (n_i/n_c), (c) fractional charge density ($(n_i - n_e)/n_e$), (d) plasma potential ($\phi/T_{e,c}$), (e) electron temperature (T_e), and (f) ion temperature (T_i). Circles denote the location of the sheath edge. The dashed line in panel (a) represents the sound speed $c_{s,c}$. The dashed line in panel (c) represents the value of P_ρ and so shows the sheath edge positions. The dashed line in panel (f) represents the ion source temperature 0.026 eV.

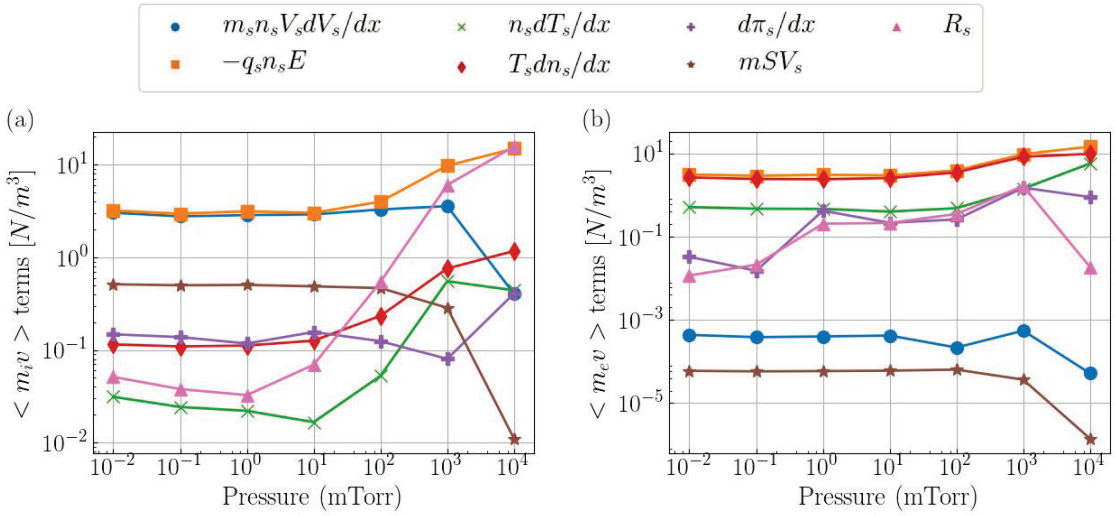

Figure 3.2: Terms from Eq. (3.10) evaluated for the ions (a) and electrons (b) at each pressure: (circles) inertial, (squares) electric field, (crosses) temperature gradient, (diamonds) density gradient, (pluses) stress gradient, (stars) source, and (triangles) friction with neutrals.

each profile and the values of V_i, n_i, and T_e at this location are reported in table 3.1. Clearly, the ion velocities and relative densities are reduced at higher pressures, while the potential increases.

Panel (a) shows that the ion velocity decreases everywhere in the domain as the pressure increases. Most notably, the ion velocity at the sheath edge is reduced below the sound speed when the pressure is above a few mTorr, illustrating that there is a collisional Bohm criterion (i.e. $a_l < 1$). The largest reduction is observed at the highest pressure ($a_l \approx 0.1$ at 10^4 mTorr), where the ion flow speed does not reach the sound speed at any point in the domain. This demonstrates a shortcoming of using $V_i = c_{\mathrm{s,c}}$ to define the sheath edge.

Besides being slowed, the relative ion density (n_i/n_{c}) is reduced with pressure as shown in panel (b). Specifically, the edge-to-center density ratio decreases with increasing pressure. Note that in terms of the absolute number density (measured in $\#/m^3$), both the central density n_{c} and sheath edge density increase with pressure (table 3.1).

The charge density fraction $(n_i - n_e)/n_e$ is a local measure of quasineutrality and is plotted in panel (c). Note that panel (c) shows only a small part of the domain near the right boundary. The sheath can be identified in each simulation as the location where the charge density fraction is significant. In fact, we use the charge density fraction to determine the sheath edge. Specifically, the time averaged charge density fraction is smoothed using a moving average that is 5 cells wide. Then the sheath edge is defined as the point where $P_\rho = (n_i - n_e)/n_e = 0.019$. The sheath edge location depends weakly on P_ρ and the filter parameters.

The local plasma potential profiles are shown in panel (d) and, as in (a) and (b), the profiles increase monotonically with pressure. Along with the general increase of the plasma potential, a rounding of the profile is observed so that the potential drop across the presheath (i.e the quasineutral part of the plasma) and the sheath individually increase with pressure.

Panel (e) shows the electron temperature profiles, which do not change monotonically with the pressure. The most important feature is that each is relatively constant, which is an assumption of our fluid model. However, the steady-state electron temperatures depend on the neutral pressure. This is most notable at 10^4 mTorr, where the electron temperature is approximately 0.3 eV, which is significantly lower than the source temperature of 1 eV.

Panel (f) shows the ion temperature profiles, which are clearly not constant and display heating above the ion source temperature (0.026 eV) near the sheath in all but the highest pressure simulations. Chapter II discussed the heating and its causes at low pressure, while at higher pressure [59] provided PIC simulations describing collisional heating. Our fluid model assumes the ion temperature to be constant. While this is clearly not the case, the fluid model is still a good approximation because the small value of the ion temperature causes the temperature gradient term of the momentum balance equation to remain small in comparison to the other terms in

Eq. (3.3); see Fig. 3.2.

To test this, we can calculate each term of the momentum equation for both ions and electrons and determine which are most significant. The general 1D momentum equation for species s is:

$$m_s n_s V_s \frac{\mathrm{d}V_s}{\mathrm{d}x} = q_s n_s E - T_s \frac{\mathrm{d}n_s}{\mathrm{d}x} - n_s \frac{\mathrm{d}T_s}{\mathrm{d}x} - \frac{\mathrm{d}\pi_s}{\mathrm{d}x} - m_s V_s S - R_s. \tag{3.10}$$

Here, π_s is the xx-component of the stress tensor and $R_s = \sum_{s'} R_{ss'}$ is the friction on species s due to collisions with all other species (s'). Each of these terms, excluding R_s, was evaluated directly from the time averaged velocity distribution functions from the PIC simulations. R_s was calculated from the residual of all other terms in Eq. (3.10). The magnitude of each term at the sheath edge is shown in Fig. 3.2 (a) and (b), for ions and electrons respectively. Furthermore, Fig. 3.2 shows which terms are important in Eq. (3.10) at different pressures. For ions, the friction, electric field, and inertia terms dominate; justifying the reduced fluid model from Eq. (3.3). Even though the source term ($m_n V_i S$) is a second-order term it is included in the model because it makes the model more accurate and is simple to implement.

For electrons, the electric field and pressure terms are the largest for most of the pressure range. This supports the use of the Boltzmann density relation. However, the electron temperature gradient and to some extent the electron stress gradient are non-negligible even at the lowest pressures and become comparable to the largest terms at the highest neutral gas pressure (10^4 mTorr). Recent work has discussed modeling the electron temperature gradient term [29, 87, 88, 89], and some discussion of how this may influence the plasma properties at the sheath edge is provided in section 3.4.6

In addition, we can test how well the constant collision frequency model of the

ion-neutral friction force (Eq. (3.4)) represents the total ion friction force in the PIC simulations (R_i) which is measured from the residual of Eq. (3.10). In general the two may not be equal since (R_i) includes the friction from ion-electron and ion-neutral collisions $R_i = R_{ie} + R_{in}$. However, it is expected that R_{ie} should be negligible in our simulations since the ion-electron momentum transfer mean free path is approximately 10 m, which is many times larger than the domain length. The mean free path was estimated from the Coulomb collision frequency [66]. Furthermore, Coulomb collisions were not explicitly included in the simulations (though there may be a degree of electrostatic interactions via the macroparticle electric fields). Figure 3.3 shows $|R_i|$ (circles) and the evaluation Eq. (3.4) using the PIC values of $V_{i,\mathrm{se}}$ and $n_{i,\mathrm{se}}$ (squares). The two agree well above 10 mTorr indicating that the friction felt by the PIC ions is accurately described by Eq. (3.4). At lower pressures there is significant disagreement which could be the result of (1) ion-acoustic instabilities excited near the sheath edge that can enhance ion-electron collisions and so R_{ie} as described in chapter II or (2) reaching a noise floor of the PIC data. Most likely, the value of R_i is limited by noise at low pressures since the terms of Eq. (3.10), specifically the time averaged value of E, have large statistical fluctuations which set a minimum value for $|R_i|$. This is supported by the fact that the sign of R_i fluctuates between negative (empty circles) and positive (filled circles) values at pressures below 10^2 mTorr. This behavior is not surprising since PIC is known to have high statistical noise.

The value of the friction force in the fluid model is also shown (red crosses) and was calculated from Eq. (3.4) using $V_{i,\mathrm{se}}$ and $n_{i,\mathrm{se}}$ from the numerical solutions of the fluid model, but where n_c and $T_{e,\mathrm{c}}$ were taken from the PIC data, since the fluid model is solved in dimensionless variables. The differences between the fluid model and PIC predictions at the highest pressure stems from differences in the density and velocity at the sheath edge that are discussed in the following sections.

Finally, we note that the model for $R_{in,\mathrm{se}}$ can be evaluated using n_c, $T_{e,\mathrm{c}}$, and

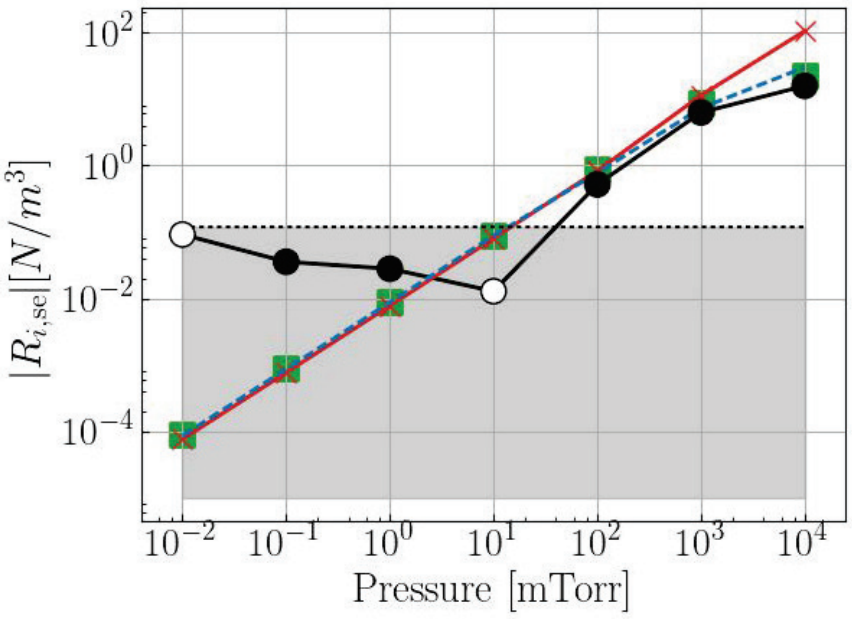

Figure 3.3: Ion fiction force at the sheath edge calculated from PIC data as the residual of terms in Eq. (3.10) (circles). Estimate of the statistical error in $R_{i,\mathrm{se}}$ (grey) based on the standard deviation of the other term in Eq. (3.10). Empty (filled) circles denote negative (positive) values of $R_{i,\mathrm{se}}$. Evaluation of Eq. (3.4) using sheath edge PIC data (squares). Evaluation of Eq. (3.4) using numerical solutions of the fluid model (equations (3.2-3.5)) and n_c and $T_{e,\mathrm{c}}$ from PIC (red crosses). Evaluation of Eq. (3.4) using the reduced expressions of the PIC data (equations (3.14) and (3.13)) (dashed).

$\lambda_{in,\mathrm{c}}(p_n)$ values from the simulations along with models for a_l (Eq. (3.13)) and h_l (Eq. (3.14)) described in the following sections. This results in the dashed line in Fig. 3.3 and the following expression:

$$R_{in,\mathrm{se}} = m_i n_\mathrm{c} h_l a_l (c_{\mathrm{s,c}}^2/\lambda_{in,\mathrm{c}}). \tag{3.11}$$

This expression agrees well with the PIC results, which is expected since both use the same cross section model.

3.4 Discussion

3.4.1 Collisional Bohm criterion

Figure 3.4 shows the simulated ion velocity at the sheath edge (a_l) taken from the profiles in Fig. 3.1 (a). The grey region about this line corresponds to values of a_l measured from the PIC profiles for P_ρ ranging from 0.0077 to 0.048. This illustrates that the collisional Bohm criterion is not very sensitive to the value of P_ρ. The values of a_l are more sensitive at lower pressures than higher pressures.

We compare the PIC simulation results to an existing model of a_l, which was derived using an approximation of equations (3.2-3.5) [78]. The equations were applied to the sheath region, where ionization events are expected to be rare, so $S \approx 0$. The authors then calculated the Sagdeev potential [90] and evaluated its second derivative at the sheath edge to arrive at a collisional Bohm criterion:

$$a_l = -\frac{(\lambda_{\mathrm{De,c}}/\lambda_{in,\mathrm{c}})}{2E'_{\mathrm{se}}} + \sqrt{1 + \left(\frac{(\lambda_{\mathrm{De,c}}/\lambda_{in,\mathrm{c}})}{2E'_{\mathrm{se}}}\right)^2} \tag{3.12}$$

$$= -10(\lambda_{\mathrm{De,c}}/\lambda_{in,\mathrm{c}}) + \sqrt{1 + 100(\lambda_{\mathrm{De,c}}/\lambda_{in,\mathrm{c}})^2}. \tag{3.13}$$

Here, $E'_{\mathrm{se}} = E_{\mathrm{se}}\lambda_{\mathrm{De,c}}/(T_{e,\mathrm{c}}/e)$ is the normalized electric field at the sheath edge and $(\lambda_{\mathrm{De,c}}/\lambda_{in,\mathrm{c}})$ is related to the pressure by Eq. (3.9). In moving from Eq. (3.12) to (3.13), E'_{se} was taken to have a value of 0.05. This comes from the result that the electric field at the sheath edge computed from the PIC simulations is nearly constant and takes this value over the entire range of pressures; see section 3.4.3 and Fig. 3.6. The close agreement between Eq. (3.13) and the PIC simulations shows that the method of Liu *et al* [78] provides an accurate approximation. If E'_{se} is set to ≈ 0.1, which better represents the predictions of the fluid model, then Eq. (3.12) agrees better with the numerical solutions of the fluid model. In other work, Eq. (3.13) has been extended to include finite ion temperatures [91] and can alternatively be derived

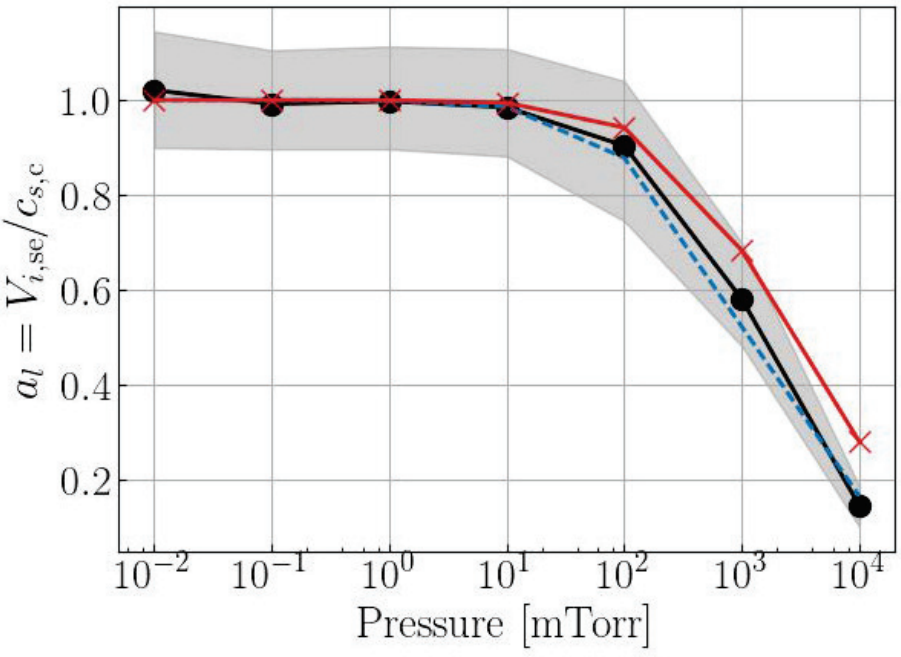

Figure 3.4: Collisional Bohm criterion, a_l, measured from PIC simulations (circles), when P_ρ ranges from 0.0077 to 0.048 (grey), from numerical solutions of the fluid model (crosses), and from Eq. (3.13) (dashed line).

from the generalized Bohm criterion [29], as is shown in appendix B.2.

The fluid model and PIC results for a_l differ slightly at higher pressures. This likely results from each using a different value of P_ρ. Using the same value of P_ρ in the fluid model and PIC does not fix this and instead causes them to differ at low pressures. Practically, both the PIC and fluid data are well represented by Eq. (3.12), though with different choices of the constant E'_{se}.

Other models for the collisional Bohm criterion have also been studied [15, 16, 17, 18]. However, they are based on different fluid models than equations (3.6)-(3.8), particularly with regard to the ionization source model, and so are not directly comparable with our simulations. Several make use of the same ion momentum equation, but assume the plasma is generated proportionally to the density [15, 16, 17]. Alternatively, [18] calculates a_l numerically using the Sagdeev potential, but uses a constant mean-free-path instead of a constant collision frequency model for the

friction force. In addition, [92] uses a different form of the friction force that smoothly transitions between constant mean-free-path and constant collision frequency models. The model of [17] makes similar assumptions as the model we compare with from [78], but is not expressed as an analytic function for a_l, so we do not compare with it here; a comparison between these models is provided in [17].

Finally, we note that previous PIC simulations have observed the collisional Bohm criterion [12]. These 1D-3V PIC simulations included two ion species and generated plasma self-consistently from electron-neutral impact ionization collisions, which is a different ionization source that is better modeled as proportional to the local density. The simulation results for a_l, for each species, were found to agree well with the model of [15].

3.4.2 Edge-to-center density ratio

Figure 3.5 shows the edge-to-center density ratio (h_l) calculated from PIC data (circles), numerical solutions of the fluid model (red crosses), and an analytic approximation (dashed line). The values of h_l are more sensitive at lower pressures than higher pressures, but are relatively robust to changes in P_ρ. Generally good agreement is observed between each of these three models, though the PIC data predicts a smaller value for h_l at the highest pressure and a larger value at pressures below 10 mTorr than the fluid model does.

The model for h_l was derived assuming quasineutrality [$n_i = n_e = \exp(-e\phi/T_{e,c})$] in the fluid model and solving the resulting differential equation; as shown in appendix B.3. Making this assumption greatly simplifies the fluid model and is the same starting point other authors have used to compute h_l [28, 77]. In order to best model the observed h_l factor from PIC we modified the coefficients of the fluid model derived in appendix B.3 so that the low and high pressure limits matched those observed in the PIC simulations. We find that the resulting h_l factor is well

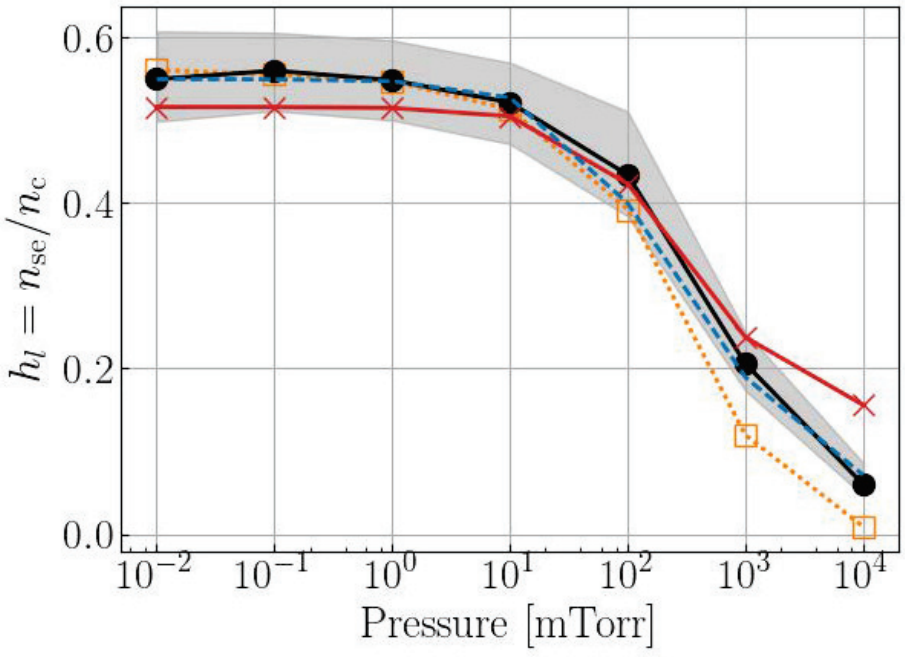

Figure 3.5: Values of h_l calculated from PIC simulations (circles), along with values when P_ρ ranges from 0.0077 to 0.048. Values of h_l from numerical solutions of the fluid model (crosses), and from Eq. (3.14) (dashed line). The factor h_l^*, which uses $V_i = c_{s,c}$ to define the sheath edge location (squares).

approximated by

$$h_l = \frac{0.55 + 0.5(\lambda_{De,c}/\lambda_{in,c})}{1 + 30(\lambda_{De,c}/\lambda_{in,c})}. \tag{3.14}$$

There is a notable difference in the fluid and PIC values for h_l at low pressure with PIC reaching 0.55, whereas the fluid model predicts a value of 0.50. This difference may be due to non-local kinetic effects that the fluid model does not capture. For instance, the electron velocity distribution function (EVDF) may deviate significantly from a truncated Maxwellian, which has been observed in other PIC simulations [87, 93]. This is an effect that cannot be captured by the fluid model which implements the Boltzmann relation.

Figure 3.5 also shows a comparison with h_l^* obtained from the PIC data. Here, h_l^* is defined as the edge-to-center ion density ratio if $V_i = c_{s,c}$ defines the sheath edge.

We compare with h_l^* because the most common models of h_l use this sonic condition to define the sheath edge [28, 77], which is not consistent with the collisional Bohm criterion. Alternatively, h_l^* has also been interpreted as the ratio of the ion flux at the sheath edge to the value $n_{\mathrm{c}} c_{\mathrm{s,c}}$ [83], but this does not correspond to the edge-to-center density ratio in view of the collisional Bohm criterion. Instead, it corresponds to $h_l^* = a_l h_l$. We stress that it is useful to define h_l as a density ratio, rather than a flux ratio, and the sheath edge as the location where quasineutrality breaks down. For example, this distinction is important in order to compute the sheath potential drop since the electron and ion densities can be equated at the sheath edge, leading to the result that the plasma potential depends on a_l, but not h_l; see section 3.4.4. This point is lost when h_l is defined as a flux ratio, or when the sheath edge is defined based on the sonic point. As expected, Fig. 3.5 shows that h_l and h_l^* agree at low pressures where $a_l = 1$, but at higher pressures h_l^* is lower. For example at 10^3 mTorr the PIC data gives $h_l = 0.21$ and $h_l^* = 0.12$. It is important to note that at 10^4 mTorr h_l^* represents the value of $n(x)/n_{\mathrm{c}}$ at the wall since there is no place in the plasma where $V_i = c_{\mathrm{s,c}}$.

Previous work has also used PIC simulations to test models of the edge-to-center density ratio. Lafleur *et al* [83] found good agreement between 1D-3V simulations and the standard formula for h_l^* [77] over a broad range of pressures, particularly in a simulation setup that modeled inductively coupled plasmas. These simulations sourced the plasma from ionizing electron-neutral collisions instead of the uniform source that we applied, which aligns more closely with a source rate that is proportional to the local density. They also focused on the flux ratio, rather than the density ratio, and so measured h_l^* rather than h_l and a_l individually. An additional important result of that work was showing that ionization and electron heating mechanisms are modified in capacitively coupled plasmas at high pressure, which leads to a breakdown of the models for h_l.

Finally, measurements of the edge-to-center density ratio have been made in a cylindrical, inductively coupled, argon plasma device using a the floating harmonic method [94]. They found good agreement between the theoretical models reviewed in [46] over pressures ranging from about 1 to 30 mTorr. Though their results used a cylindrical device and argon, we can compare with our results by estimating $\lambda_{\mathrm{De,c}}/\lambda_{in,\mathrm{c}} \approx 0.01$ for their measurements at 30 mTorr. To do this we estimated the cross section for argon ion-neutral cross section from LXCat as $\sigma \approx 5 \times 10^{-19}\mathrm{m}^2$ since this corresponds to the cross section evaluated near the experimental ion and neutral temperatures (300 K). This sits somewhere between our 10^3 and 10^4 mTorr simulations where $h_l \approx 0.1 - 0.2$. Their experimental value, taken from figure 2 of [94], was 0.14 which agrees well with what we observe.

3.4.3 Electric field at the sheath edge

Figure 3.6 shows values of the electric field at the sheath edge from the PIC simulations (circles) and numerical fluid model (crosses). The value of E_{se} from both PIC and the fluid model are quite constant over six orders of magnitude in pressure. As a result, we choose to model E_{se} as a constant value based on the PIC result when constructing our model of a_l:

$$E_{\mathrm{se}} = 0.05(T_{e,\mathrm{c}}/e)/\lambda_{\mathrm{De,c}}. \tag{3.15}$$

It is interesting that, although the PIC and fluid models predict fairly constant values for E_{se}, the PIC data predicts the electric field to be about half as strong at all pressures. This is likely a result of P_ρ having different values in PIC and the fluid model. However, the utility of modeling E_{se} is that it lets us evaluate Eq. (3.13) for a_l. Comparing the grey regions in Fig. 3.4 and 3.6 we see that, at higher pressures, changes in E_{se} have a weak effect on a_l. The fact that E_{se} is quite constant with

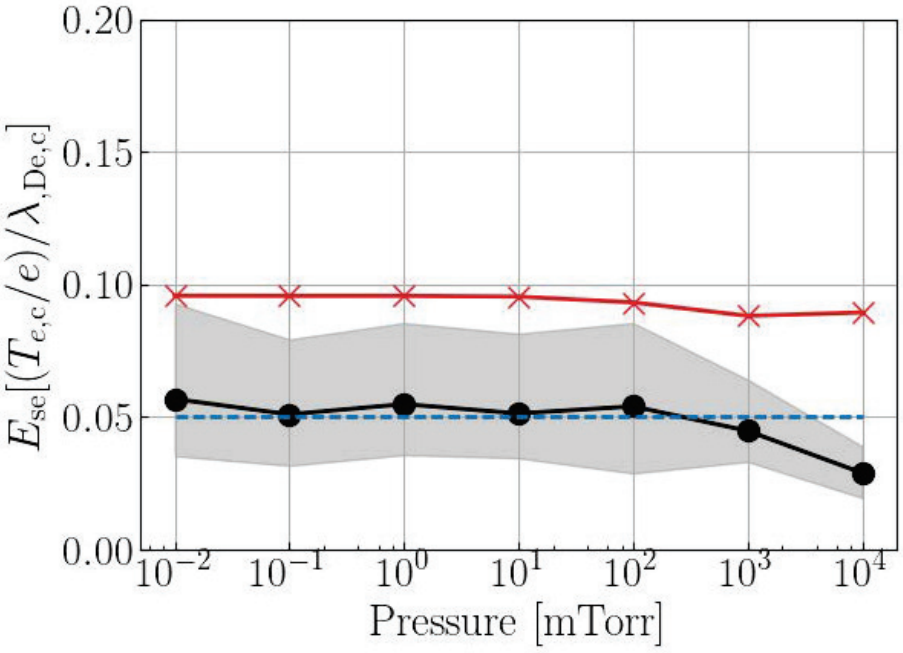

Figure 3.6: Values of $E_{\rm se}$ calculated from PIC simulations (circles), and when P_ρ ranges from 0.0077 to 0.048 (grey region). Values of $E_{\rm se}$ from numerical solutions of the fluid model (crosses). The proposed model for $E_{\rm se}$ (dashed).

pressure also indicates that defining the sheath edge as the point where quasineutrality breaks down is consistent with defining the sheath edge using a critical value of the electric field, though the correct value must be chosen.

Finally, we point out that there has been significant work done to calculate $E_{\rm se}$ by others. However, most of this work was done using a fluid model that takes the plasma source rate to be proportional to n_e [15, 95, 96]. Perhaps as a result, the values of E_{se} that these models predict are significantly larger than the values shown in Fig. 3.6. Most notably, the model used in [15] takes $E_{\rm se} = (T_{e,\rm c}/e)/\lambda_{\rm De,se} = \sqrt{h_l}(T_{e,\rm c}/e)/\lambda_{\rm De,c}$, which is significantly greater than our simulations predict. Alternatively, numerical solutions of a kinetic model with a uniform source and only charge-exchange collisions have also been studied, but this applied a different definition of the sheath edge [97].

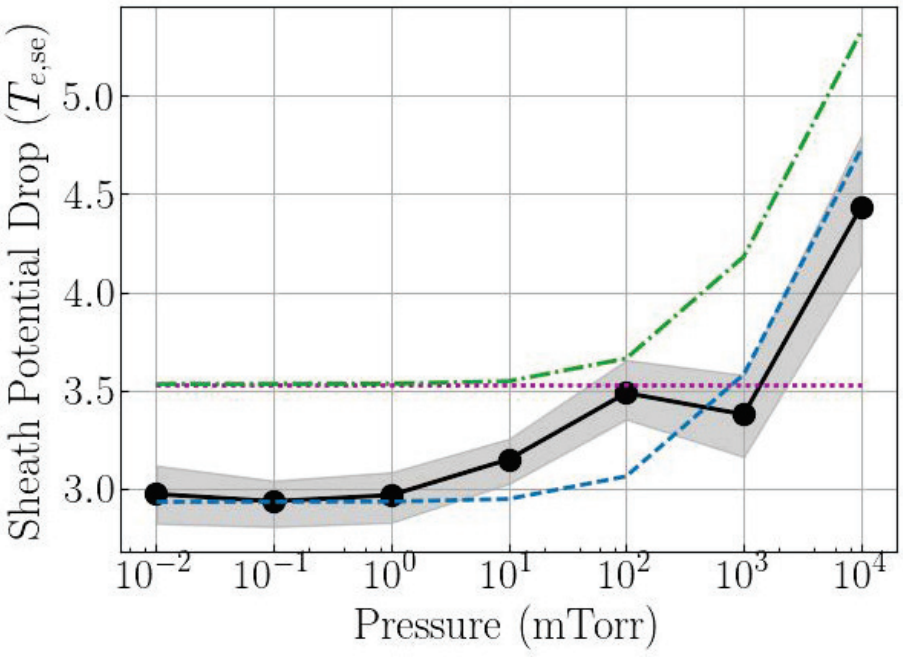

Figure 3.7: Values of $\Delta\phi_\mathrm{s}$ calculated from PIC simulations (circles), and when P_ρ ranges from 0.0077 to 0.048 (grey region). Prediction of Eq. (3.17) (dashed), Eq. (3.16) (dash-dotted), and the collisionless limit of Eq. (3.16) which corresponds to using $a_l = 1$ (dotted).

3.4.4 Sheath and presheath potentials

A practical result of distinguishing the collisional Bohm criterion from the edge-to-center density ratio is that the potential drops across the presheath and sheath can be estimated using models of a_l and h_l. The sheath potential is usually determined from balancing the electron and ion fluxes at the sheath edge. At higher pressures the ion flux is reduced from its low pressure value by a_l ($\Gamma_{i,\mathrm{se}} = h_l n_\mathrm{c} a_l c_{\mathrm{s,c}}$), while the electron flux is still the random thermal flux ($\Gamma_{e,\mathrm{se}} = \frac{1}{4} h_l n_\mathrm{c} \sqrt{8T_{e,\mathrm{se}}/\pi m_e} \exp(-e\Delta\phi_\mathrm{s}/T_{e,\mathrm{se}})$). The fact that the electron flux is largely unaffected by electron-neutral collisions is supported by Fig. 3.2 (b). A result of collisions affecting only the ion flux is that the plasma potential must increase to reduce the electron flux to that of the collisionally

modified ion flux. Balancing the electron and ion fluxes gives:

$$\begin{aligned}\frac{e\Delta\phi_{\mathrm{s}}}{T_{e,\mathrm{se}}} &= -\frac{1}{2}\ln\left(a_l^2 2\pi\frac{m_e}{m_i}\frac{T_{e,\mathrm{c}}}{T_{e,\mathrm{se}}}\right)\\ &\approx -\frac{1}{2}\ln\left(a_l^2 2\pi\frac{m_e}{m_i}\right) \qquad (3.16)\\ &\approx -\frac{1}{2}\ln\left(1.8a_l^2 2\pi\frac{m_e}{m_i}\right) \qquad (3.17)\end{aligned}$$

Here the factor $T_{e,\mathrm{c}}/T_{e,\mathrm{se}}$ inside the logarithm represents a small change in the model and is approximated as 1 in Eq. (3.16). The factor of 1.8 is multiplied inside the logarithm to reflect the PIC data in Eq. (3.17). Equation (3.16) (dash-dotted) and (3.17) (dashed) are plotted in Fig. 3.7 , where we have inserted Eq. (3.13) for a_l. The collisionless prediction, obtained from taking $a_l = 1$ in Eq. (3.16), is shown as the horizontal dotted line in Fig. 3.7. A line from the fluid model is not included since the wall was defined as the point where the potential drop across the sheath equaled Eq. (3.16).

The prediction of Eq. (3.16) increases with pressure as expected, however, it generally over predicts what is measured in the PIC simulations. We suspect this is a kinetic effect that is captured in the PIC simulations, but not the fluid model. In kinetic models of the sheath it is expected that the EVDF will be truncated since only electrons with enough energy will escape the plasma. However, if this truncation is not sharp, but instead the EVDF above the truncation is only partially depleted, then the EVDF is better represented by a two-temperature distribution where the tail population is significantly cooler [87, 93, 98]. Since only the tail electrons contribute to the electron flux leaving the plasma, and so the potential, it is the tail temperature that should be used in Eq. (3.16). Ultimately the effect of a depleted tail is a reduction in the potential so that flux of electrons balances that of the ions.

The potential drop across the presheath can be approximated by assuming the

presheath is quasineutral and that the density follows a Boltzmann density relation:

$$\frac{e\Delta\phi_{\mathrm{ps}}}{T_{e,\mathrm{c}}} = -\ln(h_l). \tag{3.18}$$

This formula is represented by the dashed line in Fig. 3.8, where h_l is computed using Eq. (3.14). The PIC and fluid data generally show good agreement, though Eq. (3.18) slightly under predicts the PIC measurements at low pressure and overestimates at high pressure.

Finally, we note that the effect of pressure on the plasma potential has been studied in several other settings: numerical fluid models [92], analytic fluid models [28], and experimentally [99]. In each case the potential drop across the presheath was observed to increase as pressure increases; however, direct comparison is difficult since [92] does not include a formula for comparison, [28] uses a non-uniform source, and [99] studied the potential in an argon discharge.

3.4.5 Sheath width

Figure 3.9 shows the calculations of the sheath width. Here, $\lambda_{\mathrm{De,c}}$ is calculated at the center of the plasma. The PIC simulations and fluid model both predict that the sheath becomes thicker as pressure increases. A simple estimate for the change in sheath thickness with pressure can be obtained by simply accounting for the reduction in the ion flux at the sheath edge in the Child-Langmuir law. The Child-Langmuir law is [76]:

$$\frac{w_{\mathrm{s}}}{\lambda_{\mathrm{De,c}}} = \frac{\sqrt{2/(\Gamma_{i,\mathrm{se}}/n_{\mathrm{c}}c_{\mathrm{s,c}})}}{3}\left(\frac{2e\Delta\phi_{\mathrm{s}}}{T_{e,\mathrm{c}}}\right)^{3/4}, \tag{3.19}$$

where $\Delta\phi_{\mathrm{s}}$ is the potential drop across the sheath and $\Gamma_{i,\mathrm{se}}$ is the ion flux at the sheath edge. In the usual application of the Child-Langmuir law $\Gamma_{i,\mathrm{se}} = n_{\mathrm{c}}c_{\mathrm{s,c}}$. To

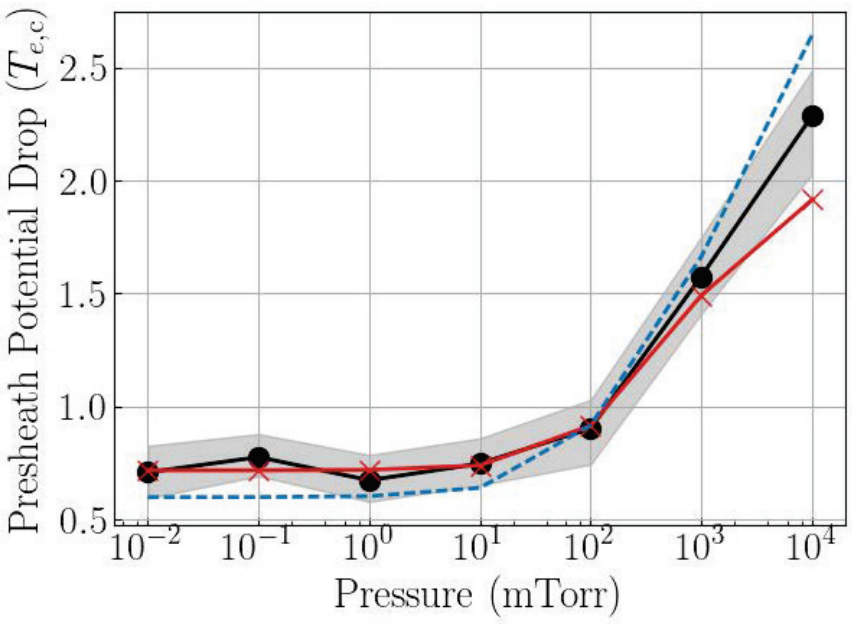

Figure 3.8: Presheath potential drop $\Delta\phi_{\rm ps}$ calculated from PIC simulations (circles) and when P_ρ ranges from 0.0077 to 0.048 (grey). The values of $\Delta\phi_p$ from numerical solutions of the fluid model (crosses) and the prediction of Eq. (3.18) (dashed) are also shown.

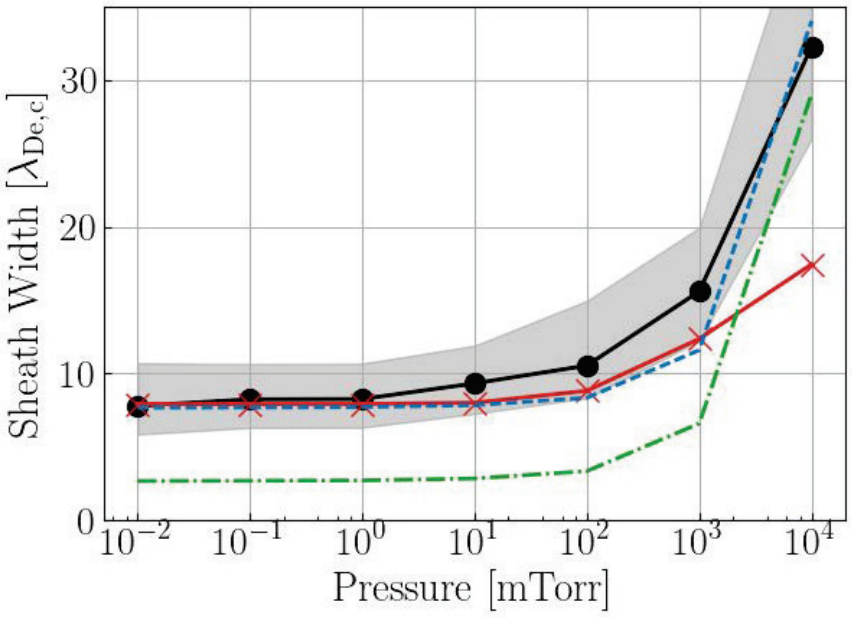

Figure 3.9: Sheath width from the PIC simulations (circles), and when taking P_ρ to range from 0.0077 to 0.048 (grey). Here $\lambda_{De,c}$ is the Debye length at the center of the domain. Sheath width predicted from numerical solutions of the fluid model (crosses), from Eq. (3.20) (dash-dotted), and from Eq. (3.20) including a shift of 5 (dashed).

account for a reduction in the flux we can simply apply $\Gamma_{i,\mathrm{se}} = h_l a_l n_\mathrm{c} c_\mathrm{s,c}$, to get

$$\frac{w_\mathrm{s}}{\lambda_\mathrm{De,c}} = \frac{\sqrt{2/h_l a_l}}{3}\left(\frac{2e\Delta\phi_\mathrm{s}}{T_{e,\mathrm{c}}}\right)^{3/4}. \tag{3.20}$$

An evaluation of this expression using equations (3.13), (3.14), and (3.16) is shown as the green dash-dotted line. High pressure leads to an increase in the sheath width in two ways: by increasing the potential drop across the sheath (Eq. (3.16)) and reducing the ion flux into the sheath. However, it is well known that the Child-Langmuir law is not very accurate at predicting the sheath width, even in the low pressure regime where it is typically applied [27, 100]. This is due to neglecting electrons entirely in the sheath [101]. We find that the inaccuracy is nearly a constant shift across the pressure range, so that adding 5 to Eq. (3.20) results in a model that fits the PIC data well (blue dashed line). The model we propose is also quite similar to that found in [101], where $w_s = 5\lambda_\mathrm{De,se} = 5/\sqrt{h_l^*}\lambda_\mathrm{De,c}$. Our model is effectively the same as this, but we found that adding, instead of multiplying by 5, better represents the PIC data.

It is worth noting that a self-consistent model of the sheath width can be derived by integrating Eq. (3.2) up to the sheath edge ($x : 0 \rightarrow L - w_s$), giving $w_s = L - n_o c_{\mathrm{s,c}} a_l h_l / S$. This relationship accurately predicts the simulated value of w_s when the PIC data is inserted for h_l and a_l. However, we find that it is sensitive to the accuracy of the models for h_l and a_l. For this reason, Eq. (3.20) provides a more practical model.

Other models of the sheath width include [82], which uses the same fluid model as this work. Because it treats only the collisional regime, the result scales inversely with the collisionality $\lambda_\mathrm{De,c}/\lambda_{in,\mathrm{c}}$, and so predicts a very wide sheath at low pressures. This is a common feature of other models for the collisional regime like the well-known Warren [102] and Mott-Gurney [103] models which assume constant collision

mean free path and constant collision frequency, respectively. Both of these models are summarized in [104] where the authors propose a model for the sheath width that captures both the collisionless and collisional limits. In [79] the author discusses the connection of the Warren and Mott-Gurney laws to the Child-Langmuir law and to others that included electron space charge. Finally, an expression for the sheath width is derived for constant mean free path and constant collision frequency models is derived in [80], but with a non-uniform source.

There is at least one measurement of the sheath width at pressures near 10^3 mTorr [105]. Their measurements were made in a DC argon discharge using laser induced fluorescence and laser optogalvanic spectroscopy and they defined the sheath edge as the point where $E = 0$ V/m. They found that the sheath width decreased with pressure when measured in units of mm. This is not necessarily inconsistent with what we observe in Fig. 3.9 since our sheath width is measured in terms of $\lambda_{\mathrm{De,c}}$. The electron temperature was not reported in [105] so we cannot compare directly with our model.

3.4.6 Isothermal electron assumption

Figure 3.1 (e) clearly shows that electrons in the PIC simulations are not really isothermal. The temperature gradient is due to the preferential loss of high energy electrons through the sheath, which causes a depletion of the tails of the electron energy distribution function at an energy correspoding to the local plasma potential [29]. In recent works, attempts have been made to model this effect by replacing the isothermal assumption with an adiabatic assumption [$d(n_e^{1-\gamma}T_e)/dx = 0$]. This modifies Bohm's criterion by a factor of the polytropic index (γ) and the result depends on the electron temperature at the sheath edge ($V_{i,\mathrm{se}} \geq \sqrt{\gamma T_{e,\mathrm{se}}/m_i}$), rather than in the bulk [87, 88, 89]. Following the method in [87], we found $\gamma \approx 1.1 - 1.3$ depending on the pressure, which is lower than what others have found [87]. Account-

ing for this effect leads to small changes in the results because $T_{e,\mathrm{c}} \approx \gamma T_{e,\mathrm{se}}$. Defining P_ρ based on the location that $V_{i,\mathrm{se}} = \sqrt{\gamma T_{e,\mathrm{se}}/m_i}$ in the lowest pressure simulation leads to $P_\rho = 0.023$ (rather than $P_\rho = 0.019$). This pushes the sheath edge location only slightly farther into the sheath. The ion speed at this location is $V_{i,\mathrm{se}} \approx 1.05 c_{s,c}$. The modified sheath edge location alters the predictions for a_l and h_l by about 10% at low pressures and leads to better agreement between the PIC and fluid models at higher pressures. In fact, the PIC and fluid models of E_{se} agreed better at all pressures. However, using the adiabatic assumption complicates the model because there is currently no model for γ. This must be calculated from the simulated profiles of n_e and T_e as in [87]. Nevertheless, further development of the adiabatic assumption could lead to a better model of the sheath, particularly in the high pressure limit.

3.5 Conclusions

Expressions describing sheath properties, including the edge-to-center density ratio ($h_l = n_{\mathrm{se}}/n_{\mathrm{c}}$) and collisional Bohm criterion ($a_l \equiv V_{i,\mathrm{se}}/c_{\mathrm{s}}$), of a helium plasma over a range of gas pressure from 10^{-2} to 10^4 mTorr were developed. These were based on 1D-3V PIC simulations and a reduced fluid model, where the sheath edge was defined as the point where charge neutrality breaks down. Additionally, expressions for the sheath width ($w_{\mathrm{s}}/\lambda_{\mathrm{De}}$), electric field at the sheath edge ($E_{\mathrm{se}}/(T_e/e\lambda_{\mathrm{De}})$), sheath potential drop ($e\Delta\phi_{\mathrm{s}}/T_e$) and presheath potential drop ($e\Delta\phi_{\mathrm{ps}}/T_e$) were developed. In general h_l and a_l decrease with pressure, while $w_{\mathrm{s}}/\lambda_{\mathrm{De}}$, $e\Delta\phi_{\mathrm{s}}/T_e$, and $e\Delta\phi_{\mathrm{ps}}/T_e$ increase with pressure. Notably, we find that $E_{\mathrm{se}}/(T_e/e\lambda_{\mathrm{De}})$ remains quite constant across the entire pressure range, indicating that a breakdown in quasineutrality corresponds to a specific value of electric field.

At low and intermediate pressures ($10^{-2} - 10^2$ mTorr) the fluid model is an excellent approximation for all but the potential, which differs from the PIC simulations likely from kinetic (non-local transport) effects associated with electron loss to the

boundaries. At the highest pressure, differences between the fluid model and simulations become more apparent and are likely due to electron temperature and stress gradients. These differences lead to the fluid model predicting higher values for h_l and a_l than PIC. As a result, we modify the expression we provide for each quantity to best represent the PIC observations by adjusting coefficients in the expressions.

The next step in validation for this model is comparison with experimental measurements over the pressure range considered here. The constant source rate used in our simulations and model represents plasmas where there is a diffuse ionizing population of electrons as in multi-dipole chambers with filament sources and in some hollow cathode discharges.

CHAPTER IV

Electron-Field Instability: Excitation of Electron Plasma Waves by an Ambipolar Electric Field

4.1 Introduction

Macroscopic electric fields that maintain quasineutrality are a common feature found in plasmas, generating ambipolar flows. Systems with such macroscopic electric fields include low temperature plasmas like glows and streamers [46, 106, 107], space plasmas like the ionosphere [108], and fully ionized plasmas like magnetic confinement fusion devices [109] and the solar atmosphere [110]. Although the primary effect of ambipolar-strength electric fields is the transport of plasma by currents, they can also drive instabilities which ultimately cause significant anomalous transport [55, 111, 112, 113]. Currently, electric fields are thought to drive instability by creating relative drifts between plasma species. This is commonly understood via the Penrose criterion, which states that drift energy is converted to wave energy when the relative drift of the streaming populations exceeds a threshold [114]. Here, we use linear theory and particle-in-cell simulations to show that a fundamentally different mechanism for driving instabilities is possible in the presence of an ambipolar electric field. In this "electron-field instability", electric field energy is converted to wave energy via an inverse Landau damping process. This process is not described by the Penrose

criterion. Furthermore, the wave frequency is characteristic of the electron plasma frequency, $\omega_{pe} = (e^2 n_e/\epsilon_o m_e)^{1/2}$, which is much larger than the ion plasma frequency, $\omega_{pi} = (e^2 n_i/\epsilon_o m_i)^{1/2}$, that characterizes most current-driven instabilities.

Common examples of kinetic instabilities include the ion-acoustic or Buneman instabilities, which are driven by a relative drift of electrons and ions, or beam instabilities that are driven by relative drifts between different electron populations [10]. The excitation of each of these instabilities can be described in terms of the shape of the total velocity distribution function (VDF):

$$F_{\text{total}} = F_e + \sum_i \frac{m_e}{m_i} F_i, \tag{4.1}$$

where F_e is the electron VDF and F_i the VDF of the i-th ion species. Electrostatic kinetic instabilities can occur when F_{total} has multiple peaks. The Penrose criterion [114] quantifies this fact and gives a necessary and sufficient condition on the spacing between and relative height of the peaks for instability. However, we have found that it is not necessary for the total VDF to have multiple peaks for instabilities to occur when a macroscopic electric field is present. Instead, a single peaked VDF can be driven unstable by an ambipolar-strength electric field. Specifically, we show that an electron plasma frequency (ω_{pe}) instability, which we will call the electron-field instability, can be excited by the acceleration of electrons in an electric field.

The idea that an ambipolar-strength field can drive instability from a single peaked distribution is not new. The earliest works on this topic were theoretical and include studies by Fried *et al* [115] with follow up work by Fried and Culler [116]. Their linear stability calculation predicted that electron plasma waves could be driven unstable by an arbitrarily weak electric field; however, they questioned whether the instability was physical or a result of their assumptions. Namely, they assumed that the velocity distribution did not change shape considerably during the growth of the instability

and questioned if this may violate the self-consistency of the linear stability analysis. More recent theoretical studies have also predicted that other instabilities can be driven by electric fields. For example, [117, 118] found that electric fields can drive ion frequency instabilities ($\omega \sim \omega_{pi} \ll \omega_{pe}$) in sufficiently collisional environments, where the VDF reaches a non-Maxwellian steady-state due to the balance between the electric field force and collisional drag. Others have found that an electric field can drive high frequency electromagnetic instabilities in the solar atmosphere, even in the presence of Coulomb collisions [119]. These predictions suggest that electric fields that are present in a variety of systems may excite new classes of instabilities that are not described by the Penrose criterion. However, at present they exist in isolation without experimental or simulation based evidence. Specifically, previous work has predicted instability based on linear dispersion relation and it is not clear if the instability is present in a fully non-linear context. With this in mind, we have designed particle-in-cell (PIC) simulations to test the linear-theory based predictions in [115] and find that the assumptions are consistent with fully non-linear solutions of the Vlasov equation.

Simulations have been used to study a similar mechanism for electric field driven instability before. Specifically, Ref. [120] shows results of simulations of plasma in the presence of the electric field in a low-temperature presheath, showing that ion frequency waves were excited throughout the presheath. This work applied a hybrid PIC-fluid model where the electrons were treated as a fluid using the Boltzmann density relation. This work provided evidence that the type of instabilities first described in [115] may not be entirely mathematical in nature, but might have some place in a physical systems. We aim to build on this work by directly studying the electron instability described in [115] using fully kinetic PIC simulations, which can capture kinetic instabilities and their influence on plasma dynamics [34, 42]. The electron plasma wave instability reported here was not possible in the previous simulations

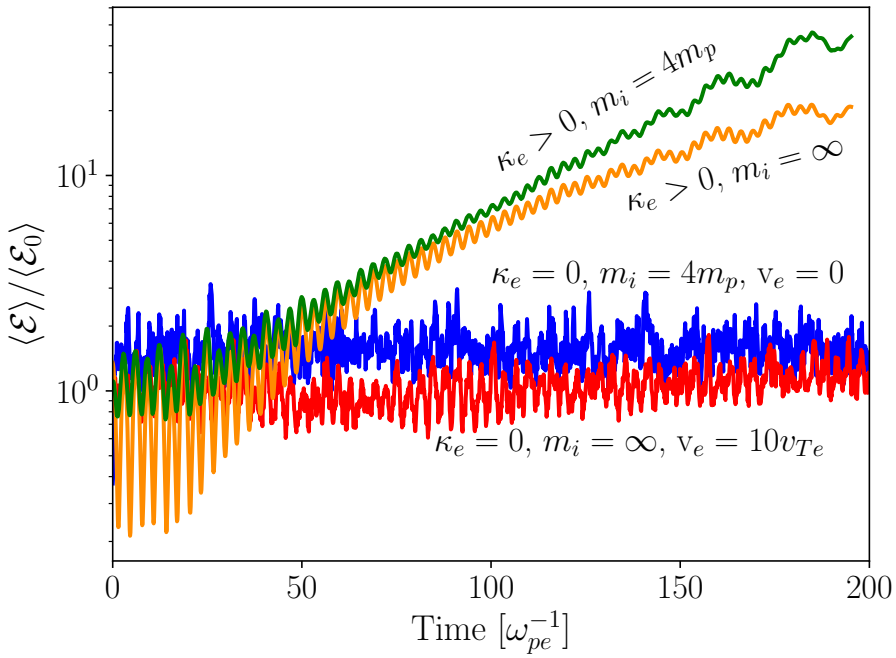

Figure 4.1: Spatially averaged electrostatic energy density in the fluctuating electric field for several simulations. (blue) A simulation with no imposed field or flow and helium ions. (red) A simulation with no imposed field, but an imposed flow of $\mathrm{v}_e = 10v_{Te}$ over immobile ions. (orange) A simulation with $\kappa_e \lambda_{De} = 0.2$ and immobile ions. (green) A simulation with $\kappa_e \lambda_{De} = 0.2$ and helium ions.

from Ref. [120] because electrons were not treated as particles.

Here we compare predictions of linear theory to 1D periodic particle-in-cell simulations of an electron-ion plasma immersed in a uniform electric field. Together the theory and simulations illustrate how a single peaked electron VDF and a macroscopic electric field can combine to drive the electron-field instability. Predictions of the instability dispersion are corroborated by the simulations: the linear growth rate and most unstable wave mode extracted from the simulation compares well with the linear theory. In addition, simulations with stationary ions $m_i \to \infty$ confirm that the instability characteristics do not depend on the ion mass. Finally, we explore how collisional damping by elastic electron-neutral collisions can restrict the pressures and fields at which the electron-field instability would be expected to be observed.

4.2 Simulation setup

Simulations were conducted using the electrostatic PIC-DSMC code Aleph [43]. They used a 1D domain in space, 3D domain in velocity phase-space, and a uniform mesh. The boundary condition for the particles and electric field was periodic in all simulations. The simulations were composed of electrons and ions and the electric field was aligned along the -x direction and had a strength of 800 V/m. This value was chosen since the growth rate associated with this electric field was relatively high, allowing for shorter simulations. Weaker electric fields are predicted to drive the instability and we have confirmed this for a few, more expensive, simulations.

The electric field was imposed by setting the left and right boundaries at different potentials. Alternatively, simulations with no applied boundary potential, but where a constant force was added to the solution of Poisson's equation, showed the same results. This confirmed that there were no unexpected numerical artifacts from the application of two distinct voltages to the periodic boundaries.

The density of both electrons and ions was set to 3×10^{14} m^{-3}, the electron temperature was 3 eV, and the ion temperature was 0.026 eV. The corresponding electron Debye length, used for measuring wavenumbers and positions, was $\lambda_{De} = 7.43 \times 10^{-4}$ m. The electron temperature and density remained effectively constant throughout each simulation leading to an electron Debye length that did not change in time. The average number of computational particles per cell was 400 for both electrons and ions. The domain was 1200 λ_{De} in length with 5 cells per λ_{De}. The electric field caused the electrons to accelerate up to $40v_{Te}$ by the end of the simulation. A time step was chosen so that an electron with velocity lower than $40v_{Te} = 40\sqrt{T_e/m_e}$ does not cross an entire spatial cell in one time step, satisfying a CFL-like condition [36]. In each simulation the cell size was $0.2\lambda_{De}$ so that electron heating was absent in the simulations.

The plasma was assumed to be generated from helium, and to be singly ionized.

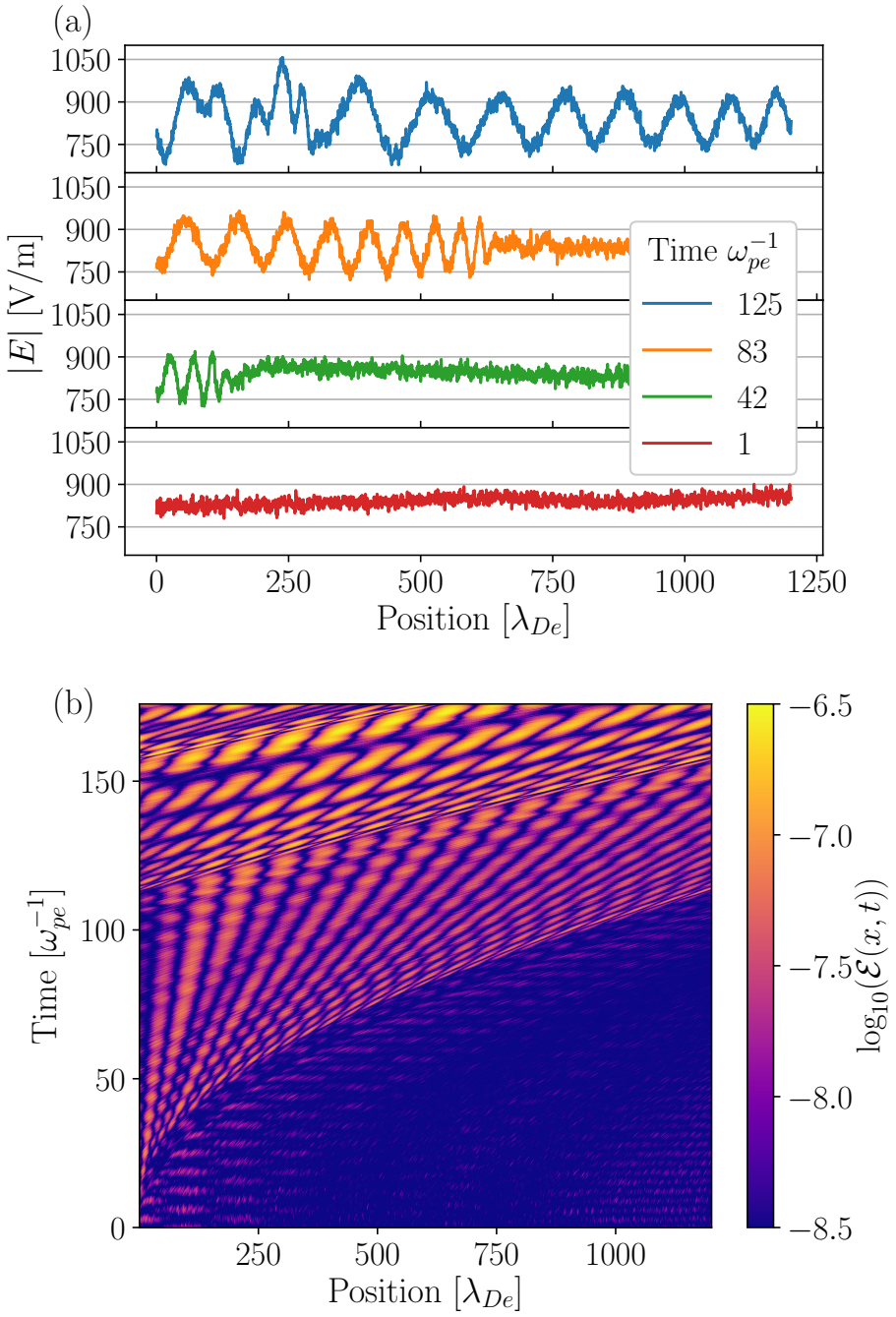

Figure 4.2: (a) Spatial profiles of the absolute value of the electric field for a simulation with $\kappa_e \lambda_{De} = 0.2$. (b) Logarithm of the fluctuation energy density ($\mathcal{E}$) for a simulation with $\kappa_e \lambda_{De} = 0.2$. The instability grows from the left of the domain and travels to the right.

No explicit method, like direct simulation Monte Carlo, was used to model any type of collisions in the simulations. However, Coulomb collisions occurring over large enough distances to be resolved by the grid, though very rare, are expected to be included implicitly in the simulations.

Finally, the figures and accompanying results shown in the following section were found by averaging 16 separate simulations that shared the same general configuration, but with different initial positions and velocities for the particles. This was done to further reduce the statistical noise in the field fluctuations at early times.

4.3 Results

The hallmark of an instability is the exponential growth of the electric field resulting from the conversion of particle energy (here derived from the imposed field) to fluctuating field energy, making the energy of the electric field fluctuations the most direct diagnostic. The energy of the electric field fluctuations was computed from

$$\mathcal{E}(x,t) = \frac{\epsilon_0}{2}[\mathrm{E}(x,t) - \bar{\mathrm{E}}(x)]^2, \tag{4.2}$$

where $\bar{\mathrm{E}}(x)$ is the time-averaged electric field at position x and ϵ_0 is the vacuum permittivity. The time average was taken over the entire simulation duration. The spatial average of $\mathcal{E}(x,t)$ is shown for several simulations in Fig. 4.1, and is denoted by $\langle\mathcal{E}\rangle$. The spatial average was taken over the whole domain and then divided by its initial value, $\langle\mathcal{E}_0\rangle$. Here, the electric field is measured in terms of the electron temperature and electron Debye length through the dimensionless quantity

$$\kappa_e\lambda_{De} \equiv (e\mathrm{E}_0/T_e)\lambda_{De}, \tag{4.3}$$

where E_0 is the imposed macroscopic electric field. The simulations clearly show that the applied electric field excites an instability since the electric field energy increases drastically in simulations with an imposed field (orange and green lines). Conversely, simulations without an imposed field show no growth in the field fluctuations (blue and red lines).

Since an electric field is prescribed on a periodic boundary the electrons and ions constantly accelerate in opposite directions, leading to large average electron velocities ($v_e \sim 10 v_{Te}$) at later times. A relative drift between electrons and ions is known to drive the ion-acoustic or Buneman instability [10]. To show that the fluctuations we observed were due to the electron-field instability and not the ion-acoustic or Buneman instability we also simulated a plasma with an imposed electric field consisting of electrons and immobile ions ($m_i \to \infty$). Since the growth rate of the ion-acoustic and Buneman instabilities scales with m_e/m_i, the simulations with immobile ions exclude the possibility that they arise. This can also be seen from Eq. (4.1) and the Penrose criterion, as the total VDF becomes a single-peaked (electron only) distribution in the limit that $m_i \to \infty$. Figure 4.1 shows essentially no difference between the simulations with mobile (green line) and immobile (orange line) ions, indicating that the ion-acoustic or Buneman instabilities, if present in our mobile ion simulation, does not explain the observed instability.

The ion-acoustic or Buneman instabilities are not observed even in the mobile ion simulations because they occur at a much lower frequency (ω_{pi}) than the frequency of the electron-field instability (ω_{pe}). Furthermore, their growth rate is at least 10 times smaller than that of the electron-field instability based on the strength of the imposed field in the simulations. In fact, a simulation (Fig. 4.1 red line) with immobile ions where an electron flow ($v_e = 10 v_{Te}$) was imposed without an electric field showed no instability over the simulated timescale of $200\omega_{pe}^{-1}$. In all simulations the densities and temperatures remained essentially constant, owing to the high spatial and velocity

resolution.

Figure 4.2 (a) shows spatial profiles of $\mathrm{E}(x,t)$ at several early times while the instability is growing in a simulation with a relatively strong electric field ($\kappa_e\lambda_{De} = 0.2$). At the earliest time (bottom line) a relatively constant electric field is observed. After about 40 ω_{pe}^{-1} (green line) some oscillations near the left boundary arise. As time increases, the instability moves across the domain from left to right (green and orange lines), which is in the opposite direction of the imposed field. The 83 ω_{pe}^{-1} profile shows that the instability has a wavelength of $\approx 30\lambda_{De}$. We can also observe in Fig. 4.2 (a) that the wavelength increases (wavenumber decreases) as time increases and that the wave profile is not exactly uniform (orange), but with a shorter wavelength near the front of the wave. The change in wavelength results from the accelerating electron VDF and is discussed further in section 4.4. Finally, after 125 ω_{pe}^{-1} (blue), the short wavelength front reaches the end of the domain and reenters the other end of the periodic box, causing overlap with the longer wavelength back end of the wave and the nearly monochromatic wave to exhibit beat wave features. In addition to the change in wavelength, the amplitude of the wave increases between each profile, which is most noticeable between 1 ω_{pe}^{-1} and 42 ω_{pe}^{-1}.

The fact that the instability grows from the periodic node (i.e. the left or right boundary) instead of from a random position in the domain is somewhat surprising since the initial state is uniform. We expect the instability to grow from the thermal noise in the plasma, which should be uniformly distributed in space. However, each of the simulations shows the instability starting from the periodic boundary node. This may be caused by the larger error from the field solver (direct, matrix based) on nodes near the left boundary which would lead to a preference in instability growth on the periodic node. We note that when the electric field direction is reversed the instability moves from right to left as excepted by the theory.

Although we can clearly discern the instability from the electric field, it is often

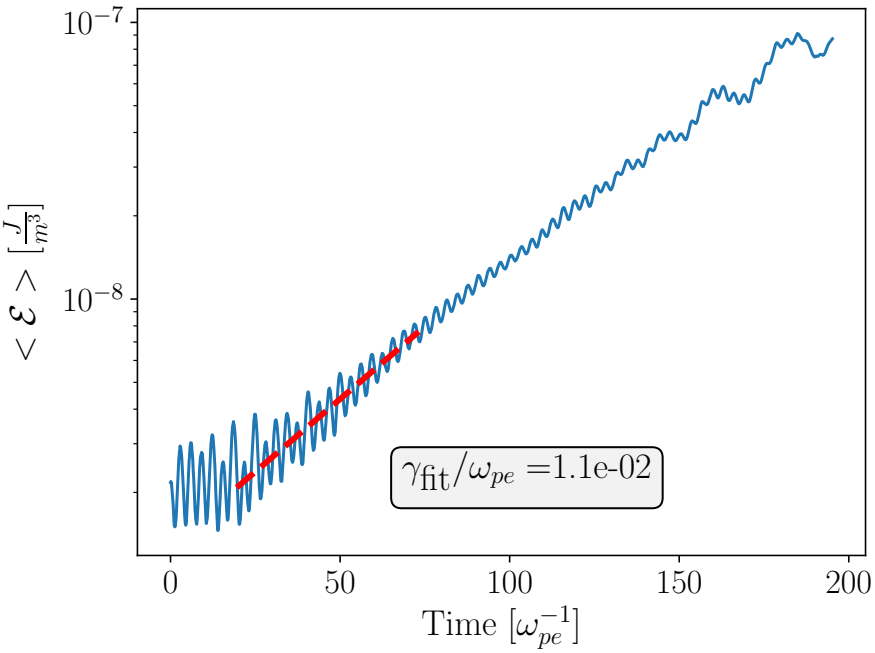

Figure 4.3: Spatially averaged electrostatic energy density in the fluctuating electric field for a simulation with $\kappa_e \lambda_{De} = 0.2$ shown in blue. The spatial average was taken over the whole domain. Times between 75 and 100 ω_{pe}^{-1} were fit (red dashed line) to extract the simulated growth-rate of the instability.

more useful to look at the non-negative fluctuation energy density, $\mathcal{E}(x,t)$. This is plotted as a function of both position and time in Fig. 4.2 (b) and showcases the general features seen in the electric field profiles. At early times (before 100 ω_{pe}^{-1}) the phase speed changes in time as the slope between the region without the wave (dark purple) and with the wave (orange) changes. This continues until the wave makes it to the right boundary and begins to interact with itself as it enters the opposite end through the periodic boundary condition (around 100 ω_{pe}^{-1}). After 100 ω_{pe}^{-1} the waves exhibit significant non-linearity and the peak in the energy density occurs near 150 ω_{pe}^{-1}.

Figure 4.3 shows $\langle\mathcal{E}\rangle$ as a function of time where $k\lambda_{De} = 0.2$ and helium ions were used (solid blue line). After a short initial period ($\sim 35\omega_{pe}^{-1}$), the growth is exponential (linear on the log-linear plot), as expected for a linear growth regime. The exponential growth continues until around 150 ω_{pe}^{-1}, which is the time that non-linear features develop due to the wave exiting one side of domain and entering the other. The linear growth rate was obtained by fitting the log-linear plot with an exponential (red dashed line) during the initial exponential growth period (35-85 ω_{pe}^{-1}), providing a value of $\gamma_{\text{fit}}/\omega_{pe} \approx 1.1 \times 10^{-2}$. The value predicted by the linear stability analysis described in Sec. 4.4 is $\gamma/\omega_{pe} \approx 1.2 \times 10^{-2}$, which is very close to the measured value.

Finally, a more detailed view of the wave modes excited by the instability is provided in Fig. 4.4, where the spatial Fourier transform of $\mathcal{E}$ is plotted. There is a clear increase in the spectral energy density in the simulation. Fig. 4.4 shows the initial growth taking place at about $40\omega_{pe}^{-1}$ and continuing throughout the simulation. The Fourier transform more clearly illustrates that the wave mode with the most energy shifts to lower and lower $k\lambda_{De}$ (larger wavelength) as the electrons accelerate in the simulation. The dotted line shows the analytic approximation of the most unstable mode versus time, which agrees well with the simulations. An additional

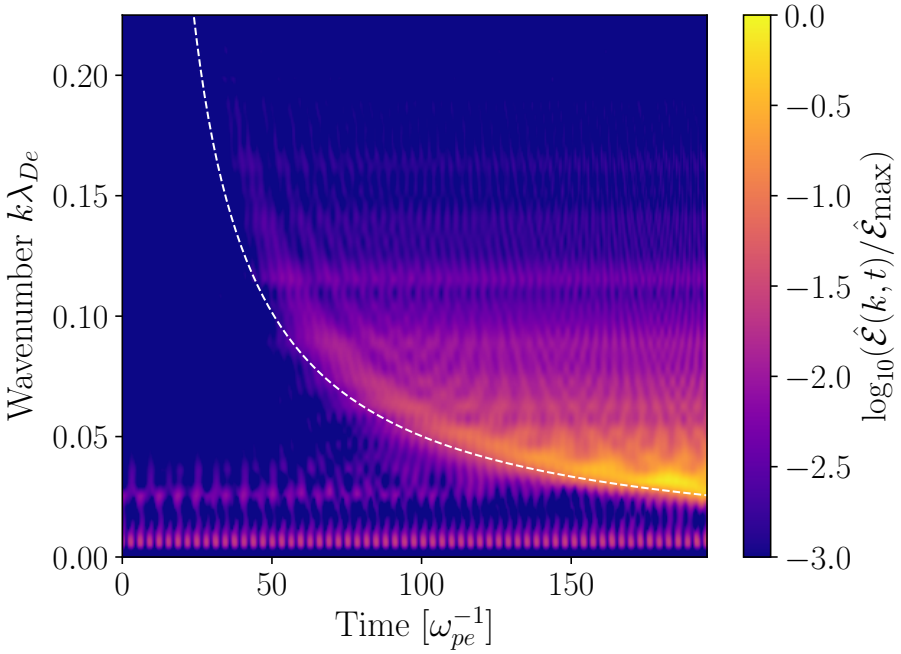

Figure 4.4: Wavenumber spectrum of electrostatic energy density in the fluctuating electric field for a simulation with a non-zero DC electric field. The dotted line represents the prediction of Eq. (4.12) for the dependence of the most unstable $k^*\lambda_{De}$ on time.

feature highlighted by the Fourier transform data is the lifetime of the excited modes. For example, we can follow a horizontal line around $k\lambda_{De} = 0.08$ from 50 to 200 ω_{pe}^{-1} and see that the energy in that mode is effectively constant (same color) meaning that any damping is not significant on the time scale of the simulation, which is consistent with the modes being unstable.

4.4 Dispersion relation

The previous section showed PIC simulation results of electron-plasma waves excited by an electric field. Here, the main features of the simulation results are interpreted based on a linear stability analysis of the Vlasov equation including a steady-state electric field, as was first done in [115]. Since ions are stationary at the timescale of electron plasma oscillations, it is expected that ions do not contribute significantly to the dispersion relation, and are therefore excluded. We have checked that including ion effects in the analysis does not significantly change the results presented below. Ultimately, analysis of the linear dielectric response of the electrons in the electric field provides us with expressions of the most unstable wave mode k^* and growth rate γ^* that compare favorably with those observed in the simulations. Furthermore, our analysis captures the time dependent features of the simulated instability (Fig. 4.4) and shows the behavior of $k^*(t)$ is related to the change of wavelength of the most unstable mode as the electrons accelerate.

Starting from the Vlasov equation

$$(\partial_t + \mathbf{v}\cdot\partial_{\mathbf{x}} - \frac{e}{m_e}\mathbf{E}\cdot\partial_{\mathbf{v}})f_e(\mathbf{x},\mathbf{v},t) = 0, \tag{4.4}$$

the distribution function is separated into slowly varying and fluctuating components, $f_e \approx f_{e0}(\mathbf{v}) + f_{e1}(\mathbf{x},\mathbf{v},t)$, as is the electric field, $\mathbf{E} \approx \mathbf{E}_0 + \mathbf{E}_1(\mathbf{x},t)$. The linearized equation is then solved along with Poisson's equation for the linear dielectric function

$\epsilon(\mathbf{k},\omega)$

$$\epsilon(\mathbf{k},\omega) = 1 + \sum_s \frac{e^2}{\epsilon_0 m_e k^2} \int \omega_{fe}^{-1} \boldsymbol{k} \cdot \partial_{\mathbf{v}} f_{e0} d^3\mathrm{v}, \tag{4.5}$$

where $\omega = \omega_r + i\gamma$, and

$$\omega_{fe}^{-1} = -i \int_0^\infty \exp\{i[(\omega - \mathbf{k}\cdot\mathbf{v})\tau - k\kappa_e \lambda_{De}^2 (\tau\omega_{pe})^2/2]\} d\tau, \tag{4.6}$$

and $\kappa_e = e\mathrm{E}_0/T_e$ is a wavenumber representing the strength of the zero-order electric field along $\mathbf{k}$ (i.e $\mathrm{E}_0 = \hat{\mathbf{k}} \cdot \mathbf{E}_0$). The field and wavevector were assumed anti-parallel ($\mathrm{E}_0 < 0$) and κ_e was taken to be positive in Eq. (4.6) and all following expressions. The argument in the exponential of Eq. (4.6) represents the characteristic trajectories of the particles in the presence of a constant electric field. When $\mathrm{E}_0 = 0$, the standard expressions for ϵ is returned as $\lim_{\mathrm{E}_0 \to 0} \omega_{fe}^{-1} = 1/(\omega - \mathbf{k}\cdot\mathbf{v})$. Furthermore, it is often the case that the electrons have a nearly Maxwellian VDF with temperature T_e ($f_{Me} = n_{0e} \exp(-(\mathbf{v} - \mathbf{v}_e)^2/v_{Te}^2)/\pi^{3/2} v_{Te}^3$). Making this approximation allows us to write the linear dielectric as

$$\epsilon_M = 1 - \frac{(k\lambda_{De})^{-2}}{2(1 + i\kappa_e/k)} Z' \left[\frac{(\omega - \mathbf{k}\cdot\mathbf{v}_e)/k v_{Ts}}{\sqrt{2(1 + i\kappa_e/k)}} \right], \tag{4.7}$$

where $Z'(x)$ is the derivative of the plasma dispersion function.

Figure 4.5 demonstrates the effect of the electric field on the roots (black circles) of Eq. (4.7), where the red and blue lines represent the roots of the real and imaginary parts of Eq. (4.7). Panel (a) shows the electron plasma waves with real frequency near $\omega_r/\omega_{pe} \approx \pm 1$ are stable with $\gamma/\omega_{pe} \approx 0$ and two lower frequency modes that are more strongly damped. The effect of the electric field is to shift one of the roots up (here the positive-frequency mode) making it unstable, while the negative frequency mode is made more stable. Finally, panel (c) shows that a strong enough electric field can drive multiple modes unstable. In such cases where multiple modes are excited,

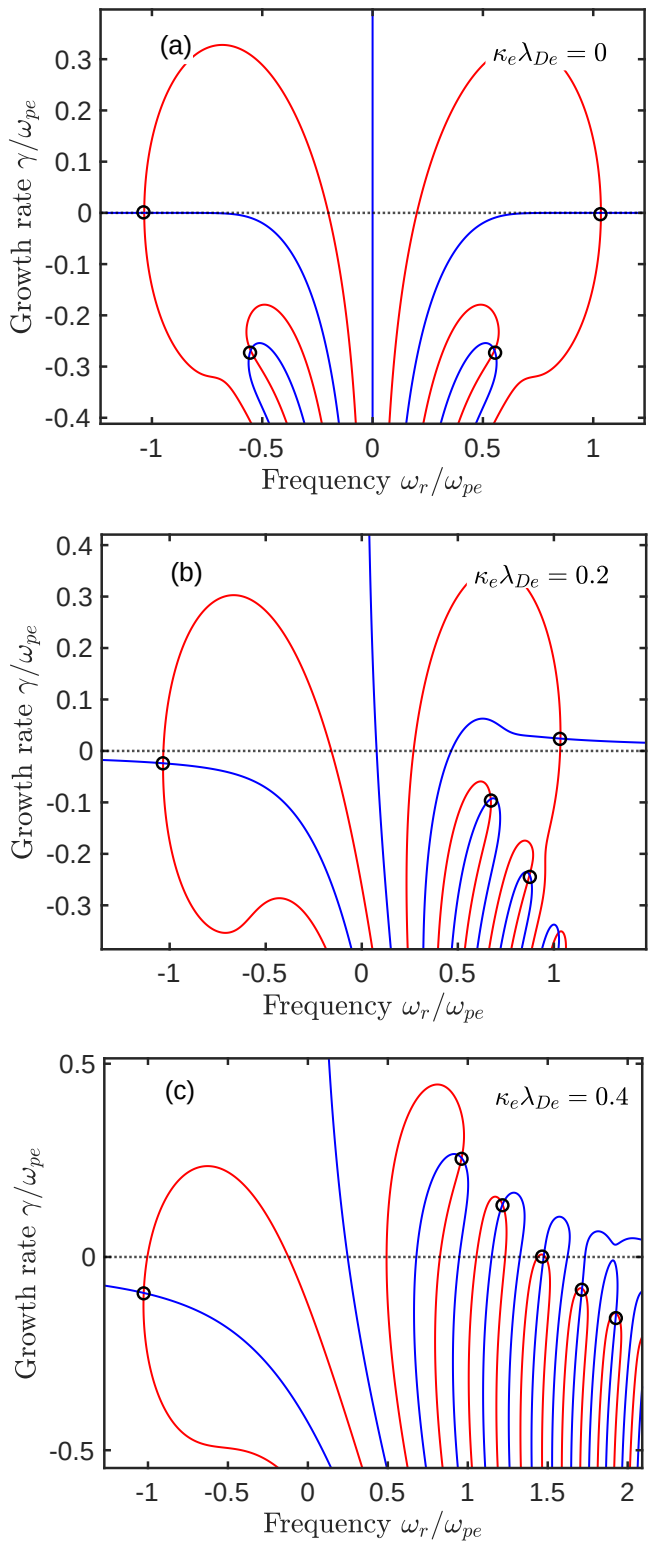

Figure 4.5: Roots of Eq. (4.7) for $v_e = 0$ and (a) no imposed electric field $\kappa_e\lambda_{De} = 0$, (b) a field value where one mode is unstable $\kappa_e\lambda_{De} = 0.2$, (c) and a stronger field where multiple modes are unstable $\kappa_e\lambda_{De} = 0.4$. All plots are for $k\lambda_{De} = 0.15$ and the black circles designate roots, while the red and blue lines represent roots of the real and imaginary parts of Eq. (4.7).

non-linear features may arise more quickly, limiting the applicability of the linear analysis that follows since it approximates only the most unstable mode.

In the simulations described in the previous section, the average electron velocity changes at a constant rate due to the electric field (E_0). We can calculate how the average electron velocity changes in time from $F = ma$ for a constant acceleration, which gives the kinematic equation $v_e(t) = at$. The effect of the accelerating electrons on the dispersion of the instability is illustrated in Fig. 4.6, where Equation (4.7) was solved numerically using Matlab's root finding function *fsolve* for $v_e = 0v_{Te}$ in (a) and $v_e = 10v_{Te}$ in (b). The main effect of the electrons accelerating is to shift ω and γ to lower values.

In addition to the numerical solutions, we can arrive at a relatively simple analytic form for the wave dispersion by starting with Eq. (4.5) and expanding for small E_0 ($\kappa_e\lambda_{De} \ll 1$). An expansion in large phase velocities ($v/(\omega_r/k) \ll 1$) gives a real frequency of

$$\omega_r = \sqrt{\omega_{pe}^2 + 3k^2v_{Te}^2} - kv_e, \tag{4.8}$$

which is the normal electron plasma wave dispersion relation. Equation (4.8) (red dashed line) is compared to the numerical solution of Eq. (4.7) in Fig. 4.6 for $\kappa_e\lambda_{De} = 1/500$, where in (a) $v_e = 0v_{Te}$ and (b) $v_e = 10v_{Te}$. The two agree well for small v_e, but show some disagreement for larger values of v_e as the large phase velocity assumption breaks down as ω_r approaches 0.

Furthermore, assuming the growth rate is small ($\gamma \ll \omega$) we can solve Eq. (4.7) for the growth rate including the effects of the electric field. We find that the lowest order effect of E_0 is to add a term proportional to κ_e onto the well-known expression for the Landau damping rate of electron plasma waves [8]:

$$\gamma/\omega_{pe} = \frac{\omega_r^3}{\omega_{pe}^3}\left(3k\kappa_e\lambda_{De}^2 - \frac{\exp\{-3/2 - 1/(2k^2\lambda_{De}^2)\}}{\sqrt{8/\pi}|k\lambda_{De}|^3}\right). \tag{4.9}$$

Note that in the standard derivation of the Landau damping rate of an electron plasma wave the real frequency (ω_r) in Eq. (4.9) is approximated to first order as the plasma frequency ($\omega_r \approx \omega_{pe}$). Here, we need to account for the Doppler shift in Eq. (4.8), but since Eq. (4.8) becomes inaccurate for large $k\mathrm{v}_e$ (as $\omega_r \to 0$) we find that it is better to approximate ω_r/ω_{pe} in Eq. (4.9) with a step function $\Theta(\omega_r)$. The step function is a better approximation at relatively large $k\lambda_{De}$ as it is not derived from the small growth rate approximation. This models the cutoff in k as $\omega_r \to 0$, which is not captured accurately by the small growth rate approximation. With this approximation, the final expression for the growth rate is

$$\gamma/\omega_{pe} = \Theta(\omega_r)\left(3k\kappa_e\lambda_{De}^2 - \frac{\exp[-3/2 - 1/(2k^2\lambda_{De}^2)]}{\sqrt{8/\pi}|k\lambda_{De}|^3}\right). \tag{4.10}$$

When Eq. (4.10) is compared with the numerical solutions of Eq. (4.7) we see very good agreement as shown in Fig. 4.6 (a) and (b) for $\kappa_e\lambda_{De} = 1/500$. Panel (a) compares the analytic and numerical solutions for a case where the average velocity of electrons in the lab frame is 0, while panel (b) compares the two for an average electron velocity of $10v_{Te}$. A non-zero average velocity greatly affects the real frequency as predicted by Eq. (4.8), while the growth rate is weakly affected. In general, both Eq. (4.9) and Eq. (4.10) are accurate for $k\lambda_{De} \ll 1$ and $\kappa_e\lambda_{De} \lesssim 1$, following the assumptions of large phase velocity and weak field.

We can now estimate the exponential growth rate see in Fig. 4.3 by evaluating Eq. (4.10) at the v_e corresponding to the middle of the fit interval (i.e $\approx 60\omega_{pe}^{-1}$. The average velocity over this period is approximately $10v_{Te}$ and the corresponding average maximum growth rate is found to be $\gamma/\omega_{pe} \approx 1.2 \times 10^{-2}$. This compares favorably with the value extracted from the simulations, shown in Fig. 4.3.

Another important prediction of both Eq. (4.9) and Eq. (4.10), is a maximum k for the instability when $\mathrm{v}_e > 0$. This is associated with the real frequency approaching

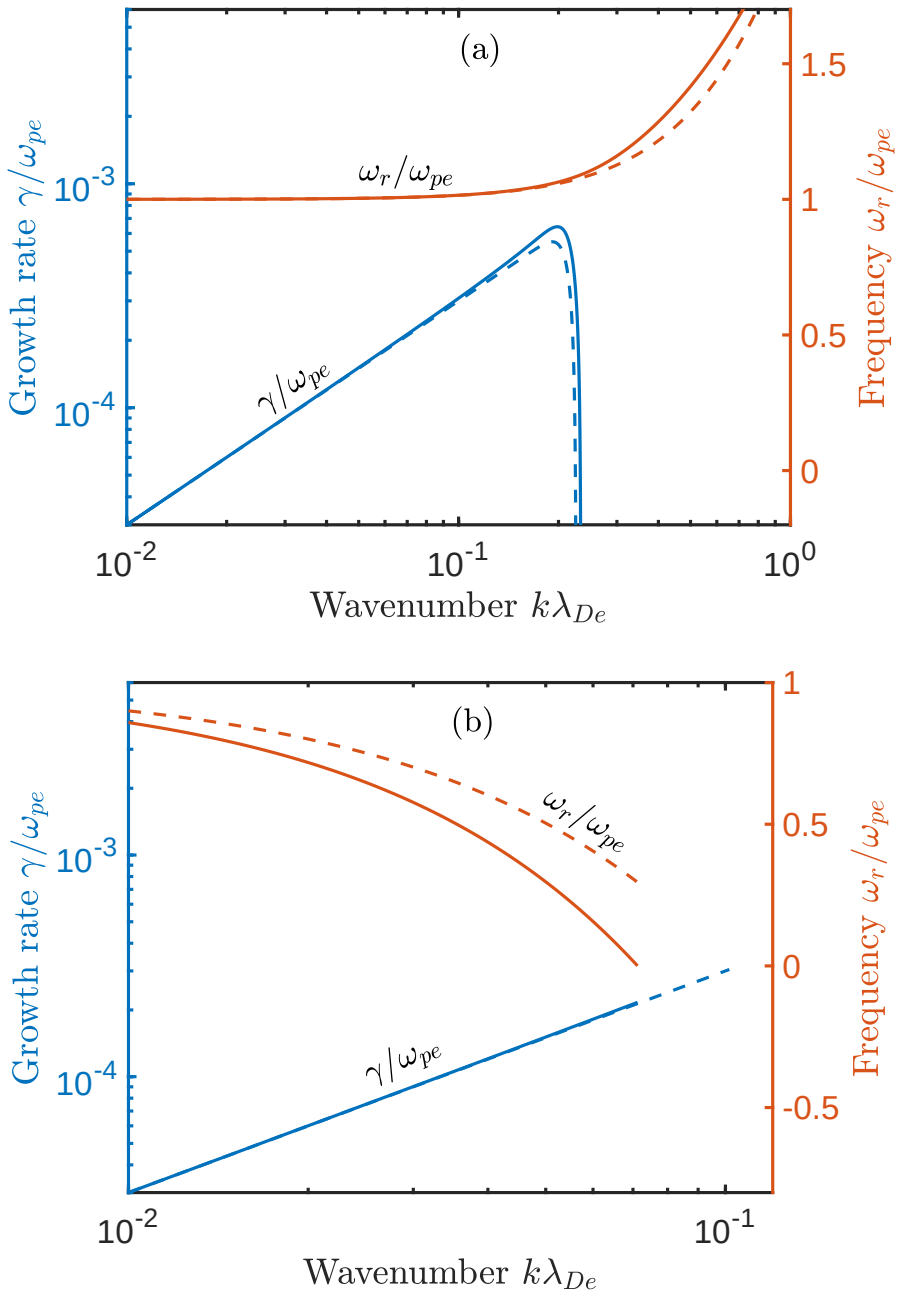

Figure 4.6: Dispersion of electron plasma waves immersed in a constant electric field of strength $\kappa\lambda_{De} = 1/500$. Growth rate (left axis) from Eq. (4.9) (dashed blue) and numerical (solid blue) solutions to Eq. (4.7). Real frequency (right axis) from Eq. (4.8) (dashed red) and numerical (solid red) solutions to Eq. (4.7). Panel (a) shows the dispersion in the rest frame of the electrons, or when the average electron velocity is 0 in the lab frame. Panel (b) shows the dispersion in the lab frame when the electrons have an average velocity of $10v_{Te}$.

zero: $\omega_r \to 0$. The range of k for which there is instability can be approximated as

$$k\lambda_{De} < v_{Te}/\mathrm{v}_e. \tag{4.11}$$

Equation (4.11) is found by setting Eq. (4.8) to 0 and ignoring the $3v_{Te}^2k^2$ term since instability only occurs for $k\lambda_{De} \lesssim 0.2$ making this term small. Equation (4.11) also predicts the most unstable wavenumber, k^*, since γ is an increasing function of k. Taking the dimensionless kinematic expression for the average electron velocity $\mathrm{v}_e/v_{Te} = \kappa_e\lambda_{De}\omega_{pe}t$ and using this in Eq. (4.11) gives a prediction for how the most unstable mode changes with time

$$k^*\lambda_{De} = (\kappa_e\lambda_{De}t\omega_{pe})^{-1}. \tag{4.12}$$

Equation 4.12 is plotted in Fig. 4.4 as the dashed white line and shows great agreement with the downshift in k^* when $\kappa_e\lambda_{De} = 0.2$.

Finally, Fig. 4.7 shows that the growth-rate has a nearly linear dependence on the electric field strength (κ_e) and the most unstable wavenumber (k^*) depends weakly on κ_e. The maximum growth rate can be approximated by

$$\gamma^*/\omega_{pe} \approx (1/2)(\kappa_e\lambda_{De}), \tag{4.13}$$

which was found from Eq. (4.10) where $k^*\lambda_{De} \approx 0.2$ and the second term was ignored since k^* is the most unstable mode. It is important to note that although the growth rate can reach very small values in weak fields, physical systems will always have some sort of collisional dissipation present, suggesting that, in practice, there is a minimum electric field value at which instabilities will be observed. Such dissipation is not self-consistently included in our analysis, since it is based on the collisionless Vlasov equation. Furthermore, comparison of γ^* and k^* for stationary electrons ($\mathrm{v}_e = 0v_{Te}$,

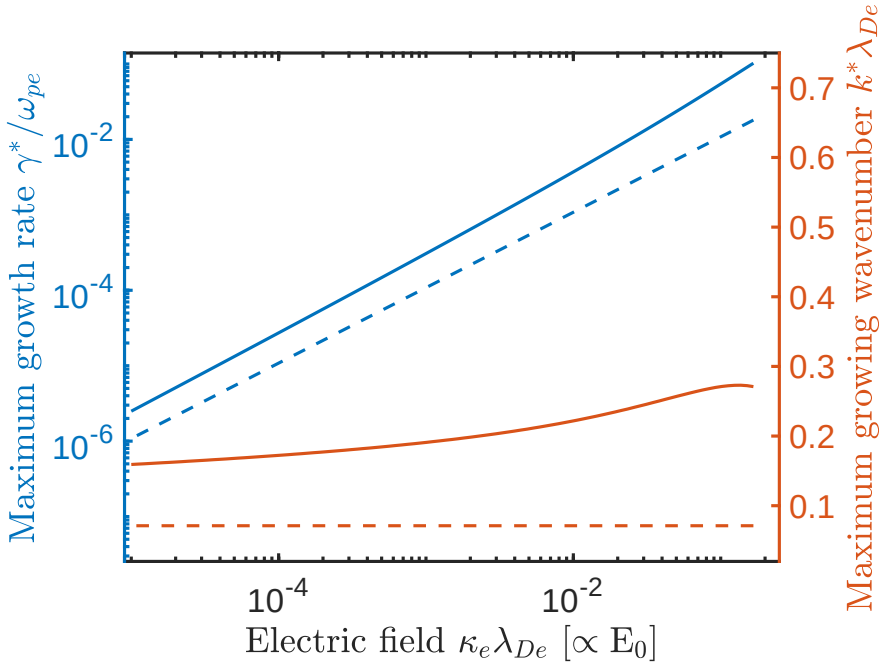

Figure 4.7: Growth rate of the most unstable mode (γ^*) in blue (left axis), most unstable wave mode (k^*) in red (right axis) as functions of the electric field strength. Solid lines represent the values for an average electron velocity of $\mathrm{v}_e = 0v_{Te}$, while dashed lines are for $\mathrm{v}_e = 10v_{Te}$.

solid lines) and drifting electrons ($v_e = 10v_{Te}$, dashed lines) illustrate that the electron drift slightly lowers the growth rate and further weakens the dependence of k^* on the electric field strength.

4.5 Discussion

This section highlights several types of plasmas where the electron-field instability could be excited based on characteristic parameters. Namely, the pressure at which electron-neutral collisions will entirely damp the instability is estimated since many plasmas are partially ionized. Ultimately, we find that the maximum, or cut off, pressure is lower than the ambient pressure in several systems, implying that the instability should be present.

An estimate of the electron-neutral collision rate can be calculated for helium from $\nu_{en} = n_g \sigma_{en} v$, where n_g is the neutral gas density, σ_{en} is the electron-neutral cross section, and v is the relative velocity between an average electron and neutral. After approximating n [m^{-3}] $\approx 3.25 \times 10^{19} p$ [mTorr], taking $\sigma_{en} \approx 6 \times 10^{-20}$ m^2 [65], and $v \approx v_{Te}$ the collision frequency becomes $\nu_{en}/\omega_{pe} \approx 2\lambda_{De} p$[mTorr]. Equating the maximum growth rate (Eq. (4.13)) and collision rate (ν_{en}/ω_{pe}) gives the cut-off pressure above which the instability should be entirely damped:

$$p^*[\text{mTorr}] \approx \kappa_e[\text{m}^{-1}]. \tag{4.14}$$

This predicts, unsurprisingly, that the higher the electric field, the higher the pressure needed to damp the instability. This is a useful formula for determining at what conditions the instability can occur.

The following paragraphs review several systems where electric fields develop and provide estimates for the parameters of the electron-field instability, like field strength, growth rate, and cut off pressure. The characteristic parameters for each system show

System	$\kappa_e \lambda_{De}$	γ^*/ω_{pe}	p^* [mTorr]
Presheath	1.3×10^{-3}	5×10^{-4}	$0.34 - 34$
Positive column (DC)	2×10^{-3}	5×10^{-4}	10
Mesosphere streamer (sprite)	$\gtrsim 0.2$	1×10^{-1}	450
Ionosphere	2×10^{-5}	5×10^{-6}	fully ionized

Table 4.1: Example systems where large-scale electric fields are present. The dimensionless electric field, maximum growth rate, and cut-off pressure are listed. A range of cut-off pressures is provided for systems that have a range of densities.

that the electron-field instability is possible in each. Note that the cut off pressure determined by Eq. (4.14) accounts only for elastic collisions and requires us to know the actual electric field [V/m] in the system or κ_e and the electron Debye length. Often there is a range to the cut-off pressure that is determined by the density and temperature that are typical of the system.

A weak, but large-scale electric field is generally associated with the presheath of low temperature plasma systems. The presheath electric field is responsible for accelerating ions (or electrons near an electron sheath) out of the bulk plasma. In either case the potential drop across the presheath is on the order of T_e and the presheath length-scale is 100s of λ_{De} often as a result of charged-neutral collisions [46]. Here we will assume the presheath is 800 λ_{De}. This allows us to estimate $\kappa_e \lambda_{De} \approx 1/800$ for either presheath as shown in the first row of Table 4.1. The corresponding growth-rate is found from Eq. (4.13) and the cut-off pressure from Eq. (4.14). However, the cut-off pressure depends on κ_e and so an estimate of the Debye length needs to be provided, which depends on the density and temperature of the plasma. Here we calculate the cut-off pressure for a range of plasma densities (and

so λ_{De}) ranging from $3 \times 10^{14} - 3 \times 10^{18}$ m^{-3}. This range of densities represents most low temperature, low pressure plasmas. As a result, we find that the electron-field instability may occur at relatively low pressure in relatively high density plasmas, but at lower densities the pressure cut-off is low enough that it is most likely damped by collisions.

Another low temperature system is the positive column of a DC glow discharge. The positive column has a very constant electric field that can be estimated from the product of the gas pressure (p) and discharge radius (R) [106, 121]. We find that $pR \lesssim 0.1$ cm Torr since the pressure needs to be low for the instability to be excited. Choosing $pR = 0.01$ cm Torr, a radius of $R = 10$ cm, an operating pressure of $p = 1$ mTorr, and $E/p = 100$ V/(cmTorr) from [106] for an argon plasma the electric field can be estimated as $\kappa_e \lambda_{De} = 2.4 \times 10^{-3}$ and the cut off pressure as 10 mTorr. These results are shown in the second row of Table 4.1. The fact that the cut off pressure is below the operating pressure we assumed indicates that the instability should not be totally damped and could be excited. Here the plasma density was assumed to be 1×10^{15} m^{-3}, while the electron temperature was taken to be 1 eV.

Plasmas in the upper atmosphere and space provide more opportunities for instability as most are in very low pressure environments. For example, relatively low pressure streamers can also occur in the mesosphere and are associated with thunderstorms at lower altitudes [107, 122]. Although, the electric field can be extremely non-uniform in these systems there is the possibility for a *relatively* weak electric field to form away from the head of the streamer. Here a relatively weak field may be 1 kV/m with an electron temperature of 3 eV and a plasma density of 3×10^{15} m^{-3}. At this altitude the neutral gas density is order 3×10^{20} m^{-3}, corresponding to a neutral pressure of about 10 mTorr. We can see in Table 4.1, third row, the electron-field instability would have a relatively high growth rate and a cut off pressure well above the ambient pressure.

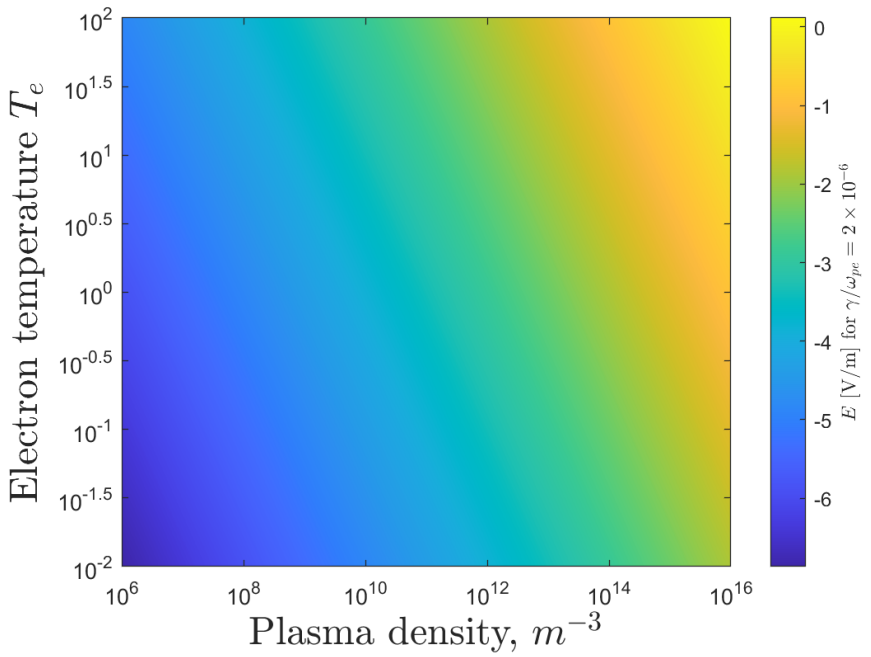

Figure 4.8: The logarithm of E_0 necessary for a plasma with density n and electron temperature T_e for $\gamma/\omega_{pe} = 2 \times 10^{-6}$.

Electric fields parallel to the Earth's magnetic field are also commonly measured in the ionosphere, are an important part of auroral processes [108], and have been shown to affect Alfven wave dispersion [123]. The strength of the field is roughly 0.01 V/m and acts on a diffuse ($n_e \approx 3 \times 10^{12}$ m^{-3}) population of electrons with a temperature that can be relatively high (10 eV). This leads to a low growth rate on order of $1 \times 10^{-5}\ \omega_{pe}^{-1}$ that corresponds to milliseconds. However, collisions that might damp the instability are rare since the ionosphere can be full ionized, especially on the day side, and so the instability may be present.

In addition to these specific examples, we note that the field required to excite the instability with a specific growth rate depends on the density and electron temperature through the Debye length. Figure 4.8 shows the field strength needed to excite the instability with a growth rate of $\gamma = 2 \times 10^{-6}\ \omega_{pe}^{-1}$. This value of the growth rate was chosen since it is relatively small when compared to the ion plasma frequency, meaning the instability may not have time to grow in the system. Thus, Fig. 4.8

effectively illustrates the minimum electric field strength need to weakly excite the instability. The minimum field is expected to increase when the electron are drifting since γ decreases for non-zero average electron velocities. As expected, the cooler and more diffuse the plasma the weaker the field needs to be (bottom left), while hotter and denser plasmas require stronger fields to be driven unstable (top right).

4.6 Conclusions

This work provides evidence in the form of 1D periodic particle-in-cell simulations that an electron plasma wave instability, called the electron-field instability, can be driven by an ambipolar electric field. The mechanism that excites the instability is different from the normal Penrose criterion, which requires the velocity distribution to have multiple peaks. Instead, the single peaked distributions can be driven unstable. The electric field fluctuations grow at the same wavelengths predicted from linear theory ($\gtrsim 30\lambda_{De}$). The linear theory predicts a growth rate for the instability that decreases with decreasing electric field strength. The predicted and measured growth rates agree well. Several well-known low-temperature and space plasmas seem susceptible to the electron-field instability. In fact, the instability may be excited in many plasma environments since electric fields are a staple feature in many systems.

CHAPTER V

Conclusions

The preceding chapters of this thesis have leveraged PIC simulations to extend the basic theoretical understanding of the presheath and sheath regions to include the effects of instabilities and collisions. To summarize: ion-acoustic instabilities enhance the energy exchange rate between electron and ions in low temperature presheaths and significantly heat the ions there above current predictions; charge-neutral collisions lower the ion velocity and relative density at the sheath edge in agreement with earlier theoretical predictions; and the ambipolar electric fields found in presheaths and other plasmas regions can drive high frequency electron plasma instabilities. Although each of these projects has furthered the current understanding of the plasma boundary, they also indicate a need for future studies.

Namely, a direct experimental test linking ion heating and the presence of ion-acoustic instabilities in the presheath is needed. So far, ion heating and ion-acoustic instabilities have both been observed experimentally, but not simultaneously. One experimental setup that would concretely link the two observations as cause and effect, would be a measurement of the ion temperature at different electron temperatures, effectively conducting an experimental analog of the simulations in chapter II. However, this requires attaining a relatively low electron temperature (≈ 0.7 eV), which may require rather specialized experiment. Showing the enhancement in ion temperature

experimentally will be especially relevant to future plasma processing techniques if they require relatively low pressure environments. Furthermore, systems often have magnetic fields applied near the boundaries. In such cases, do the instabilities develop and lead to anisotropic heating or a more complicated friction force? PIC simulations could provide a straightforward avenue for answering such questions.

Secondly, simulations confirm there is a collisional Bohm criterion that has yet to be measured experimentally. Diagnostic techniques that can span a large range of pressures are rare as many diagnostics were made with low pressures in mind. However, it may be possible to confirm the conclusions of the simulations at a relatively moderate pressure (100s mTorr). Furthermore, the simulations included in this work did not extend to atmospheric pressure, which is now a popular area for designing state-of-the-art plasma devices. Extending the PIC method to atmospheric pressure or leveraging other numerical techniques may be necessary to understand how the sheath behaves at such pressures.

Finally, when an ambipolar electric field exists in a plasma it has the ability to excite high frequency electron plasma waves via the electron-field instability. Although confirmed with first-principles PIC simulations, there is no experimental confirmation. Furthermore, the effects of such an instability were not explored here, but are needed to connect the instability to practical systems. For example, does the electron-field instability affect electron diffusion in low temperature systems like presheaths? In addition, a theoretical question remains: how does an electric field affect the other modes of the plasma. Does it modify ion-acoustic instabilities and how does a magnetic field affect the results of chapter IV? Such questions could be investigated via detailed kinetic simulation.

APPENDICES

APPENDIX A

Ion-acoustic Heating in 2D and Hybrid Simulations

A.1 Ion instability-heating in 2D

Chapter II described simulation results showing that the ions heated significantly in the presheath and only in the parallel direction corresponding to the 1D of the simulations. Is the heating still constrained along one dimension if the system has more than one spatial dimension? If not, the instability-heating may play a more important role in the context of plasma processing, where the perpendicular ion temperature is key, than the 1D simulations indicated. It seems likely that the extremely anisotropic heating observed in the 1D simulations was due to the fact that the electric field was constrained along one dimension and that some heating should occur in the perpendicular dimensions (i.e. parallel to the wall). Here, 2D simulations with a specific set of boundary conditions are employed to answer this question. Specifically, the two new boundaries introduced are opposite one another and totally reflecting (the dashed boundaries in Figure A.1). The setup is shown in Fig. A.1.

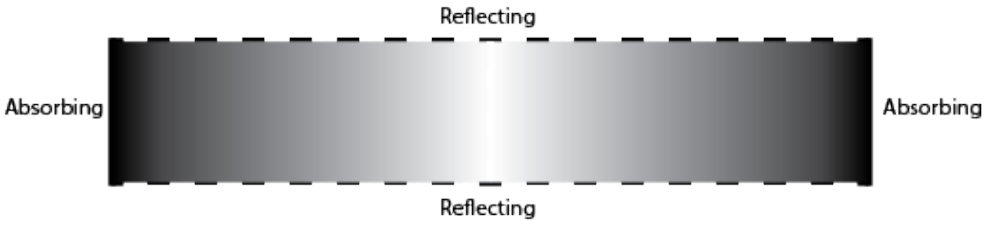

Figure A.1: The boundary conditions used in the 2D simulations for testing the effect of the second spatial dimension on the instability-heating observed in Chapter II. The horizontal dimension will be called the parallel dimension and the other the perpendicular dimension.

The use of reflecting boundaries makes comparisons with the previous 1D simulations straight forward since no spatial gradients develop along the new dimension. Specifically, the reflecting boundaries will not generate additional presheaths that could excite instabilities in addition to those on the left and right boundaries.

A.1.1 Preliminary results

A 2D simulation with the same electron and ion source temperatures, domain lengths, number of cells (along the parallel dimension), densities, and number of particles per cell as in the simulation with an electron temperature of 3 eV in chapter II has been completed. The length of the perpendicular dimension has been chosen to be several times the wavelength of the most unstable wave mode for the ion-acoustic instabilities.

Figure A.2 shows the electron density in the 2D domain after the simulation has reached steady-state. Here, the sheaths are the regions of blue near either of the absorbing boundaries.

Most importantly, Fig. A.3 shows the ion-temperature $T_i = (1/3)(T_i^x + T_i^y + T_i^z)$ as a function of the position along the x dimension. The ion temperature was calculated along a line from the center of the domain to the right absorbing boundary with a y coordinate of 0.017 m.

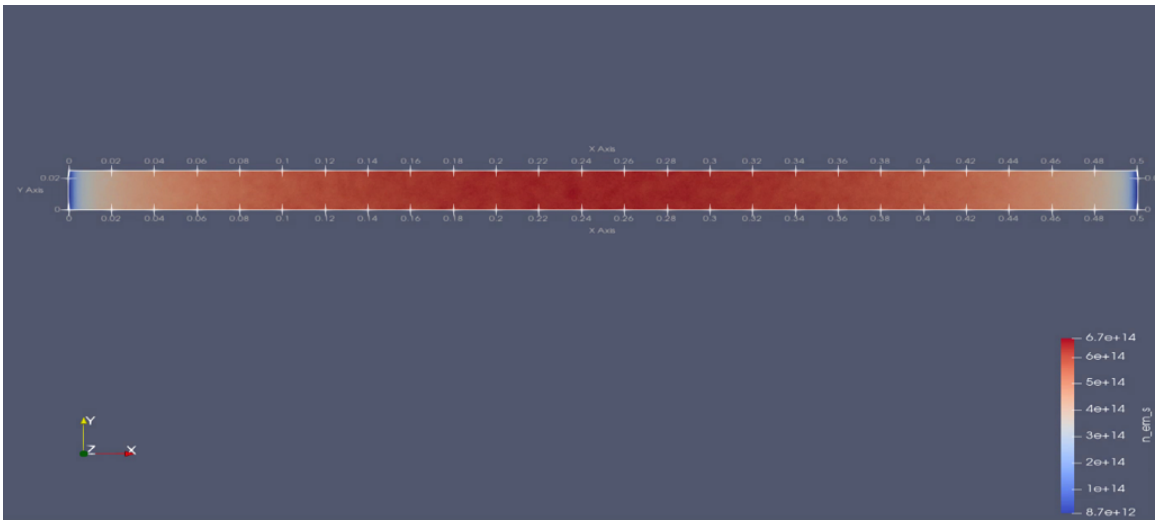

Figure A.2: Electron density plotted from a 2D simulation where the electron temperature is near 4 eV. The numbers surrounding the domain indicate the positions in meters.

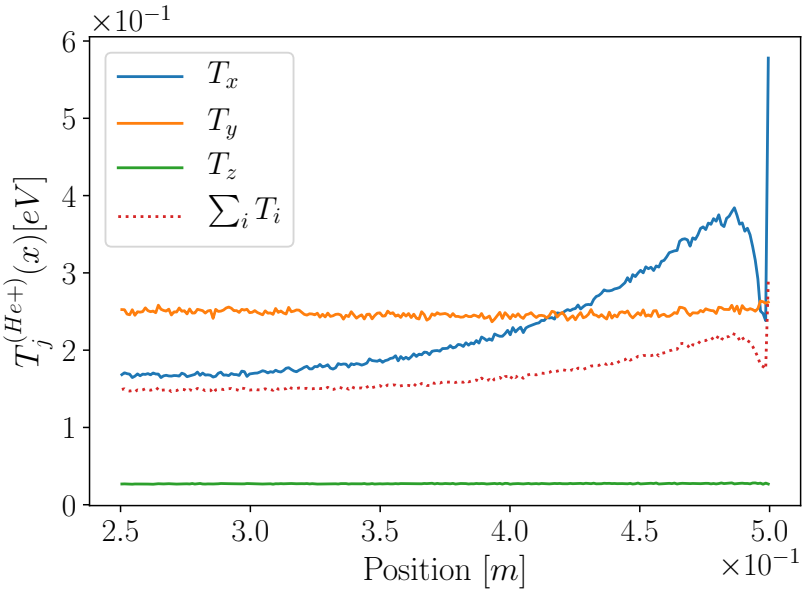

Figure A.3: Ion temperatures on a line from $x \in [0.25, 0.5], y = 0.017$ m in the 2D domain where the electron temperature is ≈ 4 eV. The blue curve is the x-direction ion temperature (the longest dimension), while the orange represents the perpendicular temperature. The green line represents the ion source temperature (300 K) and the temperature in the v_Z direction. The red dashed line is the sum of the other three and represents the 3D temperature.

This simulation clearly exhibits ion heating in the presheath in a similar manner as the 1D simulations: the ion temperature is determined by the temperature ratio threshold ($T_i \approx T_e/28 \approx 4/28 \approx 0.14$ eV) and the ions heat near the center of the domain as well. Furthermore, it shows ion heating in the perpendicular direction (y) as well. This may indicate that the instability is no longer entirely aligned along x, and may be cause by reflection from the sheaths and the new perpendicular boundaries.

A.2 Ion Heating in 1D with Boltzmann electrons

Simulations where the electrons are described by the Boltzmann relation ($n_e(x) = n_0 e^{e(\phi(x)-\phi_0)/T_e}$) are quite common and have even been used to solve the warm TL model [22]. Treating the electrons this way precludes the phenomenon of Landau damping, which depends on the electrons being particles. Landau damping is necessary for the excitation of the ion-acoustic instabilities and so they are not expected to be excited in simulations with Boltzmann electrons. However, previous simulations with Boltzmann electrons had identified instabilities non-ion-acoustic [120] as resulting from the weak electric field in the presheath. These instabilities are at a much lower frequency than the ion-acoustic instabilities. It is important to know how these low-frequency instabilities affect the plasma in the hybrid simulations. Specifically, they may alter the ion temperature from the predictions of a steady-state (not simulation based) model.

A.2.1 Preliminary results

Figure A.4 shows the ion temperature profiles throughout the presheath in a simulation with particle electrons (blue) and Boltzmann electrons (orange). The plot shows two important differences between the two simulation types: (1) no heating occurs in the center of the Boltzmann domain and (2) the heating seems to be lower in the Boltzmann domain.

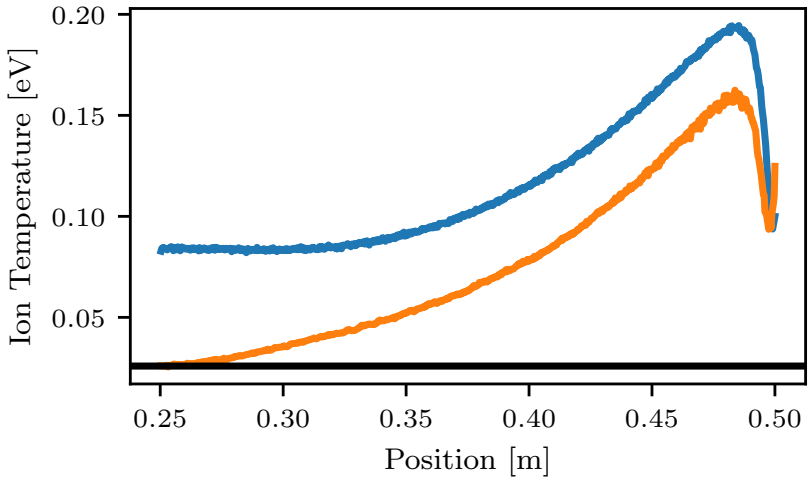

Figure A.4: Ion temperatures from a simulation with Boltzmann electrons ($T_e = 6$ eV, orange) and particle electrons ($T_e \approx 5.5$ eV, blue). The horizontal line represents the ion source temperature (300 K).

The former might be explained by the fact that any fluctuations that could lead to heating will not be able to reflect from the sheath, since the reflection of electrons from the sheath is not resolved by the Boltzmann simulations.

The heating observed in the Boltzmann simulations has two possible components: heating from ions born at different points in the presheath (a warm TL model) and heating from the low-frequency instabilities described above. At this point, there is not enough information to determine which is the leading mechanism; however, it is clear that in either case the heating in the Boltzmann simulations is lower than in the particle simulations when both have comparable electron temperatures.

Fluctuation spectra (Fig. A.5) have also been calculated from the fluctuations of the ion density in the Boltzmann simulations. Here the top panel shows the spectrum from the simulation where the electrons are treated as particles and the bottom panel that of the Boltzmann electron simulation. In each the white lines represent the ion-acoustic dispersion relation (Eq. (2.3)). One difference between the two is that the fluctuation level seems to be higher in the Boltzmann simulation, especially at frequencies lower than the ion-acoustic dispersion predicts. This may be an indication

of the low-frequency instabilities that have been previously seen in such simulations.

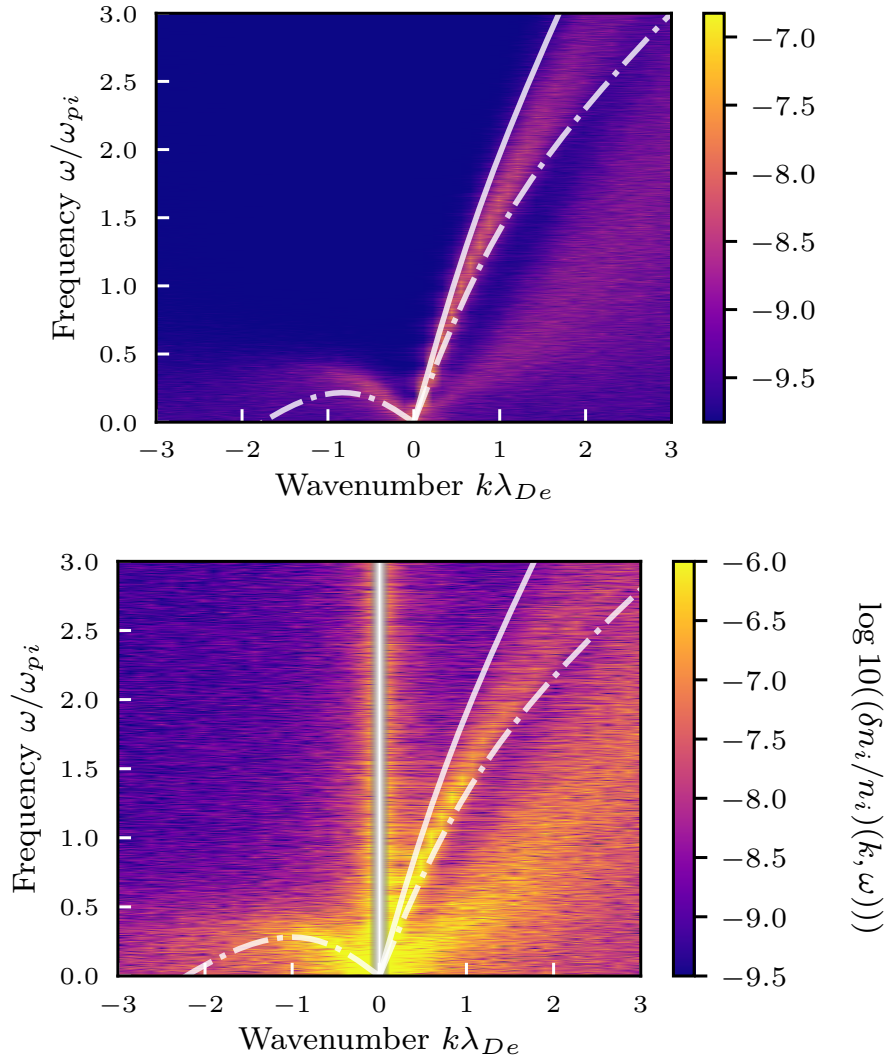

Figure A.5: Ion density fluctuation spectra calculated near the sheath edge in a simulation with particle electrons (top) and Boltzmann electrons (bottom). The white lines represent the ion-acoustic dispersion relation (Eq. (2.3)).

APPENDIX B

Collisional Plasma Equations

B.1 Numerical fluid model

Equations (3.6-3.8) can be rearranged to give a set of three coupled ODE's for the variables ϕ, E, and V_i:

$$\frac{\mathrm{d}\phi}{\mathrm{d}x} = -E \tag{B.1}$$

$$\frac{\mathrm{d}E}{\mathrm{d}x} = \frac{sx}{V_i} - e^{\phi} \tag{B.2}$$

$$\frac{\mathrm{d}V_i}{\mathrm{d}x} = \frac{E}{V_i} - \frac{V_i}{x} - \lambda_{\mathrm{De,c}}/\lambda_{in,\mathrm{c}}. \tag{B.3}$$

Here the initial condition is set at the center of the plasma ($x = 0$) with $\phi = 0, E = 0, V_i = 0$. This system of equations can solved using a standard implementation of the Runge-Kutta (4,5) method, like *ode45()* in Matlab. However, there are three difficulties in general to solving this system of ODEs: (1) a forward difference scheme (which is implemented by *ode45()*) will only calculate 0's for the given initial condition, (2) the position where the solution should end is not defined, and (3) s depends on $\lambda_{\mathrm{De,c}}/\lambda_{in,\mathrm{c}}$. The first can be avoided by starting the solution a small distance from

the middle, where the initial condition can be advanced using a backward difference scheme. To remedy the second, we defined the wall to be the point where the potential had dropped by $\Delta\phi_{\rm s}/(T_{e,{\rm c}}/e)$ as defined by Eq. (3.16). Finally, the value of s that is consistent with $\lambda_{\rm De,c}/\lambda_{in,{\rm c}}$ was found by starting with an initial guess for s and increasing or decreasing its value based on the value of $n_e - n_i$ near the first point in the domain. This was repeated until $abs(n_e - n_i)/n_{\rm c} < 10^{-4}$, which effectively enforces quasineutrality near the center. These are the same methods that have been previously used to solve a similar fluid model and are described in section 2.1.2 of [21].

The fact that the fluid model uses a constant source s has the advantage that Eq. (3.6) can be directly integrated from $x = 0$ to a point $x = \xi$. This allows us to write, in the same dimensionless variables as Eq. (3.6):

$$nV = s\xi \quad \text{or} \tag{B.4}$$

$$h_l a_l = s(L - w_{\rm s})/\lambda_{\rm De,c}, \tag{B.5}$$

where the second line was evaluated at the sheath edge. If we assume quasineutrality $[n = \exp(-\phi)]$ we can integrate Eq. (3.7) into the algebraic expressions:

$$n(V^2 + 1) + \frac{\lambda_{\rm De,c}}{\lambda_{in,{\rm c}}}\frac{s}{2}\xi^2 = 1 \quad \text{or} \tag{B.6}$$

$$h_l(a_l^2 + 1) + \frac{\lambda_{\rm De,c}}{\lambda_{in,{\rm c}}}\frac{s}{2}\left(\frac{L - w_{\rm s}}{\lambda_{\rm De,c}}\right)^2 = 1. \tag{B.7}$$

Equations (B.5-B.7) could be solved for h_l and a_l in terms of $\lambda_{\rm De,c}/\lambda_{in,{\rm c}}$ and $w_{\rm s}$, but ultimately we are looking for expressions that depend only on $\lambda_{\rm De,c}/\lambda_{in,{\rm c}}$. In practice, we found that these expressions for h_l and a_l depended sensitively on the model of $w_{\rm s}$ and so were less useful than those given in the preceding sections.

However, the low pressure limit of h_l can be easily determined from these equations

by taking $\lambda_{\mathrm{De,c}}/\lambda_{in,\mathrm{c}}$ to 0 and setting $a_l = 1$, which gives $h_l = 0.50$. Knowing h_l allows us to determine the presheath potential drop from Eq. (3.18) and we find $\frac{e\Delta\phi_p}{T_{e,c}} = 0.693$. Although this is not a new result, it does differ from what might be expected if one assumed energy is conserved for each ion. In this case the ion starts at rest in the bulk plasma and is accelerated to the sounds speed a the sheath edge leading to $e\phi_{\mathrm{se}} + 0.5 m_i c_s^2 = 0$. This indicates the potential drop is 0.5, and is lower than the fluid model predicts. This is because the steady-state fluid model conserves the energy density of the fluid, not the energy of an average ion.

B.2 Collisional Bohm criterion model

Here we develop a model of the collisional Bohm criterion using the generalized Bohm criterion from [29]. We have extended the original expression in [29] to include a constant source rate (S) to capture how plasma is sourced in our simulations. The generalized Bohm criterion includes moments of the velocity distribution function of (f_s) and takes the form

$$\sum_s q_s \frac{q_s n_s E - n_s \mathrm{d}T_s/\mathrm{d}x - \mathrm{d}\pi_s^{xx}/\mathrm{d}x - m_s V_s S + R_s}{E(m_s V_s^2 - T_s)} \geq 0. \tag{B.8}$$

Here

$$R_s = m_s \int \boldsymbol{v} C(f_s) \mathrm{d}^3 v \tag{B.9}$$

is the friction force density calculated from the collision operator C, which is due to electrons or ions colliding with neutrals. Though each of these terms contributes to the generalized Bohm criterion, several terms are usually negligible. Specifically, as it was shown in section 3.3, the electric-field and friction terms are found to be the most important for ions and only the electric-field term in the numerator is important for the electrons.

Keeping only the important terms in inequality (B.8), we have:

$$(V_i/c_{\mathrm{s,c}})^2 \leq 1 - \frac{R_{in}}{eEn}, \tag{B.10}$$

where n is the plasma density at the sheath edge. In general R_{in} depends on V_i and the electric field at the sheath edge is not yet specified, so inequality (B.10) is not an explicit form of the collisional Bohm criterion.

We can model the friction force between ion and neutrals using kinetic theory. Following the calculation used in [124] based on the Boltzmann collision operator

$$C(f_i, f_n) = \int_{\boldsymbol{v}'} \int_{\Omega} \mathrm{d}^3 v' \mathrm{d}\Omega D u (\hat{f}_i \hat{f}_n - f_i f_n). \tag{B.11}$$

Here $\hat{f}$ denotes the distribution evaluated at the post collision velocities and f at the precollision velocities. The differential cross section is labeled D, u is the relative velocity coordinate, and $\mathrm{d}\Omega = \sin\theta \mathrm{d}\theta \mathrm{d}\phi$ is the differential solid angle. Using this in Eq. (B.9) and rearranging the orders of integration gives

$$R_{in} = m_i \int \mathrm{d}^3 u \int \mathrm{d}\Omega D u \Delta \boldsymbol{u} \int \mathrm{d}^3 v' f_i(\boldsymbol{u} + \boldsymbol{v}') f_n(\boldsymbol{v}'). \tag{B.12}$$

Here $\Delta u = u[\sin(\theta)\cos(\phi)\hat{x} + \sin(\theta)\sin(\phi)\hat{y} - 2\sin^2(\theta/2)\hat{z}]$ is the relative velocity vector rotated by the scattering angle θ.

Assuming the ions are a flowing Maxwellian with average velocity $\boldsymbol{V}^i$ and the neutrals are represented by a stationary Maxwellian (with distinct temperatures), then the final integral ($\mathrm{d}^3 v'$) in Eq. (B.12) can be computed analytically. Then the $\mathrm{d}^3 u$ integral can be converted to spherical polar coordinates and the two angular integrals may be computed analytically. The friction force can then be written as

$$R_{in} = -n_i m_i \bar{\nu}_{in} \boldsymbol{V}^i \tag{B.13}$$

where

$$\bar{\nu}_{in} = \frac{n_n m_n \bar{v}_{in} a_0^2}{2\sqrt{\pi}(m_i + m_n)(\bar{V}_i)^3} I(\bar{V}_i) \tag{B.14}$$

is a velocity dependent collision frequency with $\bar{V}_i = |\boldsymbol{V}^i|/\bar{v}_{in}$, $\bar{v}_{in} = \sqrt{v_{Ti}^2 + v_{Tn}^2}$, and

$$I = \int_0^\infty \xi^2 \bar{\sigma}^{(1)}(\xi) \sum_{\pm} (2\xi \bar{V}_i \pm 1) e^{-(\xi \pm \bar{V}_i)^2} \mathrm{d}\xi \tag{B.15}$$

generalizes the Coulomb logarithm as an integral over relative velocities $\xi = u/\bar{v}_{in}$, and

$$\bar{\sigma}^{(1)}(\xi) = \frac{2\pi}{a_0^2} \int_0^\pi (1 - \cos(\theta)) D(\xi, \theta) \sin(\theta) \mathrm{d}\theta \tag{B.16}$$

is the momentum transfer cross section, measured by the Bohr radius a_0.

To proceed further, we chose to implement only the isotropic part of the differential scattering cross section, as was done in the Aleph PIC simulations. This means D only depends on the energy of the colliding particles, not the angle at which they scatter. Using this information in Eq. (B.16) we find that $\bar{\sigma}^{(1)}(\xi) = \frac{2\pi}{a_0^2} D(\xi) \int_0^\pi (1 - \cos(\theta)) \sin(\theta) \mathrm{d}\theta = \frac{4\pi}{a_0^2} D(\xi)$. Specifically, the cross section data we are using takes the form $D = (\sigma_s(c_{\mathrm{s,c}})/2\pi)(c_{\mathrm{s,c}}/\bar{v}_{in})\xi^{-1}$, where σ_s is the total cross section evaluated at an energy corresponding to $c_{\mathrm{s,c}}$. Using this cross section, the integral in Eq. (B.15) becomes

$$I = \frac{2\sqrt{\pi}(\bar{V}_i)^3 \sigma_s c_{\mathrm{s,c}}}{\bar{v}_{in} a_0^2}, \tag{B.17}$$

and entering this into Eq. (B.14) gives

$$\bar{\nu}_{in} = n_n \sigma_s c_{\mathrm{s,c}}. \tag{B.18}$$

Finally, we arrive at an expression for the ion friction force due to collisions with the neutrals:

$$R_{in} = -m_i n_i \boldsymbol{V}^i \frac{c_{\mathrm{s,c}}}{\lambda_{in,\mathrm{c}}(c_{\mathrm{s,c}})} \tag{B.19}$$

where $\lambda_{in,\mathrm{c}}(c_{\mathrm{s,c}}) = 1/(n_n\sigma(c_{\mathrm{s,c}}))$ and $\sigma(c_{\mathrm{s,c}})$ is the total elastic cross section evaluated at the sound speed. Eq. (B.19) can then be used in Eq. (B.10), which can be solved for V_i once a model for E is provided. Based on figure 3.6, E_{se} can be approximated as a constant. Finally solving Eq. (B.10) gives the same model for the collisional Bohm criterion that is provided in Eq. (3.12).

B.3 Edge-to-center density model

Here we derive a model for h_l in a planar, symmetric plasma with a uniform source profile. We use the model Eq. (3.6-3.8), but with the added condition that the plasma is quasinuetral ($n_i \approx n_e$). Making use of the Boltzmann density relation for the electrons we find that $E = -(T_{e,\mathrm{c}}/en)\frac{\mathrm{d}n}{\mathrm{d}x}$ and the model equations become:

$$\frac{\mathrm{d}(nV)}{\mathrm{d}x} = s \tag{B.20}$$

$$nV\frac{\mathrm{d}V}{\mathrm{d}x} = -\frac{\mathrm{d}n}{\mathrm{d}x} - (\lambda_{\mathrm{De,c}}/\lambda_{in,\mathrm{c}})nV - sV. \tag{B.21}$$

These can be solved for $\frac{\mathrm{d}n}{\mathrm{d}x}$ and $\frac{\mathrm{d}V}{\mathrm{d}x}$ giving:

$$\frac{\mathrm{d}n}{\mathrm{d}x} = \frac{-V}{1-V^2}[2s + (\lambda_{\mathrm{De,c}}/\lambda_{in,\mathrm{c}})n] \tag{B.22}$$

$$\frac{\mathrm{d}V}{\mathrm{d}x} = -\frac{1}{n(1-V^2)}\{s + [s + (\lambda_{\mathrm{De,c}}/\lambda_{in,\mathrm{c}})n]V^2\}. \tag{B.23}$$

Dividing Eq. (B.22) by Eq. (B.23) we have a tractable ODE to solve with the boundary condition $n(V=0) = 1$:

$$\frac{\mathrm{d}n}{\mathrm{d}V} = -nV\left[\frac{2s + (\lambda_{\mathrm{De,c}}/\lambda_{in,\mathrm{c}})n}{s + (s + (\lambda_{\mathrm{De,c}}/\lambda_{in,\mathrm{c}})n)V^2}\right] \tag{B.24}$$

Equation (B.24) has the solution

$$n(V) = \frac{-s(1+V^2) + \sqrt{s^2(1+V^4) + 2s(s + \frac{\lambda_{\mathrm{De,c}}}{\lambda_{in,\mathrm{c}}})V^2}}{(\lambda_{\mathrm{De,c}}/\lambda_{in,\mathrm{c}})V^2}. \tag{B.25}$$

To derive a formula for h_l we take the small and large $\lambda_{\mathrm{De,c}}/\lambda_{in,\mathrm{c}}$ limits of Eq. (B.25) and evaluate them at the sheath edge (i.e. where $V = a_l$). We solve these equations for h_l in each limit and determine their scaling with $\lambda_{\mathrm{De,c}}/\lambda_{in,\mathrm{c}}$. Finally, we construct an expression that captures both limits. However, it is important to notice that both s and V scale with $\lambda_{\mathrm{De,c}}/\lambda_{in,\mathrm{c}}$. The scaling of V is given in Eq. (3.12). We observe, from our PIC simulation data, that $s \approx 0.0071(1 + 50(\lambda_{\mathrm{De,c}}/\lambda_{in,\mathrm{c}}))^{-1}$.

The small $\lambda_{\mathrm{De,c}}/\lambda_{in,\mathrm{c}}$ expansion of Eq. (B.25) is

$$n \approx 0.50 - 6.12(\lambda_{\mathrm{De,c}}/\lambda_{in,\mathrm{c}}) - 177(\lambda_{\mathrm{De,c}}/\lambda_{in,\mathrm{c}})^2. \tag{B.26}$$

The large $\lambda_{\mathrm{De,c}}/\lambda_{in,\mathrm{c}}$ expansion of Eq. (B.25) is

$$n \approx 0.165 - \frac{1.50 \times 10^{-3}}{(\lambda_{\mathrm{De,c}}/\lambda_{in,\mathrm{c}})} + \frac{1.20 \times 10^{-3}}{(\lambda_{\mathrm{De,c}}/\lambda_{in,\mathrm{c}})}. \tag{B.27}$$

The leading order in both of these expression are captured in the Pade approximate expression

$$n \approx \frac{0.500 + 3.01(\lambda_{\mathrm{De,c}}/\lambda_{in,\mathrm{c}})}{1 + 18.3(\lambda_{\mathrm{De,c}}/\lambda_{in,\mathrm{c}})}, \tag{B.28}$$

where the leading order term in Eq. (B.26) and (B.27) were used to match to the expansions of $(A + Bx)/(1 + Cx)$.

BIBLIOGRAPHY

BIBLIOGRAPHY

[1] I. Langmuir, "Positive Ion Currents from the Positive Column of Mercury Arcs," *Science*, vol. 58, pp. 290–291, Oct. 1923.

[2] I. Langmuir, "Scattering of Electrons in Ionized Gases," *Physical Review*, vol. 26, no. 5, pp. 585–613, 1925. Publisher: Physical Review.

[3] I. Langmuir, "The Interaction of Electron and Positive Ion Space Charges in Cathode Sheaths," *Physical Review*, vol. 33, pp. 954–989, June 1929.

[4] J. W. Coburn and H. F. Winters, "Plasma etching—A discussion of mechanisms," p. 14.

[5] L. Tonks and I. Langmuir, "A General Theory of the Plasma of an Arc," *Physical Review*, vol. 34, pp. 876–922, Sept. 1929.

[6] E. R. Harrison and W. B. Thompson, "The Low Pressure Plane Symmetric Discharge," *Proceedings of the Physical Society*, vol. 74, pp. 145–152, Aug. 1959.

[7] K.-U. Riemann, "Plasma-sheath transition in the kinetic Tonks-Langmuir model," *Physics of Plasmas*, vol. 13, no. 6, p. 063508, 2006. Publisher: Physics of Plasmas.

[8] D. R. Nicholson and D. R. Nicholson, *Introduction to plasma theory*, vol. 1. Wiley New York, 1983.

[9] J. Jackson, "Longitudinal plasma oscillations," *Journal of Nuclear Energy. Part C, Plasma Physics, Accelerators, Thermonuclear Research*, vol. 1, no. 4, p. 171, 1960. Publisher: IOP Publishing.

[10] D. A. Gurnett and A. Bhattacharjee, *Introduction to Plasma Physics: With Space, Laboratory and Astrophysical Applications*. Cambridge: Cambridge University Press, 2 ed., 2017.

[11] S. D. Baalrud, J. D. Callen, and C. C. Hegna, "A kinetic equation for unstable plasmas in a finite space-time domain," *Physics of Plasmas*, vol. 15, p. 092111, Sept. 2008.

[12] P. J. Adrian, S. D. Baalrud, and T. Lafleur, "Influence of neutral pressure on instability enhanced friction and ion velocities at the sheath edge of two-ion-species plasmas," *Physics of Plasmas*, vol. 24, p. 123505, Dec. 2017.

[13] G. Severn, C.-S. Yip, N. Hershkowitz, and S. D. Baalrud, "Experimental studies of ion flow near the sheath edge in multiple ion species plasma including argon, xenon and neon," *Plasma Sources Science and Technology*, vol. 26, no. 5, p. 055021, 2017. Publisher: Plasma Sources Science and Technology.

[14] N.-K. Kim, J. Song, H.-J. Roh, Y. Jang, S. Ryu, S.-R. Huh, and G.-H. Kim, "Ion-neutral collision effect on ion-ion two-stream-instability near sheath-presheath boundary in two-ion-species plasmas," *Plasma Sources Science and Technology*, vol. 26, no. 6, p. 06LT01, 2017. Publisher: IOP Publishing.

[15] V. Godyak, "Modified Bohm criterion for a collisional plasma," *Physics Letters A*, vol. 89, pp. 80–81, Apr. 1982.

[16] H. Valentini, "Bohm criterion for the collisional sheath," *Physics of Plasmas*, vol. 3, pp. 1459–1461, Apr. 1996.

[17] R. P. Brinkmann, "The plasma–sheath transition in low temperature plasmas: on the existence of a collisionally modified Bohm criterion," *Journal of Physics D: Applied Physics*, vol. 44, p. 042002, Feb. 2011.

[18] X. P. Chen, "Sheath criterion and boundary conditions for an electrostatic sheath," *Physics of Plasmas*, vol. 5, pp. 804–807, Mar. 1998.

[19] K.-U. Riemann, "The Bohm criterion and sheath formation," p. 27.

[20] D. Bohm, *The characteristics of electrical discharges in magnetic fields*. McGraw-Hill, 1949. Publication Title: Qualitative Description of the Arc Plasma in a Magnetic Field.

[21] S. Robertson, "Sheaths in laboratory and space plasmas," *Plasma Physics and Controlled Fusion*, vol. 55, p. 093001, Sept. 2013.

[22] T. E. Sheridan, "Solution of the plasma-sheath equation with a cool Maxwellian ion source," *Physics of Plasmas*, vol. 8, pp. 4240–4245, Sept. 2001.

[23] D. Coulette and G. Manfredi, "Collisionless "thermalization" in the sheath of an argon discharge," *Physics of Plasmas*, vol. 22, p. 043505, Apr. 2015.

[24] C.-S. Yip, N. Hershkowitz, and G. Severn, "Verifying effects of instability enhanced ion–ion Coulomb collisions on ion velocity distribution functions near the sheath edge in low temperature plasmas," *Plasma Sources Science and Technology*, vol. 24, p. 015018, Dec. 2014.

[25] R. Hood, S. D. Baalrud, R. L. Merlino, and F. Skiff, "Laser-induced fluorescence measurements of ion fluctuations in electron and ion presheaths," *Physics of Plasmas*, vol. 27, p. 053509, May 2020.

[26] N. Hershkowitz, C.-S. Yip, and G. D. Severn, "Experimental test of instability enhanced collisional friction for determining ion loss in two ion species plasmas," *Physics of Plasmas*, vol. 18, p. 057102, May 2011.

[27] S.-B. Wang and A. Wendt, "Sheath thickness evaluation for collisionless or weakly collisional bounded plasmas," *IEEE Transactions on Plasma Science*, vol. 27, pp. 1358–1365, Oct. 1999.

[28] J. H. Palacio Mizrahi, V. T. Gurovich, and Y. E. Krasik, "Unified one-dimensional model of bounded plasma with nonzero ion temperature in a broad pressure range," *Physics of Plasmas*, vol. 20, p. 032116, Mar. 2013.

[29] S. D. Baalrud and C. C. Hegna, "Kinetic theory of the presheath and the Bohm criterion," *Plasma Sources Science and Technology*, vol. 20, p. 025013, Apr. 2011.

[30] S. D. Baalrud, "Influence of ion streaming instabilities on transport near plasma boundaries," *Plasma Sources Science and Technology*, vol. 25, p. 025008, Apr. 2016.

[31] Y. Li, B. Srinivasan, Y. Zhang, and X.-Z. Tang, "Bohm criterion of plasma sheaths away from asymptotic limits," *Physical Review Letters*, vol. 128, no. 8, 2022.

[32] Y. Li, B. Srinivasan, Y. Zhang, and X.-Z. Tang, "Transport physics dependence of bohm speed in presheath–sheath transition," *Physics of Plasmas*, vol. 29, no. 11, p. 113509, 2022.

[33] P. Cagas, A. Hakim, J. Juno, and B. Srinivasan, "Continuum kinetic and multi-fluid simulations of classical sheaths," *Physics of Plasmas*, vol. 24, no. 2, p. 022118, 2017.

[34] C. K. Birdsall and A. B. Langdon, *Plasma physics via computer simulation*. CRC press, 2018.

[35] L. Schiesko, A. Revel, T. Minea, and E. Carbone, "On the use of ultra-high resolution pic methods to unveil microscale effects of plasma kinetic instabilities: electron trapping and release by electrostatic tidal effect," *Plasma Sources Science and Technology*, vol. 31, no. 4, p. 04LT01, 2022.

[36] R. Courant, K. Friedrichs, and H. Lewy, "On the Partial Difference Equations of Mathematical Physics," *IBM Journal of Research and Development*, vol. 11, no. 2, pp. 215–234, 1967. Publisher: IBM.

[37] E. Cormier-Michel, B. A. Shadwick, C. G. R. Geddes, E. Esarey, C. B. Schroeder, and W. P. Leemans, "Unphysical kinetic effects in particle-in-cell modeling of laser wakefield accelerators," *Physical Review E*, vol. 78, no. 1, 2008. Publisher: Physical Review E.

[38] R. W. Hockney and J. W. Eastwood, *Computer simulation using particles*. crc Press, 2021.

[39] V. Vahedi and M. Surendra, "A monte carlo collision model for the particle-in-cell method: applications to argon and oxygen discharges," *Computer Physics Communications*, vol. 87, no. 1-2, p. 179–198, 1995.

[40] G. Bird, *Molecular gas dynamics and the direct simulation of gas flows*. Oxford University Press, 1994.

[41] G. A. Bird, "Direct Simulation and the Boltzmann Equation," *Physics of Fluids*, vol. 13, no. 11, p. 2676, 1970. Publisher: Physics of Fluids.

[42] B. Scheiner and P. J. Adrian, "Why the particle-in-cell method captures instability enhanced collisions," *Physics of Plasmas*, vol. 26, p. 034501, Mar. 2019.

[43] H. Timko, P. S. Crozier, M. M. Hopkins, K. Matyash, and R. Schneider, "Why Perform Code-to-Code Comparisons: A Vacuum Arc Discharge Simulation Case Study," *Contributions to Plasma Physics*, vol. 52, pp. 295–308, May 2012.

[44] L. P. Beving, M. M. Hopkins, and S. D. Baalrud, "Simulations of ion heating due to ion-acoustic instabilities in presheaths," *Physics of Plasmas*, vol. 28, p. 123516, Dec. 2021.

[45] L. P. Beving, M. M. Hopkins, and S. D. Baalrud, "How sheath properties change with gas pressure: modeling and simulation," *Plasma Sources Science and Technology*, vol. 31, no. 8, p. 084009, 2022.

[46] M. A. Lieberman and A. J. Lichtenberg, *Principles of plasma discharges and materials processing*. Hoboken, N.J: Wiley-Interscience, 2nd ed ed., 2005. OCLC: ocm56752658.

[47] J. Pelletier and A. Anders, "Plasma-based ion implantation and deposition: a review of physics, technology, and applications," *IEEE Transactions on Plasma Science*, vol. 33, pp. 1944–1959, Dec. 2005.

[48] M. Sasao, K. Connor, K. Ida, H. Iguchi, A. Ivanov, M. Nishiura, D. Thomas, M. Wada, and M. Yoshinuma, "Ion sources for fusion plasma diagnostics," *IEEE Transactions on Plasma Science*, vol. 33, pp. 1872–1900, Dec. 2005.

[49] K. Takahashi, "Helicon-type radiofrequency plasma thrusters and magnetic plasma nozzles," *Reviews of Modern Plasma Physics*, vol. 3, p. 3, Dec. 2019.

[50] A. Sánchez-Villar, J. Zhou, E. Ahedo, and M. Merino, "Coupled plasma transport and electromagnetic wave simulation of an ECR thruster," *Plasma Sources Science and Technology*, vol. 30, p. 045005, Apr. 2021.

[51] J. Glanz and N. Hershkowitz, "Ion-acoustic noise excited by positive probes," *Plasma Physics*, vol. 23, pp. 325–335, Apr. 1981.

[52] B. T. Yee, B. Scheiner, S. D. Baalrud, E. V. Barnat, and M. M. Hopkins, "Electron presheaths: the outsized influence of positive boundaries on plasmas," *Plasma Sources Science and Technology*, vol. 26, p. 025009, Jan. 2017.

[53] B. Scheiner, S. D. Baalrud, B. T. Yee, M. M. Hopkins, and E. V. Barnat, "Theory of the electron sheath and presheath," *Physics of Plasmas*, vol. 22, p. 123520, Dec. 2015.

[54] B. A. Jorns, I. G. Mikellides, and D. M. Goebel, "Ion acoustic turbulence in a 100-A LaB 6 hollow cathode," *Physical Review E*, vol. 90, p. 063106, Dec. 2014.

[55] T. Lafleur, S. D. Baalrud, and P. Chabert, "Characteristics and transport effects of the electron drift instability in Hall-effect thrusters," *Plasma Sources Science and Technology*, vol. 26, p. 024008, Jan. 2017.

[56] K. Hara, "An overview of discharge plasma modeling for Hall effect thrusters," *Plasma Sources Science and Technology*, vol. 28, p. 044001, Apr. 2019.

[57] I. D. Kaganovich, A. Smolyakov, Y. Raitses, E. Ahedo, I. G. Mikellides, B. Jorns, F. Taccogna, R. Gueroult, S. Tsikata, A. Bourdon, J.-P. Boeuf, M. Keidar, A. T. Powis, M. Merino, M. Cappelli, K. Hara, J. A. Carlsson, N. J. Fisch, P. Chabert, I. Schweigert, T. Lafleur, K. Matyash, A. V. Khrabrov, R. W. Boswell, and A. Fruchtman, "Physics of E × B discharges relevant to plasma propulsion and similar technologies," *Physics of Plasmas*, vol. 27, p. 120601, Dec. 2020.

[58] N. Claire, G. Bachet, U. Stroth, and F. Doveil, "Laser-induced-fluorescence observation of ion velocity distribution functions in a plasma sheath," *Phys. Plasmas*, p. 9.

[59] A. Meige, O. Sutherland, H. B. Smith, and R. W. Boswell, "Ion heating in the presheath," *Physics of Plasmas*, vol. 14, p. 032104, Mar. 2007.

[60] D. Lee, N. Hershkowitz, and G. D. Severn, "Measurements of Ar+ and Xe+ velocities near the sheath boundary of Ar–Xe plasma using two diode lasers," *Applied Physics Letters*, vol. 91, p. 041505, July 2007.

[61] S. D. Baalrud, J. D. Callen, and C. C. Hegna, "Instability-Enhanced Collisional Effects and Langmuir's Paradox," *Physical Review Letters*, vol. 102, p. 245005, June 2009.

[62] "Phelps database, www.lxcat.net, accessed 6th June 2020."

[63] "Phelps database, private communication, www.lxcat.net, accessed 6th June 2020."

[64] R. Crompton, M. Elford, and R. Jory, "The Momentum Transfer Cross Section for Electrons in Helium," *Australian Journal of Physics*, vol. 20, no. 4, p. 369, 1967.

[65] M. Hayashi, "Recommended values of transport cross sections for elestic collisions and total collision cross section for electrons in atomic and molecular gases," Tech. Rep. IPPJ-AM-19, Institute of Plasma Physics, Nagoya Institute of Technology, Nov. 1981.

[66] J. D. J. D. Huba, 1950, *NRL Plasma Formulary*. Revised 1998. Washington, DC : Naval Research Laboratory, [1998], 1998.

[67] M. E. Dieckmann, A. Ynnerman, S. C. Chapman, G. Rowlands, and N. Andersson, "Simulating Thermal Noise," *Physica Scripta*, vol. 69, pp. 456–460, Jan. 2004.

[68] A. B. Langdon, "Kinetic theory for fluctuations and noise in computer simulation of plasma," *Physics of Fluids*, vol. 22, no. 1, p. 163, 1979.

[69] N. Rostoker, "Fluctuations of a plasma (I)," *Nuclear Fusion*, vol. 1, pp. 101–120, Mar. 1961.

[70] T. Lafleur, S. D. Baalrud, and P. Chabert, "Theory for the anomalous electron transport in Hall effect thrusters. II. Kinetic model," *Physics of Plasmas*, vol. 23, p. 053503, May 2016.

[71] O. Ishihara, I. Alexeff, H. J. Doucet, and W. D. Jones, "Reflection and absorption of ion-acoustic waves in a density gradient," *Physics of Fluids*, vol. 21, no. 12, p. 2211, 1978.

[72] B. Bertotti, "Reflection-Absorption Properties of Walls and Sheaths in the Propagation of Ion-Acoustic Waves," *Physics of Fluids*, vol. 9, no. 7, p. 1428, 1966.

[73] I. Ibrahim and H. H. Kuehl, "Reflection of ion acoustic waves by the plasma sheath," *Physics of Fluids*, vol. 27, no. 4, p. 962, 1984.

[74] J. Berumen and F. Skiff, "Analysis and comparison of ion-acoustic wave reflection using laser-induced fluorescence and Langmuir probes," *Physics of Plasmas*, vol. 25, p. 122102, Dec. 2018.

[75] P. L. Bhatnagar, E. P. Gross, and M. Krook, "A Model for Collision Processes in Gases. I. Small Amplitude Processes in Charged and Neutral One-Component Systems," *Physical Review*, vol. 94, pp. 511–525, May 1954.

[76] P. Chabert and N. Braithwaite, "Physics of Radio-Frequency Plasmas," p. 395.

[77] J.-L. Raimbault and P. Chabert, "Edge-to-center plasma density ratio in high density plasma sources," *Plasma Sources Science and Technology*, vol. 18, p. 014017, Feb. 2009.

[78] J.-Y. Liu, Z.-X. Wang, and X. Wang, "Sheath criterion for a collisional sheath," *Physics of Plasmas*, vol. 10, pp. 3032–3034, July 2003.

[79] M. S. Benilov, "The Child–Langmuir law and analytical theory of collisionless to collision-dominated sheaths," *Plasma Sources Science and Technology*, vol. 18, p. 014005, Feb. 2009.

[80] A. Kono, "Structure of collisional and collisionless sheaths: closed expressions for sheath thickness," *Journal of Physics D: Applied Physics*, vol. 37, pp. 1945–1953, July 2004.

[81] R. N. Franklin and J. Snell, "The plasma-sheath transition with a constant mean free path model and the applicability of the Bohm criterion," *Physics of Plasmas*, vol. 8, no. 2, pp. 643–647, 2001. _eprint: https://doi.org/10.1063/1.1334609.

[82] T. E. Sheridan and J. Goree, "Collisional plasma sheath model," *Physics of Fluids B: Plasma Physics*, vol. 3, pp. 2796–2804, Oct. 1991.

[83] T. Lafleur and P. Chabert, "Edge-to-center density ratios in low-temperature plasmas," *Plasma Sources Science and Technology*, vol. 24, 2015.

[84] R. J. Procassini, C. K. Birdsall, and E. C. Morse, "A fully kinetic, self-consistent particle simulation model of the collisionless plasma–sheath region," *Physics of Fluids B: Plasma Physics*, vol. 2, pp. 3191–3205, Dec. 1990.

[85] L. Oksuz and N. Hershkowitz, "Plasma, presheath, collisional sheath and collisionless sheath potential profiles in weakly ionized, weakly collisional plasma," *Plasma Sources Science and Technology*, vol. 14, pp. 201–208, Feb. 2005.

[86] K. Kutasi and Z. Donkó, "Hybrid model of a plane-parallel hollow-cathode discharge," *Journal of Physics D: Applied Physics*, vol. 33, pp. 1081–1089, May 2000.

[87] A. Tavant, R. Lucken, A. Bourdon, and P. Chabert, "Non-isothermal sheath model for low pressure plasmas," *Plasma Sources Science and Technology*, vol. 28, p. 075007, July 2019.

[88] Y. Zhang, C. Charles, and R. Boswell, "A POLYTROPIC MODEL FOR SPACE AND LABORATORY PLASMAS DESCRIBED BY BI-MAXWELLIAN ELECTRON DISTRIBUTIONS," *The Astrophysical Journal*, vol. 829, p. 10, Sept. 2016. Publisher: American Astronomical Society.

[89] R. Sahu, A. Tropina, and R. Miles, "Isentropic plasma sheath model for improved fidelity," *Physics of Plasmas*, vol. 29, no. 4, p. 040701, 2022. _eprint: https://doi.org/10.1063/5.0084712.

[90] F. F. Chen, *Introduction to Plasma Physics*. Boston, MA: Springer US, 1995.

[91] H. Ghomi and M. Khoramabadi, "Influence of ion temperature on plasma sheath transition," *Journal of Plasma Physics*, vol. 76, pp. 247–255, Apr. 2010.

[92] Z. Sternovsky and S. Robertson, "Numerical solutions to the weakly collisional plasma and sheath in the fluid approach and the reduction of the ion current to the wall," *IEEE Transactions on Plasma Science*, vol. 34, pp. 850–854, June 2006.

[93] S. D. Baalrud, T. Lafleur, R. W. Boswell, and C. Charles, "Particle-in-cell simulations of a current-free double layer," *Physics of Plasmas*, vol. 18, p. 063502, June 2011.

[94] G.-H. Kim, H.-C. Lee, and C.-W. Chung, "Experimental investigation of edge-to-center density ratio in inductively coupled plasmas," *Physics of Plasmas*, vol. 17, p. 073504, July 2010.

[95] I. D. Kaganovich, "How to patch active plasma and collisionless sheath: A practical guide," *Physics of Plasmas*, vol. 9, pp. 4788–4793, Nov. 2002.

[96] K.-U. Riemann, "The influence of collisions on the plasma sheath transition," *Physics of Plasmas*, vol. 4, pp. 4158–4166, Nov. 1997.

[97] Z. Sternovsky, K. Downum, and S. Robertson, "Numerical solutions to a kinetic model for the plasma-sheath problem with charge exchange collisions of ions," *Physical Review E*, vol. 70, p. 026408, Aug. 2004.

[98] M. J. Kushner, "Floating Sheath Potentials in Non-Maxwellian Plasmas," *IEEE Transactions on Plasma Science*, vol. 13, pp. 6–9, Feb. 1985.

[99] S. Langendorf, M. Walker, L. Rose, M. Keidar, and L. Brieda, "Study of the Plasma-Wall Interface–Measurement and Simulation of Sheath Potential Profiles," (Washington DC), Oct. 2013.

[100] T. Sheridan and J. Goree, "Analytic expression for the electric potential in the plasma sheath," *IEEE Transactions on Plasma Science*, vol. 17, pp. 884–888, Dec. 1989.

[101] P. Chabert, "What is the size of a floating sheath?," *Plasma Sources Science and Technology*, vol. 23, p. 065042, Oct. 2014.

[102] R. Warren, "Interpretation of Field Measurements in the Cathode Region of Glow Discharges," *Physical Review*, vol. 98, pp. 1658–1664, June 1955.

[103] N. F. Mott and R. W. Gurney, *Electronic processes in ionic crystals*. Clarendon Press, 1948.

[104] S. Naggary, D. Engel, L. Kroll, and R. P. Brinkmann, "Bridging Child–Langmuir and Warren: exact and approximate solutions for the unipolar sheath of intermediate pressure," *Plasma Sources Science and Technology*, vol. 28, p. 015003, Jan. 2019.

[105] Young Wook Choi and Hae-June Lee, "Analysis of collisional sheath structure in an argon DC discharge," *IEEE Transactions on Plasma Science*, vol. 31, pp. 1032–1037, Oct. 2003.

[106] V. Lisovskiy, K. Artushenko, and V. Yegorenkov, "Reduced electric field in the positive column of the glow discharge in argon," *Vacuum*, vol. 122, pp. 75–81, Dec. 2015.

[107] S. Nijdam, J. Teunissen, and U. Ebert, "The physics of streamer discharge phenomena," *Plasma Sources Science and Technology*, vol. 29, p. 103001, Nov. 2020.

[108] G. T. Marklund, "Electric Fields and Plasma Processes in the Auroral Downward Current Region, Below, Within, and Above the Acceleration Region," *Space Science Reviews*, vol. 142, pp. 1–21, Feb. 2009.

[109] V. Rozhansky, E. Kaveeva, I. Senichenkov, E. Sytova, I. Veselova, S. Voskoboynikov, and D. Coster, "Electric fields and currents in the detached regime of a tokamak," *Contributions to Plasma Physics*, vol. 58, pp. 540–546, July 2018.

[110] P. Foukal and S. Hinata, "Electric fields in the solar atmosphere: A review," *Solar Physics*, vol. 132, pp. 307–334, Apr. 1991.

[111] S. M. Hamberger, "Experimental Studies of Electrostatic Fluctuations in a Turbulently Heated Plasma," *Physics of Fluids*, vol. 15, no. 5, p. 825, 1972.

[112] B. Coppi, "Anomalous Plasma Resistivity at Low Electric Fields," *Physics of Fluids*, vol. 14, no. 1, p. 134, 1971.

[113] G. F. Reiter, "Instability of the Steady State of a Plasma in a Uniform Electric Field," *Physics of Fluids*, vol. 10, no. 4, p. 703, 1967.

[114] O. Penrose, "Electrostatic Instabilities of a Uniform Non-Maxwellian Plasma," *Physics of Fluids*, vol. 3, no. 2, p. 258, 1960.

[115] B. D. Fried, M. Gell-Mann, J. D. Jackson, and H. W. Wyld, "Longitudinal plasma oscillations in an electric field," *Journal of Nuclear Energy. Part C, Plasma Physics, Accelerators, Thermonuclear Research*, vol. 1, pp. 190–198, Jan. 1960.

[116] B. D. Fried and G. J. Culler, "Plasma Oscillations in an External Electric Field," p. 12, 1963.

[117] R. Kompaneets, Y. O. Tyshetskiy, and S. V. Vladimirov, "Ion response in a weakly ionized plasma with ion flow," *Physics of Plasmas*, vol. 20, p. 042108, Apr. 2013.

[118] R. Kompaneets, A. V. Ivlev, S. V. Vladimirov, and G. E. Morfill, "Instability of ion kinetic waves in a weakly ionized plasma," *Physical Review E*, vol. 85, p. 026412, Feb. 2012.

[119] A. N. Kryshtal, "Bernstein-wave instability in a collisional plasma with a quasistatic electric field," *Journal of Plasma Physics*, vol. 60, pp. 469–484, Oct. 1998.

[120] T. E. Sheridan and S. D. Baalrud, "Time-dependent Tonks-Langmuir model is unstable," *Physical Review E*, vol. 96, p. 053201, Nov. 2017.

[121] C. Yuan, A. A. Kudryavtsev, and V. I. Demidov, *Introduction to the Kinetics of Glow Discharges*. 2053-2571, Morgan & Claypool Publishers, 2018.

[122] U. Ebert, S. Nijdam, C. Li, A. Luque, T. Briels, and E. van Veldhuizen, "Review of recent results on streamer discharges and discussion of their relevance for sprites and lightning," *Journal of Geophysical Research: Space Physics*, vol. 115, July 2010.

[123] P. Varma, S. Mishra, G. Ahirwar, and M. Tiwari, "Effect of parallel electric field on Alfven wave in thermal magnetoplasma," *Planetary and Space Science*, vol. 55, pp. 174–180, Jan. 2007.

[124] S. D. Baalrud, "Transport coefficients in strongly coupled plasmas," *Physics of Plasmas*, vol. 19, p. 030701, Mar. 2012.